

**GEOMETRIC ANALYSIS OF HIGH RESOLUTION SPACE IMAGES  
USING PARAMETRIC APPROACHES CONSIDERING SATELLITE  
ORBITAL PARAMETERS**

**Ph.D. Thesis by  
Hüseyin TOPAN**

**Department : Geodesy and Photogrammetric Engineering**

**Programme : Geomatics Engineering**

**DECEMBER 2009**



**GEOMETRIC ANALYSIS OF HIGH RESOLUTION SPACE IMAGES  
USING PARAMETRIC APPROACHES CONSIDERING SATELLITE  
ORBITAL PARAMETERS**

**Ph.D. Thesis by  
Hüseyin TOPAN  
(501042607)**

**Date of submission : 27 October 2009  
Date of defence examination: 03 December 2009**

**Supervisor (Chairman) : Prof. Dr. Derya MAKTAV (ITU)  
Members of the Examining Committee : Prof. Dr. Filiz SUNAR (ITU)  
Assis. Prof. Dr. Orhan KURT (KOU)  
Prof.Dr. Sıtkı KÜLÜR (ITU)  
Prof.Dr. Şenol KUŞÇU (ZKU)**

**DECEMBER 2009**



**İSTANBUL TEKNİK ÜNİVERSİTESİ ★ FEN BİLİMLERİ ENSTİTÜSÜ**

**YÜKSEK ÇÖZÜNÜRLÜKLÜ UYDU GÖRÜNTÜLERİNİN UYDU  
YÖRÜNGE PARAMETRELERİNİ DİKKATE ALAN PARAMETRİK  
MODELLERLE GEOMETRİK ANALİZİ**

**DOKTORA TEZİ  
Hüseyin TOPAN  
(501042607)**

**Tezin Enstitüye Verildiği Tarih : 27 Ekim 2009**

**Tezin Savunulduğu Tarih : 03 Aralık 2009**

**Tez Danışmanı : Prof. Dr. Derya MAKTAV (İTÜ)  
Diğer Jüri Üyeleri : Prof. Dr. Filiz SUNAR (İTÜ)  
Yrd. Doç. Dr. Orhan KURT (KOÜ)  
Prof. Dr. Sıtkı KÜLÜR (İTÜ)  
Prof. Dr. Şenol KUŞÇU (ZKÜ)**

**ARALIK 2009**



## FOREWORD

I appreciate to many mentors, colleagues and friends surrounded me before and during my Ph.D. study. At first, my greatest gratitude is reserved for my supervisor, Prof.Dr. Derya Maktav, who admitted me as Ph.D. student and always encouraged me. Secondly Prof.Dr. Filiz Sunar and Dr. Orhan Kurt, the members of the thesis committee, advise me with their important opinions. I cannot forget Prof. Sunar's helps on establishing my contact with SPOT Image (France), and Dr. Kurt's sharing his deep experience on adjustment computation. He supports also his intercity travel allowance himself for many times to join the committee meetings.

I gratefully acknowledge Dr. Gürcan Büyüksalih who meets me both research on geospatial applications of space images and also with Dr. Karsten Jacobsen, who is leading doyen on his research topics and shares his insightful feedback on HRSI. Prof.Dr. Şenol Kuşçu, head of my Department in ZKU, provides always a comfortable work environment. Dr. M. Güven Koçak introduces me with Matlab and provides the GPS survey on this thesis. And to work with Mr. Murat ORUÇ is always a source of bliss. I cannot forget friendship of my former and actual colleagues in the Department. Dr. Hakan Yavaşoğlu, Dr. Ahmet Özgür Doğru, Mr. Umut Aydar, and Mr. Cihan Uysal from ITU disburden my task in ITU for many times. Dr. Şinasi Kaya and Prof. Dr. Dursun Zafer Şeker helps me in the Ph.D. project, and Prof.Dr. Umur Daybelge meet me with satellite orbits.

Dr. Stevlin Fotev, Dr. Taejung Kim, Dr. Hyung-Sup Jung, Dr. Franz Rottensteiner, Mr. Thomas Weser, Dr. Lionele Ibos, Dr. Pullur Variam Radhadevi, Dr. Francoise DeLussy, and Dr. Wolfgang Kornus kindly answered my questions via e-mail for many times. My thanks goes to also Prof. Clive S. Fraser for the help on Barista, Mr. Umut Güneş Sefercik and Mrs. Ulla Wissmann for their helps and guidance during my two Hannover visits. And Dr. Joanne Poon helps on the language check.

Belgüzar and Muharrem Topal countlessly hosted me in Istanbul, and also Aysel and Koray Yücel; Sevda and Fatih Tahtacı; Aşkın Polat, and Devrim Kurt, too.

I wish to thank my family, Selma, Mehmet and Altan Topan; Belgüzar, Muharrem and Erdal Köse; and Birsen and Ercan Tabakçayı.

My final acknowledgment is directed to Aysel, my lovely wife. She shared the good moments and gave me strength and serenity in the difficult times during these years.

December 2009

Hüseyin TOPAN  
Geomatic Engineer





## TABLE OF CONTENTS

	<u>Page</u>
<b>FOREWORD</b> .....	v
<b>TABLE OF CONTENTS</b> .....	vii
<b>LIST OF TABLES</b> .....	xi
<b>LIST OF FIGURES</b> .....	xiii
<b>SUMMARY</b> .....	xv
<b>ÖZET</b> .....	xvii
<b>1. INTRODUCTION</b> .....	<b>1</b>
1.1 Thesis Objectives .....	2
1.2 Thesis Outline .....	3
<b>2. LINEAR ARRAY SENSORS AND THEIR GEOMETRY</b> .....	<b>5</b>
2.1 Linear Array Sensors.....	5
2.1.1 Technologic background.....	6
2.1.2 Geometry of linear array sensors .....	6
2.2 Acquisition Techniques of Linear Array Sensors .....	8
2.2.1 Pushbroom technique.....	8
2.2.2 TDI technique .....	9
2.2.3 Slow-down technique.....	10
2.2.4 Staggered line array technique.....	11
2.3 Geometric Distortions and Influences of Linear Array HRSIs .....	11
2.3.1 Geometric distortions of linear array sensors .....	11
2.3.2 Distortions of optical system.....	13
2.3.3 Sensor geometry.....	14
2.3.4 Ground pixel size .....	15
2.3.5 Influence of earth curvature .....	16
2.3.6 Influence of Earth rotation .....	16
2.3.7 Influence of topographic relief.....	17
<b>3. GEOMETRIC CORRECTION OF LINEAR ARRAY HRSIs USING PARAMETRIC MODELS</b> .....	<b>19</b>
3.1 Overview of Geometric Correction of Linear Array HRSIs .....	19
3.2 Parametric Models.....	20
3.2.1 Colinearity equations .....	20
3.2.2 Existing parametric models.....	22
3.2.2.1 3D CCRS parametric model by Toutin.....	23
3.2.2.2 Model by Salamonowicz.....	25
3.2.2.3 Model by Gugan.....	26
3.2.2.4 Model by Konecny et al. ....	28
3.2.2.5 BLASPO and CORIKON by Jacobsen.....	29
3.2.2.6 Model by Kratky .....	30
3.2.2.7 Model by Westin.....	31
3.2.2.8 Trade-off by Orun and Natarajan.....	32
3.2.2.9 Model by Radhadevi and Ramachandran .....	33

3.2.2.10 Model by El-Manadili and Novak .....	34
3.2.2.11 Model by Poli.....	34
3.2.2.12 LOS vector adjustment model by Jung et al. ....	36
3.2.3 Overview of Existing Parametric Models.....	38
3.3 Model and Adjustment for Geometric Analysis .....	39
3.3.1 Generic Model .....	39
3.3.1.1 Coordinate systems and transformations .....	39
3.3.1.2 Modelling parameters .....	42
3.3.2 Modified Model for SPOT-5 .....	43
3.3.3 Adjustment.....	46
3.3.3.1 Pre-adjustment .....	49
3.3.3.2 Bundle adjustment .....	50
<b>4. GEOMETRIC ANALYSIS OF SPOT-5 HRG LEVEL 1A STEREO</b>	
<b>IMAGES .....</b>	<b>53</b>
4.1 Test Field.....	53
4.2 Description of Satellite, Image, and Auxiliary Data .....	53
4.2.1 SPOT-5 .....	54
4.2.2 Images and metadata used .....	55
4.2.3 Points observed by GPS survey .....	56
4.3 Programming.....	58
4.3.1 Loading data .....	59
4.3.2 Pre-processing.....	59
4.3.3 Pre-adjustment .....	59
4.3.4 Bundle adjustment .....	60
4.4 Geometric Analysis.....	60
4.4.1 Preface of Geometric Analysis .....	61
4.4.2 Results Achieved .....	64
4.4.2.1 Results based on first type pre-adjustment .....	64
4.4.2.2 Results based on second type pre-adjustment.....	73
4.4.3 Overview of Geometric Analysis .....	76
<b>5. CONCLUSION .....</b>	<b>79</b>
5.1 Discussion of Thesis .....	79
5.2 Further Work.....	80
<b>REFERENCES.....</b>	<b>83</b>
<b>APPENDICES .....</b>	<b>89</b>
<b>CURRICULUM VITAE.....</b>	<b>111</b>

## ABBREVIATIONS

<b>CCD</b>	: Charge-Coupled Device
<b>CCRS</b>	: Canada Centre for Remote Sensing
<b>CCS</b>	: Camera Coordinate System
<b>CICS</b>	: Conventional Inertial Coordinate System
<b>CMOS</b>	: Complementary Metal–Oxide Semiconductor
<b>CNES</b>	: Centre National d'Études Spatiales
<b>CTCS</b>	: Conventional Terrestrial Coordinate System
<b>DEM</b>	: Digital Elevation Model
<b>DIMAP</b>	: Digital Image MAP
<b>DLT</b>	: Direct Linear Transformation
<b>DORIS</b>	: Doppler Orbitography Radiopositioning Integrated by Satellite
<b>EOP</b>	: Exterior Orientation Parameter
<b>GCP</b>	: Ground Control Point
<b>GCS</b>	: Ground Coordinate System
<b>GIS</b>	: Geographic Information System
<b>GSD</b>	: Ground Sampling Distance
<b>GMST</b>	: Greenwich Mean Sidereal Time
<b>GNSS</b>	: Global Navigation Satellite System
<b>GPS</b>	: Global Positioning System
<b>HRG</b>	: High Resolution Geometry
<b>HRS</b>	: High Resolution Stereoscopic
<b>HRSI</b>	: High Resolution Space Image
<b>ICP</b>	: Independent Check Point
<b>ICS</b>	: Image Coordinate System
<b>IFOV</b>	: Instantaneous Field of View
<b>IMU</b>	: Inertial Measurement Unit
<b>INS</b>	: Inertial Navigation System
<b>IPI</b>	: Institute of Photogrammetry and Geoinformation
<b>IRS</b>	: Indian Remote Sensing Satellite
<b>LSA</b>	: Least Square Adjustment
<b>LOS</b>	: Line-of-Sight
<b>MTF</b>	: Modulation Transfer Function
<b>NRCS</b>	: Navigation Reference Coordinate System
<b>OCS</b>	: Orbital Coordinate System
<b>PCS</b>	: Payload Coordinate System
<b>PPM</b>	: Piecewise Polynomial Functions
<b>PSG</b>	: Pixel Size on Ground
<b>RFM</b>	: Rational Function Model
<b>RMSE</b>	: Root Mean Square Error
<b>SCS</b>	: Scanline Coordinate System
<b>SDLT</b>	: Self-Calibrating DLT
<b>SPOT</b>	: Satellite Pour l'Observation de la Terre
<b>SWIR</b>	: Short Wave Infrared

**VNIR** : Visible and Near Infrared  
**TDI** : Time Delay and Integration  
**THR** : Very High-Resolution  
**TLS** : Tree-Line Sensor  
**TÜBİTAK** : Türkiye Bilimsel ve Teknik Araştırma Kurumu  
**2D** : Two Dimensional  
**3D** : Three Dimensional

## LIST OF TABLES

	<b><u>Page</u></b>
<b>Table 4.1:</b> Specifications for SPOT-5 HRG level 1A images.....	55
<b>Table 4.2:</b> Configurations of choosing EOP as adjustment parameter.....	63
<b>Table 4.3:</b> RMSE of GCPs and ICPs using approximate and adjusted look angles.....	64



## LIST OF FIGURES

	<u>Page</u>
<b>Figure 2.1:</b> Sensors for data acquisition (Poli, 2005).....	5
<b>Figure 2.2:</b> Linear array imaging.....	7
<b>Figure 2.3:</b> Various designs of linear arrays.....	7
<b>Figure 2.4:</b> Pushbroom technique (left) and corresponding image (right).....	9
<b>Figure 2.5:</b> TDI technique with three stages (Schöder et al., 2001).....	10
<b>Figure 2.6:</b> Slow-down technique (Jacobsen, 2005).....	10
<b>Figure 2.7:</b> Staggered CCD lines (left) and relation of pixel and GSD (right)....	11
<b>Figure 2.8:</b> Geometric distortions of one segment linear array sensor.....	12
<b>Figure 2.9:</b> Unique geometric distortions of two segment linear array sensor....	13
<b>Figure 2.10:</b> Geometric distortions of three overlapped linear array segments....	14
<b>Figure 2.11:</b> Influences of sensor geometry.....	15
<b>Figure 2.12:</b> Difference in ground pixel size in along track view.....	16
<b>Figure 2.13:</b> Influence of Earth curvature.....	16
<b>Figure 2.14:</b> Rotation of Earth during nadir acquisition (above) and corresponding corrected image (below).....	17
<b>Figure 2.15:</b> Influence of topographic relief.....	17
<b>Figure 3.1:</b> Relationship between image and ground coordinate systems in aerial photogrammetry with film based or digital frame images.....	22
<b>Figure 3.2:</b> Transformation from ICS to GCS.....	40
<b>Figure 3.3:</b> NRCS and look angles ( $\psi_x$ and $\psi_y$ ) (left) (SPOT Image, 2002), and bundle rays given by the SPOT-5 look angles (Weser et al., 2008)	44
<b>Figure 4.1:</b> Imaging sensors and some instruments of SPOT-5 satellite (above) and the CCD array of panchromatic band (below) (SPOT Image, 2002).....	54
<b>Figure 4.2:</b> Distribution of points on the image dated 13 <sup>th</sup> and 14 <sup>th</sup> August 2003 above and below, respectively.....	57
<b>Figure 4.3:</b> One of the points selected on road intersection (left hand-side) and scene of GPS observation in the field (right hand-side).....	58
<b>Figure 4.4:</b> Main steps of developed program (GeoSpot-1.0).....	58
<b>Figure 4.5:</b> Plotting of positions of both satellite (given in metadata and estimated for each points), and points.....	60
<b>Figure 4.6:</b> Steps of pre-adjustment.....	61
<b>Figure 4.7:</b> Various configuration of point distribution (H: Homogenous distribution, G: Grouped distribution, +: GCP, $\diamond$ : ICP).....	62
<b>Figure 4.8:</b> Plot of residual errors in planimetry (diagonal) and in height (up- down) at all GCPs (H-0). left: using approximate look angles, right: using pre-adjusted look angles.....	65

<b>Figure 4.9:</b> Plot of residual errors in planimetry (diagonal) and in height (up-down) at GCPs and ICPs for homogenously distributed point sets. (above: results of pre-adjusted look angles, below: results of bundle adjusted look angles, H: Homogenous distribution, G: Grouped distribution, •: GCP, o: ICP).....	66
<b>Figure 4.10:</b> Plot of residual errors in planimetry (diagonal) and in height (up-down) at GCPs and ICPs for grouped point sets (from above to below: G-A, G-B, G-C). left: results of pre-adjusted look angles, right: results of bundle adjustment. (H: Homogenous distribution, G: Grouped distribution, •: GCP, o: ICP).....	67
<b>Figure 4.11:</b> Graphical representation of accuracy of GCPs and ICPs in point sets homogenously distributed.....	70
<b>Figure 4.12:</b> Graphical representation of accuracy of GCPs and ICPs in point sets homogenously distributed.....	71
<b>Figure 4.13:</b> Plot of residual errors in planimetry (diagonal) and in height (up-down) at GCPs and ICPs for some point sets with respect to EOP sets. (H: Homogenous distribution, G: Grouped distribution, •: GCP, o: ICP).....	72
<b>Figure 4.14:</b> Plot of residual errors in planimetry (diagonal) and in height (up-down) at all GCPs for some EOP sets.....	74
<b>Figure 4.15:</b> Plot of residual errors in planimetry (diagonal) and in height (up-down) for some sets of points and EOPs. (left: pre-adjustment, right: bundle adjustment, H: Homogenous, G: Grouped, •: GCP, o: ICP).....	75
<b>Figure 4.16:</b> Graphical representation of accuracy of GCPs and ICPs in point sets $P_S$ and A for the homogenously distributed points. $\overline{LP}$ : pre-adjusted look angles and EOPs, B: bundle adjustment.....	77
<b>Figure A.2.1:</b> Image coordinate system.....	95
<b>Figure A.2.2:</b> Scanline coordinate system.....	96
<b>Figure A.2.3:</b> Camera coordinate system.....	96
<b>Figure A.2.4:</b> Orbital and ground coordinate systems.....	97
<b>Figure A.3.1:</b> Contraclockwise rotations.....	99
<b>Figure A.3.2:</b> Keplerian elements in CICS and GCS.....	101
<b>Figure A.4.1:</b> Point intersection from sreteo images .....	105



# **GEOMETRIC ANALYSIS OF HIGH RESOLUTION SPACE IMAGES USING PARAMETRIC APPROACHES CONSIDERING SATELLITE ORBITAL PARAMETERS**

## **SUMMARY**

In the last two decades the imaging technology in aerial and space based missions grew up thanks to especially the imaging technology based on linear array sensors and reducing ground sampling distance. Now high resolution space images with about 40 cm resolution are available. This improvement supports developments on geospatial applications of these images. The geometric correction process becomes more important now than in the past for this purpose. This thesis is focused on the geometric analysis of high resolution space images using parametric (rigorous) approaches ignoring non-parametric (deterministic) ones. Parametric approaches consider imaging geometry, orbital and attitude parameters of satellite, and define the real geometry between image and ground on contrary to the non-parametric ones.

The analysed images are only one set of stereo SPOT-5 HRG level 1A images acquired by linear array sensors. So this technology is subjected following brief information about the sensors for data acquisition. Then the existing parametric approaches for the geometric correction of distortions and influences are summarized following definition of the distortions and influences on linear array images.

The generic model which establishes the geometric relationship between image and ground coordinate systems is defined at first (Weser *et al.*, 2008). Then the modification and simplification to generic model are explained taking into account the image characteristics (SPOT Image, 2002; Fotev *et al.*, 2005). The ground coordinates and their accuracies are attained by adjustment process requiring both pre- and bundle adjustment stages.

The test field covering Zonguldak (Turkey), specifications of SPOT-5 HRG level 1A image, brief information about SPOT-5 satellite, and auxiliary data used are presented before the section of MATLAB programming which includes the workflow of the programme GeoSpot-1.0 developed by the author.

The most important issue for the purpose of estimating the true ground coordinate via the stereo images is adjusting the interior orientation components, i.e. look angles to be corrected in the pre-adjustment process, in this thesis. However the effects of exterior orientation parameters on the accuracy evaluation have to be investigated establishing various sets of them. The adjustment requires selection of suitable set of these parameters. The results of geometric analysis are presented with the help of graphical figures and the tables at the end of this thesis. The section Conclusion contains the general overview and comments on the thesis and its results.

Some auxiliary explanations are given in the Appendices.



# YÜKSEK ÇÖZÜNÜRLÜKLÜ UYDU GÖRÜNTÜLERİNİN UYDU YÖRÜNGE PARAMETRELERİNİ DİKKATE ALAN PARAMETRİK MODELLERLE GEOMETRİK ANALİZİ

## ÖZET

Son yirmi yılda doğrusal dizi algılama teknolojisi sayesinde hava ve uzay bazlı görüntüleme teknolojileri önemli ölçüde gelişmiş ve yer örnekleme aralığı küçültülmüştür. Günümüzde yaklaşık 40 cm çözünürlüğe sahip uydu görüntüleri elde edilebilmektedir. Bu gelişme bu görüntüler yardımıyla konumsal uygulamaların gelişimini de desteklemiştir. Bu nedenle geometrik düzeltme işlemi geçmişe nazaran daha önemli hale gelmiştir. Bu tez çalışması parametrik olmayan yaklaşımları göz ardı ederek yüksek çözünürlüklü uydu görüntülerinin parametrik modellerle analizini amaçlamaktadır. Parametrik modeller, parametrik olmayanların aksine görüntüleme geometrisini ve uydunun yörünge ve durum parametrelerini dikkate alır ve görüntü ve yeryüzü arasındaki gerçek geometrik ilişkiyi tanımlar.

Analizi yapılan görüntüler doğrusal dizi algılayıcılar tarafından algılanan bir çift stereo SPOT-5 HRG düzey 1A görüntüsüdür. Bu nedenle veri elde etmek için kullanılan algılayıcılardan bahsedildikten sonra doğrusal dizi algılama teknolojisi hakkında bilgi verilmiştir. Doğrusal dizi görüntülerinin taşıdıkları geometrik bozulma ve etkiler açıklandıktan sonra bunların düzeltilmesi için kullanılan mevcut parametrik modeller tanıtılmıştır.

Öncelikle, görüntü ve yer koordinat sistemleri arasındaki geometrik ilişkiyi tanımlayan genel bir model tanımlanmıştır (Weser *et al.*, 2008). Sonrasında kullanılan görüntünün özelliklerini göz önüne alarak genel model değiştirilmiş ve basitleştirilmiştir (SPOT Image, 2002; Fotev *et al.*, 2005). Yer koordinatları ve bunların doğruluğu, öncül ve demet dengeleme adımlarının her ikisine gerek duyan dengeleme işlemiyle elde edilmektedir ve her biri ayrı bölümlerde açıklanmıştır.

Zonguldak'ı kapsayan test alanı, SPOT-5 HRG düzey 1A görüntüsünün özellikleri, SPOT-5 uydusu hakkında özet bilgi, kullanılan ek veriler ve sonrasında yazar tarafından MATLAB ortamında geliştirilen GeoSpot-1.0 yazılımının akış şeması anlatılmıştır.

Bu tezde stereo görüntüler yardımıyla doğru görüntü koordinatlarının elde edilmesi sürecinde en önemli unsur ön dengeleme ile düzeltilen iç yöneltme bileşenleri yani bakış açılarıdır. Bununla birlikte dış yöneltme elemanlarının doğruluk üzerindeki etkileri de farklı parametre setleri oluşturularak incelenmiştir. Dengelemede bu parametrelerin uygun şekilde seçimi gereklidir. Geometrik analiz sonuçları grafik şekiller ve tablolar yardımıyla tezin sonunda sunulmuştur. Sonuç bölümünde ise tez ve sonuçlar hakkında genel bir değerlendirme yapılmaktadır.

Gerekli bazı açıklamalar Ekler bölümünde verilmiştir.



## 1. INTRODUCTION

The high resolution space images (HRSIs) usually contain geometric distortions and influences and are not directly used in geospatial applications. For this reason, correction of geometric distortions and influences are necessary for the production of corrected image related products to allow these products to be registered, compared, combined etc. pixel by pixel and used in a GIS environment (Toutin, 2003a).

Since the first-decades of remote sensing the geometric correction has become more important for some of the following reasons:

- The geometric resolution is sub-meter level while previously it was coarse (for instance Landsat-1 has around 80-100 m ground sampling distance (GSD)).
- The images are off-nadir viewing whereas previously were nadir viewing.
- The products are digital while previously were hard-copy resulting from image processing.
- The interpretation of final products is performed on the computer whereas previously it was performed as visually.
- The fusion of multi-source images (from different platforms and sensors) is in general use while previously the fusion and integration of multi-source and multi-format data did not exist in the past.

The process of generating a corrected image is called by various terms, i.e. orthoimage generation, georectification, geolocation, georeferencing, geopositioning, geometric correction or direct or indirect sensor orientation. Nevertheless, the main aim in this process is to establish the geometric relationship between image and ground coordinate systems, and remove the geometric distortions and influences of image, assuming image coordinate as observation. The geometric relationship between these two coordinate systems is generally subject of scale, shift and rotation which are generally assumed as parameters. However, the observations and parameters can be set various depending on the adjustment model.

The geometric distortions and influences of the linear array HRSIs are caused by different sources. The characteristics of linear array sensors and their having geometric distortions and influences are briefly explained following the overview of sensors for data acquisition.

## **1.1 Thesis Objectives**

The main objective of this thesis is to perform geometrical analysis of stereo SPOT-5 HRG level 1A images based on a linear array imaging technology. The preferred parametric approach is dedicated for these images considering their imaging geometry, and orbital and attitude parameters of satellite. The analysis consists of three main issues. These are:

1. The effects of interior orientation defined by look angles subjected with and without its pre-adjustment.
2. The effects of exterior orientation parameters (EOPs) with and without pre-adjustment.
3. The correlation among EOPs.

The following steps are required for the issues mentioned above:

- Define the required auxiliary coordinate systems between image and ground coordinate systems.
- Establish generic parametric model; the geometric relationship between image- and ground-coordinate systems will be determined considering imaging geometry and orbital and attitude parameters of satellite.
- Modify and simplify the parametric model for the specifications of the images used in this thesis.

All computations including pre-processing the auxiliary data, pre-adjustment and bundle adjustment are performed in the programme called GeoSpot-1.0 developed by the author in MATLAB environment. Graphical presentations and tables of results helps to discuss the results.

Many images were available for the purpose of this thesis. Nevertheless, of all images acquired by the various sensors, only the auxiliary information required for

the parametric model to be discussed was provided for SPOT-5 HRG images. Thus, these images with 5 m GSD were preferred in this thesis. However various images with higher geometric resolution than SPOT-5 HRG existed. Here, the term “high resolution” has to be discussed. There is no precise definition on this term in the literature. In spite of the fact that SPOT-5 is three years older than IKONOS (panchromatic images with 1 m GSD), SPOT Image names its camera as High Resolution Geometric (HRG). Moreover, the aimed research is independent than the GSD in this thesis. If the geometric relationship of the sensor is known and the auxiliary data is available, the parametric model can be used for all spaceborne, airborne or terrestrial images.

## **1.2 Thesis Outline**

The images investigated in this thesis are based on the linear array sensor technology. The background of this technology is described in the second section. The geospatial applications of HRSIs requires geometric correction of these images. So the source of geometric distortions and influences carried by the images are summarized, and the geometric correction methods are explained including the existing approaches in the third section.

The fourth section consists of the auxiliary coordinate systems required to establish the geometric relationship between image and the ground, the generic and the modified and also simplified model, and the geometric analysis. Finally the fifth and the last section concludes the thesis and its results recalled.

Some of the auxiliary information needed are given in the Appendices.





## 2. LINEAR ARRAY SENSORS AND THEIR GEOMETRY

Since the distortions and influences are partly related to the imaging systems, they have to be characterized by understanding their acquisition geometry. This section explains the characteristics of linear array sensors and their geometry.

### 2.1 Linear Array Sensors

Various sensors for data acquisition are available as shown in Figure 2.1. Firstly, the sensors can be divided as passive and active considering the energy source. The passive sensors obtain the energy which comes from an external source while the active sensors are the source of observed energy themselves. Both passive and active sensors have tasks of imaging or non-imaging (Poli, 2005).

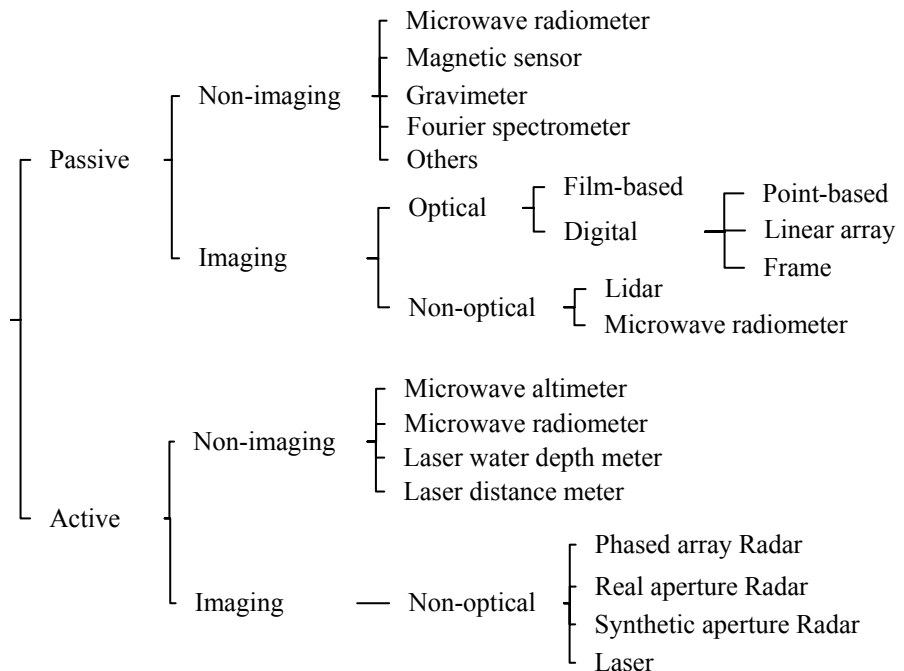


**Figure 2.1:** Sensors for data acquisition (Poli, 2005).

Linear array sensors, generally used in remote sensing applications, are classified as passive, optical and digital sensors aimed imaging. The Radar sensors, which are active and non-optical sensors and aimed imaging, become mostly preferred systems for the purposes such as observation of cloudy areas, generation digital elevation model (DEM), determination of surface-deformation or monitoring the marine-traffic at midnight etc.

The technologic background of the linear array sensors is presented following brief information related to the data acquisition.

### **2.1.1 Technologic background**

Linear array sensors used for imaging purposes depends mainly on charge-coupled device (CCD) technology which was invented by George Smith and Willard Boyle at AT&T Bell Labs in 1969 (Wikipedia, 2007). The CCD is an imaging sensor, consisting of an integrated circuit containing an array of linked, or coupled, light-sensitive capacitors. Complementary metal–oxide semiconductor (CMOS), as an alternative technology, is invented by Frank Wanlass at Fairchild Semiconductor in 1963 (Wikipedia, 2007). CMOS refers to both a particular style of digital circuitry design, and the family of processes used to implement that circuitry on integrated circuits (chips). The CCD technology is used mostly on helicopters, aircrafts and satellites for Earth observation and also for motion capture, human body modelling and object modelling for medical, industrial, archaeological and architecture applications; on the contrary the CMOS technology in linear arrays is used only for close range applications. Only some airborne frame cameras use CMOS in recent years. The advantages of CCD versus CMOS are its superior image performance (as measured in quantum efficiency and noise) and flexibility at the expense of system size (Poli, 2005). Further technical information of CCD and CMOS technologies are available in various references.

### **2.1.2 Geometry of linear array sensors**

Sensor elements or detectors in linear array sensors (i.e. pixels) are arranged along a line in the focal plane (Figure 2.2). The observed object, i.e. Earth surface, is projected on the sensor element, and the image is generated by the charge of the related detector. The construction of a linear array is easier than area arrays, and mechanical scanning is not necessary. For covering more area, the arrays are built as

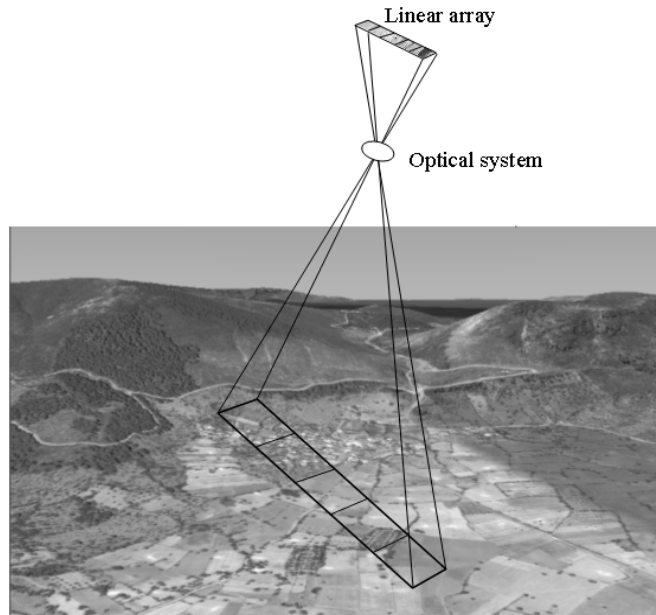


**Figure 2.2:** Linear array imaging.

longer or designed as a combination of segments. The existing configurations of line design are (Poli, 2005):

- The pixels are placed in a single line (Figure 2.3 a). SPOT-5 HRG has 12000 elements in a line.
- A line consists of two or more segments (Figure 2.3 b). QuickBird with 27000 elements is a combination of six segments, each of 3000 elements (Liedtke, 2002).

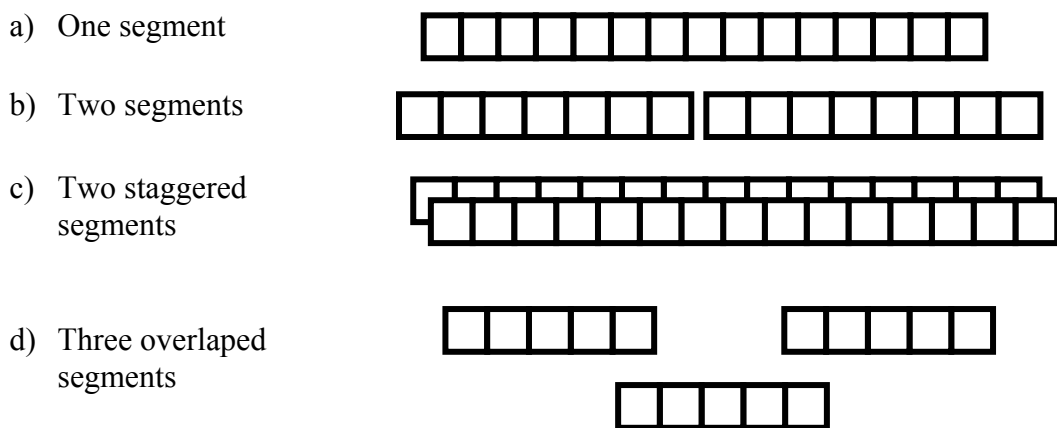


**Figure 2.3:** Various designs of linear arrays.

- Two segments placed parallel on the longer side are staggered as half-element in both directions (Figure 2.3 c). SPOT-5 Supermode (2.5 m GSD) and OrbView-3 panchromatic (1 m GSD) images are generated by staggered linear arrays, each pixel has 5 m and 2 m size on the ground, respectively.
- And the segments are placed with overlaps (Figure 2.3 d). IRS-1C and ALOS PRISM have three and four segments overlapping on each other, respectively.

Various acquisition techniques of linear array sensors are available as explained in the following section.

## 2.2 Acquisition Techniques of Linear Array Sensors

A linear array is instantaneously projected on the object. The integration time depends on velocity of platform, for instance 0.88364 ms for IRS-1C panchromatic band (5.8 m GSD) or 0.14285 ms for IKONOS panchromatic band. This short time based on the pushbroom technique is not enough to observe sufficient energy from the object. For this reason, the integration time can be extended by other techniques, such as time delay and integration (TDI) or slow-down techniques; or the projection of pixel on the ground can be enlarged producing the image with halved size by staggered line arrays. The acquisition techniques used for linear array sensors are explained below.

### 2.2.1 Pushbroom technique

The basic of pushbroom technique is, as shown by Figure 2.4, a linear array sensor mounted on a moving platform sweeping out a line on the Earth surface during the motion of platform. The instantaneous view plane is perpendicular to the direction of motion. Each elements of linear array generates the charge as a response to the energy from the projected-pixel on the ground during the integration time. The generated charge as a response to the incoming energy is discharged fast enough to independently collect the energy of neighbored pixels projected on the ground (Gupta and Hartley, 1997).

The pixel size on ground (PSG) in the direction of motion ( $psg_x$ ) is defined by velocity of platform ( $V$ ) and line interval ( $\Delta t$ ):

$$psg_x = V.\Delta t \quad (2.1)$$

and the  $psg_y$ , perpendicular to the direction of motion, becomes:

$$psg_y = \frac{p.H}{c} \quad (2.2)$$

where  $psg_x$  and  $psg_y$  are pixel size on ground in the direction of motion (x) and perpendicular to the direction of motion (y), respectively,  $V$  is velocity of platform,  $\Delta t$  is line interval,  $p$  is pixel size ( $p=p_x=p_y$ ),  $H$  is flying height, and  $c$  is focal length.

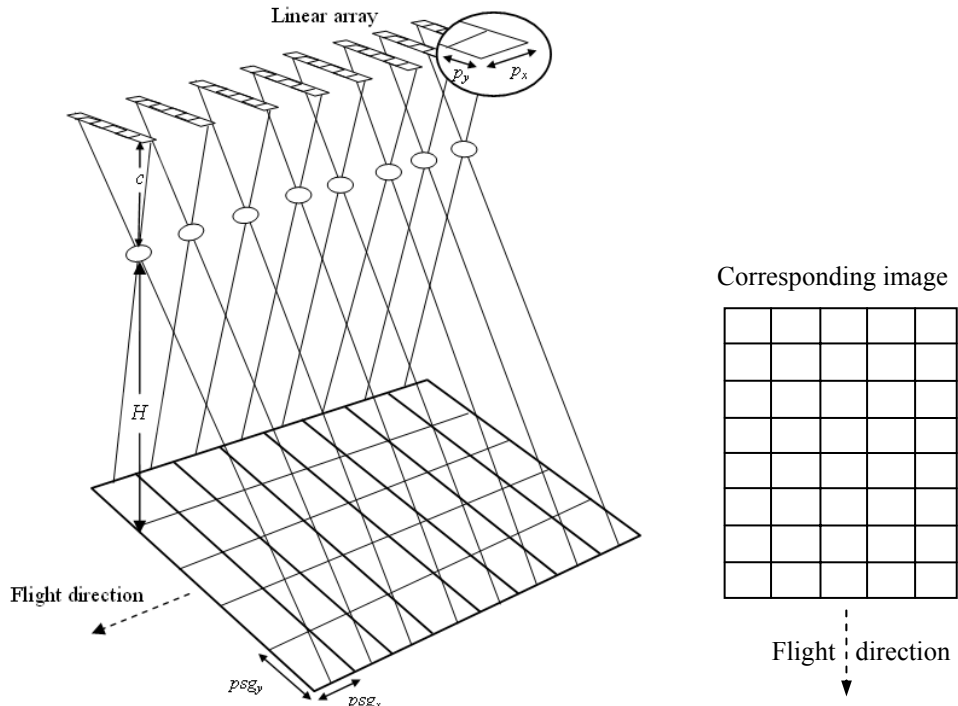


**Figure 2.4:** Pushbroom technique (left) and corresponding image (right).

Since the integration time is not sufficient for acquisition of enough energy, for instance  $\Delta t$  is 0.88364 ms for IRS-1C panchromatic band, 0.75210 ms for SPOT-5 HRG or 0.14285 ms for IKONOS panchromatic band, an extension of  $\Delta t$  is necessary by TDI or slow-down techniques with or without the staggered line arrays.

### 2.2.2 TDI technique

The TDI, in other words drift-scan, is a technique based on the principle of multiple generation of the charge as a response to the energy from the projected-pixel on the ground in  $N$  stages. Consequently, the object is observed by not only one, but also  $N$

pixels in a line along the motion (Figure 2.5). The final charge is a sum of charges in the previous stages. IKONOS and QuickBird are equipped by the TDI with 13 stages. Nevertheless, QuickBird is launched at altitude of 450 km instead of its planned altitude of 680 km, in order to reduce the GSD for higher geometric resolution. Consequently QuickBird uses also slow-down technique for increasing the imaging time (Jacobsen, 2005). OrbView-3 is other satellite which uses slow-down technique, but this satellite is equipped by staggered line arrays instead of TDI.

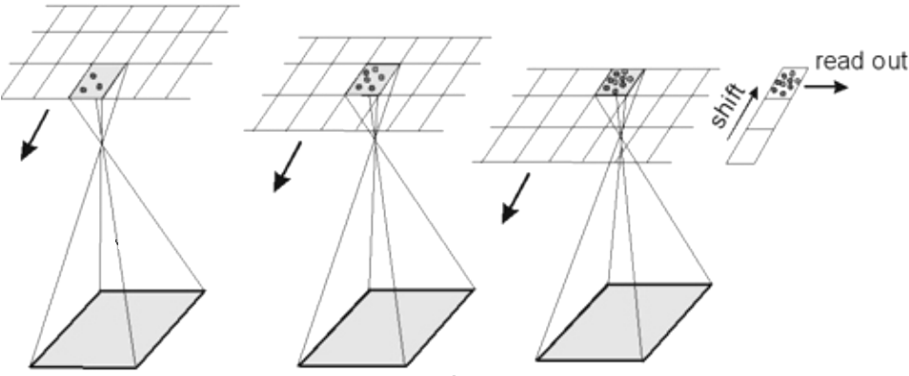


Figure 2.5: TDI technique with three stages (Schöder et al., 2001).

**2.2.3 Slow-down technique**

The slow-down technique is based on the principle that permanently changing the view-direction against direction of motion during imaging. So, the imaging time is increased by the reducing the speed of sensor-track on the ground (Jacobsen, 2005). In Figure 2.6, (a) means distance of unchanged view direction against the orbit, (b) means distance of slow down technique. The  $b/a$  is 1.4 for OrbView-3 and 1.6 for QuickBird (Topan *et al.*, 2009).

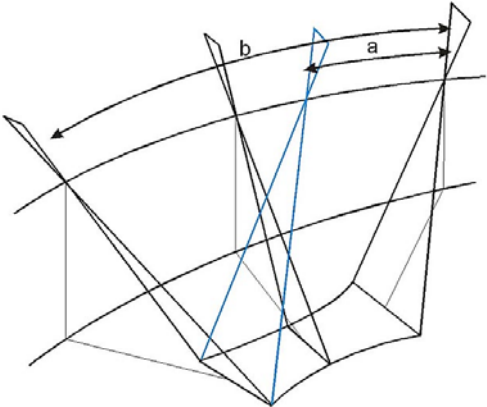
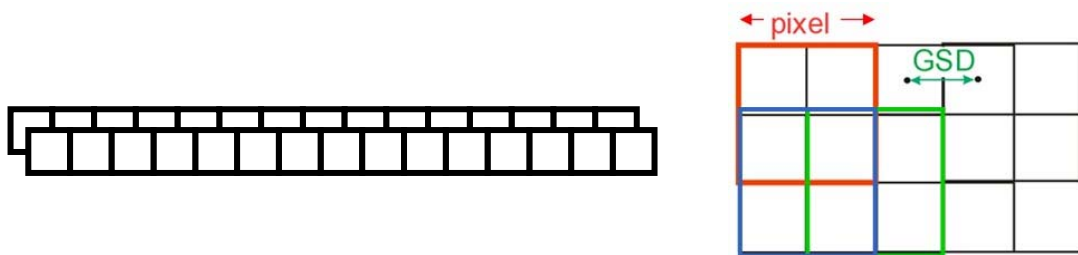


Figure 2.6: Slow-down technique (Jacobsen, 2005).

## 2.2.4 Staggered line array technique

Staggered line arrays depends on the concept that two line arrays are shifted half-pixel along both row and column directions (Figure 2.7). The process of generation an image by this technique consists in quincunx interpolation, deconvolution and denoising. Quincunx interpolation computes radiometric information over a halved pixel, deconvolution compensates for low modulation transfer function (MTF) values for high spatial frequencies and denoising reduces the noise level enhancement due to deconvolution (Latry and Rouge, 2003). The SPOT-5 Supermode (2.5 m GSD) and OrbView-3 panchromatic (1 m GSD) images are generated by 5 m and 2 m pixel size on the ground, respectively The relation between pixel and GSD is depicted in the Figure 2.7. As comparison of information content of TDI and staggered line arrays, IKONOS panchromatic image with TDI technique has sharper edges than OrbView-3 with staggered line arrays (Topan et al., 2006).



**Figure 2.7:** Staggered CCD lines (left) and relation of pixel and GSD (right).

## 2.3 Geometric Distortions and Influences of Linear Array HRSIs

The linear array HRSIs have significant geometric distortions denying the use as map base products. The distortions are sourced by acquisition system (i.e. imaging sensor, platform, incidence angle etc.), curvature and rotation of Earth and topographic relief (Toutin, 2003a). These various sources of distortions are explained in the following sections.

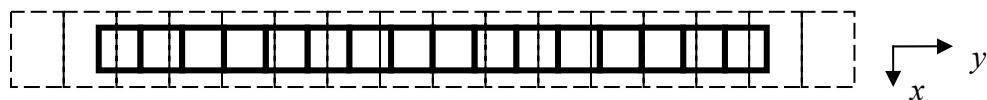
### 2.3.1 Geometric distortions of linear array sensors

The images used in this thesis are acquired by linear array sensors with various designs as explained by Figure 2.3 in Section 2.1.2. The distortions of linear array sensor are related to these designs. As general, the distortions corrected by suitable functions are:

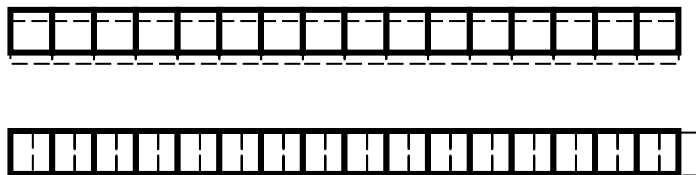
- Change of pixel dimension,
- Shift or rotation of the segments in focal plane,
- Line bending or curvature.

In the case of one segment linear array sensor, the geometric distortions are explained in the following:

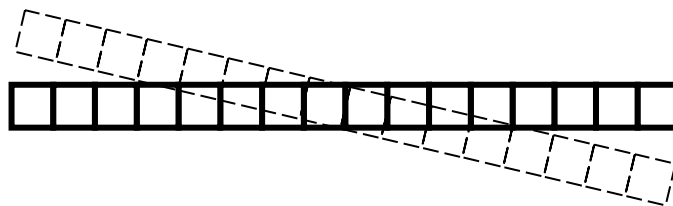
- The change of pixel dimension affects the image scale (Figure 2.8 a). The error in  $y$  direction is highly correlated to the focal length variation, the radial distortion and the scale factor in  $y$ -direction (Poli, 2005).
- Shift in  $x$ - and  $y$ -directions are possible as depicted in Figure 2.8 b.
- A horizontal rotation in the focal plane is available (Figure 2.8 c).
- Line bending or curvature distortion is exhibited in focal plane (Figure 2.8 d).



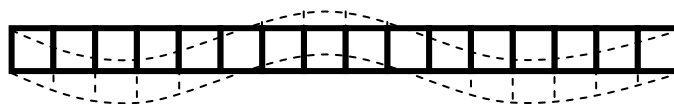
a) Effects of pixel size change in  $x$ - and  $y$ -directions.



b) Shift in  $x$ -(above) and in  $y$ - (below) directions.



c) Horizontal rotation of line array sensor in the focal plane.



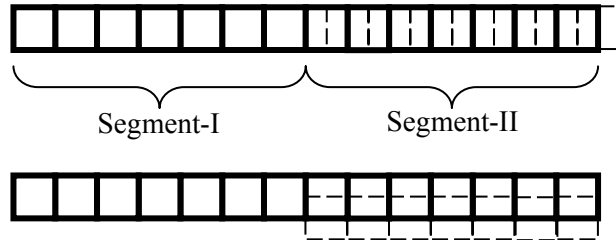
c) Line bending or curvature distortion in focal plane.

**Figure 2.8:** Geometric distortions of one segment linear array sensor.

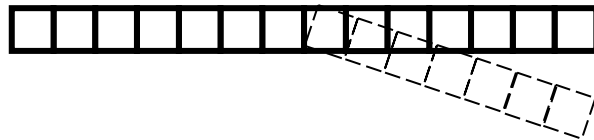


The unique geometric distortions in two segments linear array sensors are:

- Shift in  $x$ - and  $y$ -directions (Figure 2.9 a). One segment is shifted against its nominal position.
- One segment can be horizontal rotated in focal plane (Figure 2.9 b).



a) Shift of a segment in  $y$ - (above) and  $x$ - (below) directions.



b) Rotation of a segment.

**Figure 2.9:** Unique geometric distortions of two segments linear array sensor.

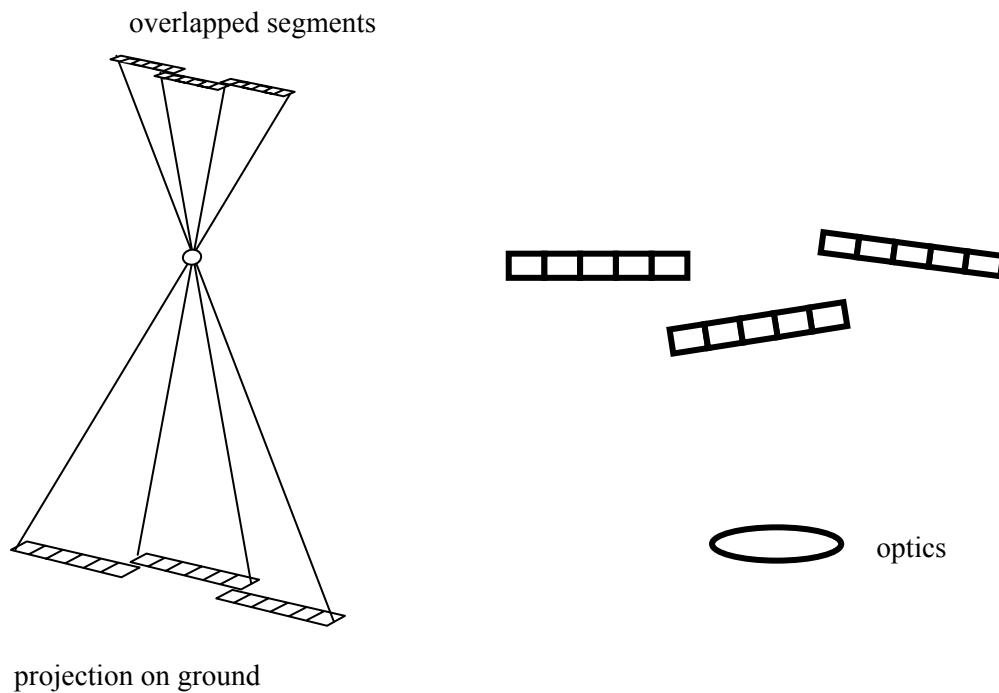
The three overlapped linear array segments have following unique distortions:

- The shift and rotation of linear arrays in focal plane causes different locations of each segment at the same integration time (Figure 2.10 a).
- The vertical rotation and different focal length of the overlapped segments change scale in  $y$ -direction as shown by Figure 2.10 b (Jacobsen, 1998).

### 2.3.2 Distortions of optical system

The existing distortions of optical system are:

- The shift of principal point in  $x$ - and  $y$ -directions,
- The change of focal length ( $c$ ),
- The symmetric lens distortions,
- The decentering lens distortions,
- The scale variation in  $x$ - and  $y$ -directions.



- a) Different location of overlapped segments.      b) Possible vertical rotation and different focal length of overlapped segments.

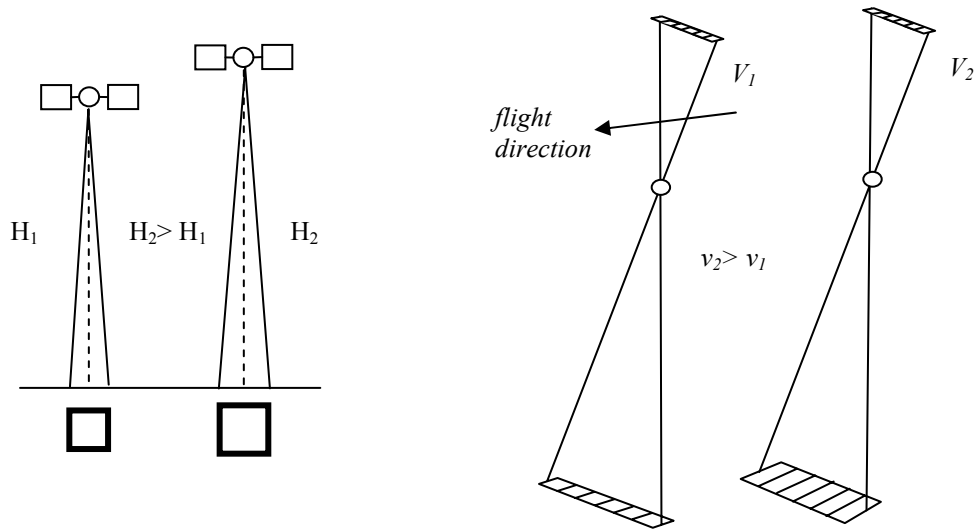
**Figure 2.10:** Geometric distortions of three overlapped linear array sensors.

The lens distortions can be negligible since the field of view of linear array sensors is generally very narrow (Orun, 1990; Yamakawa, 2004).

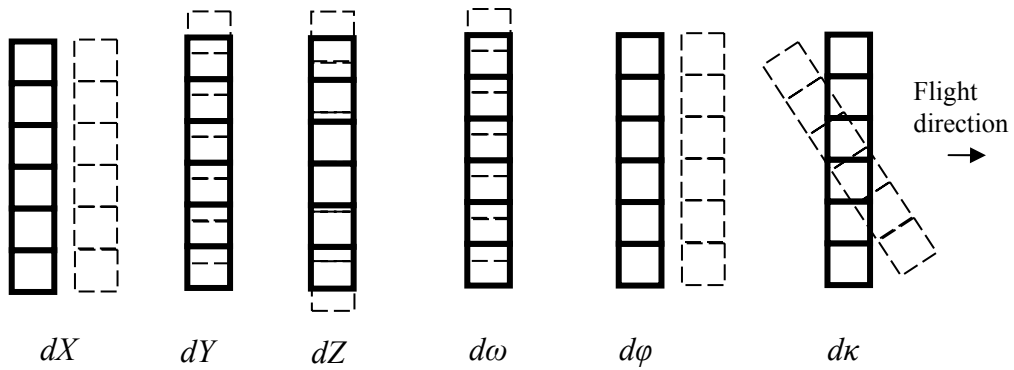
### 2.3.3 Sensor geometry

The platforms, artificial satellites in this scope, have a constant sun-synchronous orbit. However the sensor geometry is mainly related to orbit and Earth (elliptic movement, variable Earth gravity etc.). Depending on the acquisition time and the size of image, the influences of sensor geometry are:

- Platform altitude variation in combination with sensor focal length, Earth's flatness and topographic relief changes the pixel size on the ground (Figure 2.11 a).
- Platform velocity variations change the line spacing or create line gaps/overlaps (Figure 2.11 b).



a) Changing caused by altitude variation of platform.      b) Changing along flight direction caused by platform velocity variation.



c) Influences of small changes of attitude and position of platform.

**Figure 2.11:** Influences of sensor geometry.

- Small changes of platform position (in  $X$ ,  $Y$  and  $Z$  directions) and rotation angles ( $\omega$ ,  $\varphi$  and  $\kappa$ ) changes the orientation and the shape of images (Michalis, 2005) (Figure 2.11 c).

### 2.3.4 Ground pixel size

The sensors have capability of off-nadir viewing in across-track, in along-track or in flexible directions with the help of mirror or reaction wheels (Jacobsen, 2005). Since their angular instantaneous field of view (IFOV) is constant, this off-nadir viewing allows difference of ground pixel size (Figure 2.12). This difference is seen in  $y$ -direction of across-track images, in  $x$ -direction of along-track images and in both  $x$ - and  $y$ -directions of flexible images. The images have to be corrected as if observed in nadir view.

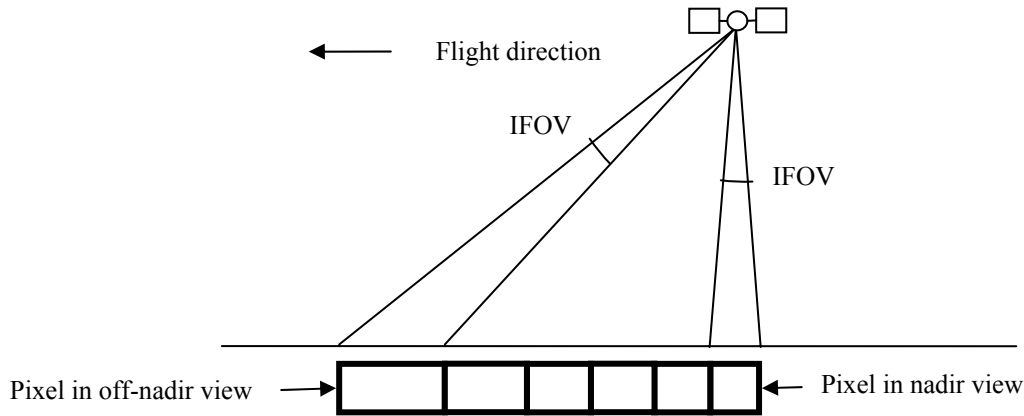


**Figure 2.12:** Difference in ground pixel size in along track view.

### 2.3.5 Influence of earth curvature

The Earth curvature causes the influence of pixel size on the ground (Figure 2.13). This influence is seen in  $y$ -direction of across-track images, in  $x$ -direction of along-track images and in both  $x$ - and  $y$ -directions of flexible images. This influence is more realized in the images covering longer-distance rather than shorter-distance.

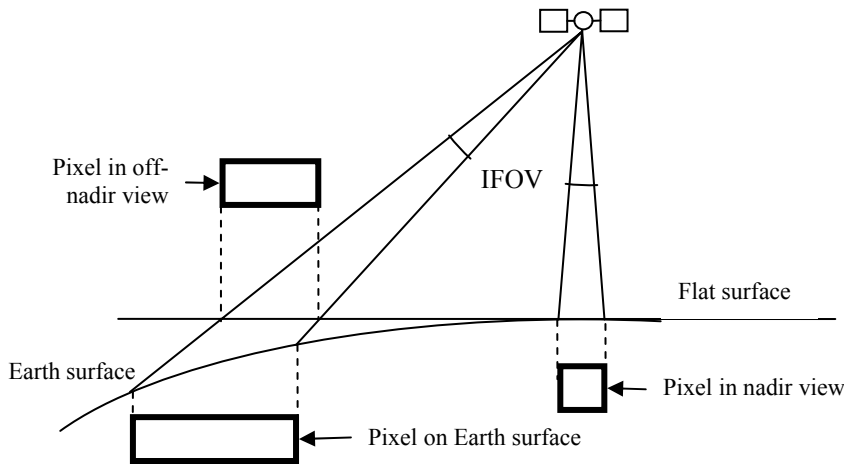


**Figure 2.13:** Influence of Earth curvature.

### 2.3.6 Influence of Earth rotation

During the image acquisition, the Earth rotates from west to east around itself causing an influence on the image. The sensor acquires the object with longitude  $\lambda_1$  at time  $t_1$  whereas it takes the object longitude with  $\lambda_2$  at time  $t_2$  (Figure 2.14). Magnitude of this influence is based on the relative velocities of satellite and Earth,

and length of the image even (Richards and Jia, 1999). The corrected image is a left-oriented image. Some satellites such as SPOT-5 have yaw steering mode to recover this influence during the acquisition of image (SPOT Image, 2002).

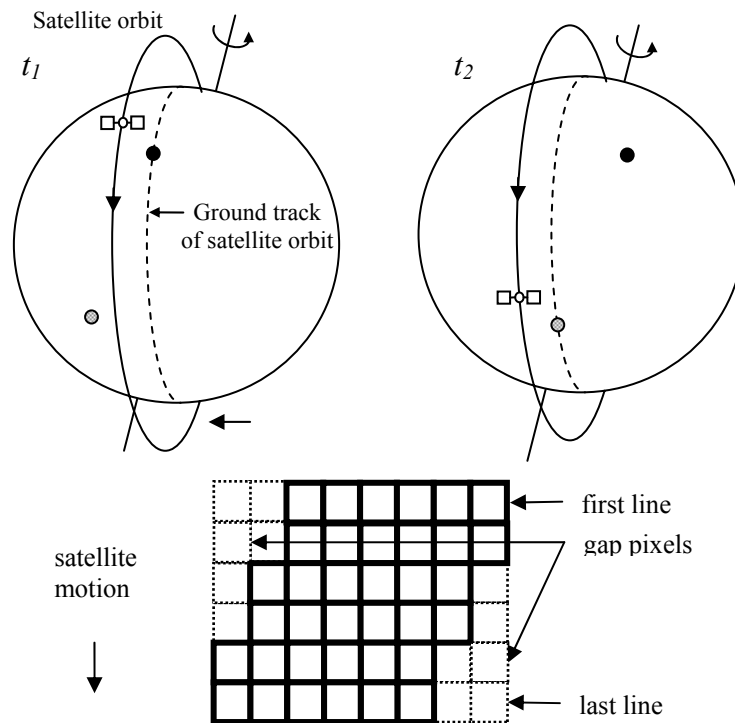


**Figure 2.14:** Rotation of Earth during nadir acquisition (above) and corresponding corrected image (below).

### 2.3.7 Influence of topographic relief

Since the Earth surface is not flat, the topographic relief causes shift of pixel position (Figure 2.15). This influence is seen in  $y$ -direction of an across-track image, in  $x$ -direction of an along-track image and in both  $x$ - and  $y$ -directions of a flexible image.

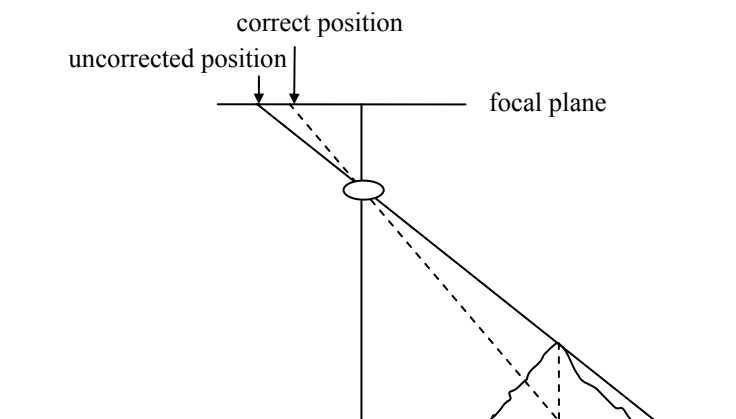


**Figure 2.15:** Influence of topographic relief.

Brief information with respect to geometric correction of these distortions and influences are summarized in the following section.

### **3. GEOMETRIC CORRECTION OF LINEAR ARRAY HRSIs USING PARAMETRIC MODELS**

#### **3.1 Overview of Geometric Correction of Linear Array HRSIs**

The aforementioned distortions and influences related to imaging sensor, platform, Earth curvature, Earth rotation and topographic relief are corrected by the suitable functions during pre- or post-launch calibration. The pre-launch calibration is generally performed in laboratory environment for the correction of following distortions:

- Change of pixel dimension,
- Shift or rotation of segments in focal plane,
- Line bending,
- Lens distortions.

The following distortions are corrected by various correction methods explained together in the post-launch calibration:

- Shift and rotation of three segments, can be determined and corrected by the images with different inclination angles of the same area, in addition to the pre-launch calibration. Since IRS-1C panchromatic camera has three overlapped segments, the study by Jacobsen (1999) is performed to shift images of each overlapped segments using tie points. The maximum shift values are 7 pixels in  $x$ - and 30 pixels in  $y$ -direction.
- Change of focal length and vertical rotation of segments in focal plane can be determined thanks to ground control points (GCPs) located in different heights.
- Variations of sensor geometry can be determined by the orbital parameters of platform and GCPs.
- Differences of ground pixel size are corrected by the inclination angle of

sensor.

- Influence of Earth curvature is corrected by the information of sensor's inclination angle and position of platform.
- Influence of Earth rotation is removed by the information of platform-position and period of acquisition time. This effect can be removed by a control system during the acquisition time, such as in SPOT-5 satellite.
- Influence of topographic relief is corrected by imaging geometry, sensor orientation, orbital parameters of platform, GCPs and DEM.

Some of these distortions are corrected with the pre- or post-launch calibration parameters by the firms before distribution of the images. However, GCPs and DEM are required as additional data for the correction of some distortions and influences such as sensor geometry and topographic relief. The end-user has to correct the images using this additional data by the various mathematical models.

The mathematical models used for this purpose can be classified as parametric and non-parametric. The non-parametric models do not reflect the real geometry of HRSIs while parametric models consider imaging geometry and position and attitude parameters of satellite etc. Since this thesis is focused on the parametric models, the non-parametric models are not summarized. However, the principles and potential of these models such as polynomial transformation, affine projection, direct linear transformation (DLT), self-DLT, sensor and terrain dependent Rational Function Model (RFM) etc. are investigated by the researchers such as Zoj (1997), Wang (1999), Toutin (2003a), Topan (2004), Jacobsen *et al.* (2005), and Topan and Kutoglu (2009).

## **3.2 Parametric Models**

The parametric models usually depend on the colinearity equations explained in the following section.

### **3.2.1 Colinearity equations**

The geometric relationship between 2 dimensional (2D) image- and 3 dimensional (3D) object-coordinate systems, independently the optical imaging sensor type, can be established by colinearity equations:



$$\begin{aligned}
x &= x_0 - c \frac{R_{11} \cdot (X - X_0) + R_{12} \cdot (Y - Y_0) + R_{13} \cdot (Z - Z_0)}{R_{31} \cdot (X - X_0) + R_{32} \cdot (Y - Y_0) + R_{33} \cdot (Z - Z_0)} \\
y &= y_0 - c \frac{R_{21} \cdot (X - X_0) + R_{22} \cdot (Y - Y_0) + R_{23} \cdot (Z - Z_0)}{R_{31} \cdot (X - X_0) + R_{32} \cdot (Y - Y_0) + R_{33} \cdot (Z - Z_0)}
\end{aligned} \tag{3.1}$$

where  $x$  and  $y$  are image coordinates of GCP,  $x_0$  and  $y_0$  are image coordinates of principal point,  $X$ ,  $Y$  and  $Z$  are object coordinates of GCP,  $X_0$ ,  $Y_0$ , and  $Z_0$  are object coordinates of perspective centre,  $R$  is rotation matrix, and  $c$  is focal length (Kraus, 1993).  $x_0$ ,  $y_0$  and  $c$  are elements of interior orientation where  $X_0$ ,  $Y_0$ ,  $Z_0$  and elements of  $R$  compose exterior orientation.

This equation allows establishing real geometric relationship between 2D image space and 3D object space whereas other models such as affine projection, DLT etc. do not. Rearrangement of this equation for estimate 3D object coordinates from 2D image coordinates is available when the object exists in stereo-images. The  $R$  can be formed by rotation angles, i.e.  $\omega$ ,  $\varphi$ ,  $\kappa$  in classic photogrammetry or by the combination of *roll*, *pitch*, *yaw* ( $a_r$ ,  $a_p$  and  $a_y$ ) and Keplerian elements (*inc*,  $\Omega$ ,  $f$  and  $w_p$ ), or unit vectors estimated by position and velocity vectors of the imaging system in satellite photogrammetry.

For the dynamic images, such as acquired by the linear array sensors, the image-coordinate component along the flight direction ( $x$ ) is considered as zero (0) (Weser *et al.*, 2008). This coordinate component associates with the imaging time of the related line of image. Contrary, the exterior orientation parameters (EOPs) are equal for one image in film based or digital frame images and are changed with time for each line of image in the case of linear array imaging. The EOPs in the second case are varied considering the real geometric relationship between image- and object coordinate systems. Figure 3.1 illustrates the relationship between image- and object coordinates in the case of aerial photogrammetry with film-based or digital frame image. In this case only one  $R$  matrix consisting of  $\omega$ ,  $\varphi$  and  $\kappa$  angles and only one set of  $X_0$ ,  $Y_0$ ,  $Z_0$  is enough for all image. However if the satellite or shuttle is used as the platform, many other auxiliary coordinate systems, time dependent rotation and shifts between them have to be considered. This issue will be detailed in the section 3.3.

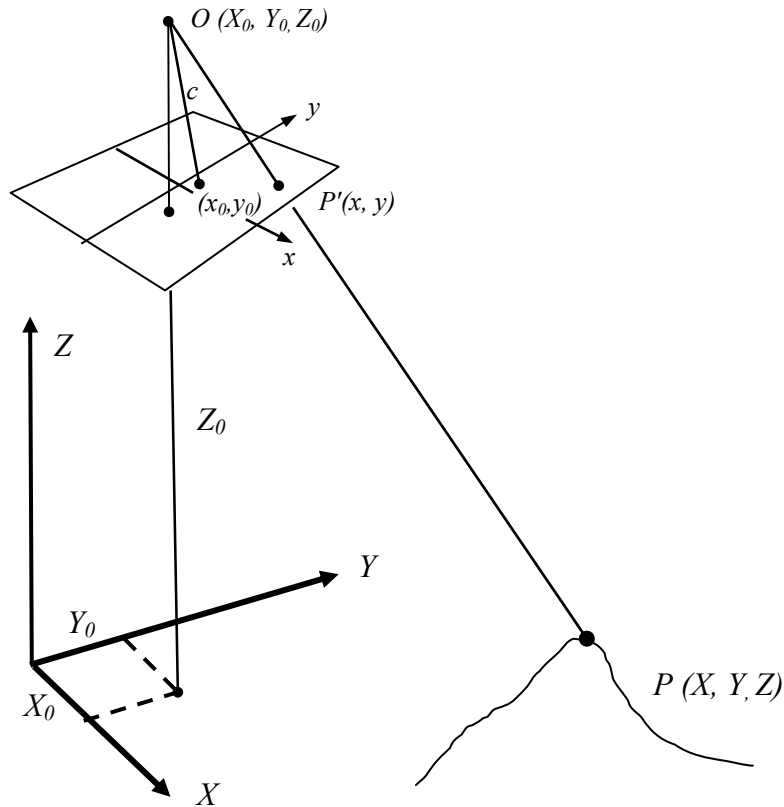


**Figure 3.1:** Relationship between image and ground coordinate systems in aerial photogrammetry with film based or digital frame images.

The image-coordinates ( $x$  and  $y$ ) are mostly considered as observations whereas EOPs are mostly the adjustment parameters in the adjustment procedure. A linearization is required since the collinearity equations are non-linear. The initial values of the unknowns can be estimated by GCPs, or directly measured by Global Navigation Satellite Systems (GNSS), Doppler Orbitography Radiopositioning Integrated by Satellite (DORIS) etc. for positioning and Inertial Measurement Unit (IMU) for determination of rotation angles. The elements of interior orientation can be considered as unknowns if the camera calibration is not confidential, and additional parameters can be applied to overcome systematic errors (Jacobsen, 2008).

### 3.2.2 Existing parametric models

The parametric models developed by the researchers such as Guichard and Toutin in 1993 (Toutin, 2003b), Salamonowicz in 1986 (Salamonowicz, 1986), Gugan in 1987 (Gugan, 1987), Konency *et al.* in 1987 (Konency *et al.*, 1987), Jacobsen in 1988 (Jacobsen, 2005), Kratky in 1989 (Fristsch and Stalman, 2000), Westin in 1990

(Westin, 1990), Orun and Natarajan in 1994 (Orun and Natarajan, 1994), Radhadevi and Ramachandran in 1994 (Zoej, 1997), El-Manadili and Novak in 1996 (El-Manadili and Novak, 1996), Poli in 2005 (Poli, 2005) and Jung *et al.* in 2007 (Jung *et al.*, 2007) are summarized in this section. These models are generated for the motivation of rigorous evaluating the images using their special characteristics with respect to their imaging geometry, sensor orientation and satellite orbital parameters. The following approaches are some of the existing models based on the colinearity equations in photogrammetry, but the investigators take differing parameters into account.

### 3.2.2.1 3D CCRS parametric model by Toutin

The 3 dimensional (3D) Canadian Center for Remote Sensing (CCRS) Parametric Model, developed by Toutin since 1983, benefits from theoretical work in celestial mechanics for better determination of the satellite's osculatory orbit and parameters. The model takes into account the following distortions relative to the global geometry of viewing:

- distortions relative to the platform (position, velocity, orientation),
- the distortions relative to the sensor (orientation angles, IFOV, detection signal integration time),
- the distortions relative to the earth (geoid-ellipsoid, including elevation), and
- the deformations relative to the cartographic projection.

The model integrates the following transformations:

- rotation from the sensor reference to the platform reference,
- translation to the Earth's centre,
- rotation which takes into account the platform time variation,
- rotation to align the  $z$ -axis with the image centre ( $M_0$ ) on the ellipsoid,
- translation to the image centre ( $M_0$ ),
- rotation to align the  $y$ -axis in the meridian plane,
- rotation to have  $x M_0 y$  tangent to the ellipsoid,
- rotation to align the  $x$ -axis in the image scan direction, and

- rotation-translation into the cartographic projection.

The final equation which link cartographic coordinates to the image coordinates is given as:

$$Pp + y(1 + \delta\gamma X) - \tau H - H_0 \Delta T^* = 0 \quad (3.2)$$

$$X + \theta H / \cos \chi + \alpha q(Q + \theta X - H / \cos \chi) - Q \Delta R = 0 \quad (3.3)$$

where

$$X = (x - ay)(1 + h / N_0) + by^2 + cxy \quad (3.4)$$

$$H = h - X^2 / 2N_0 \quad (3.5)$$

and  $H$  is the altitude of the point corrected for Earth curvature,  $H_0$  is the satellite elevation at the image centre line,  $N_0$  is the normal to the ellipsoid,  $A$  is mainly a function of the rotation of the Earth,  $\alpha$  is the instantaneous field-of-view,  $p$  and  $q$  are the image coordinates,  $P$  and  $Q$  are the scale factors in  $Y$  and  $X$ , respectively,  $\tau$  and  $\theta$  are function of the leveling angles in  $Y$  and  $X$ , respectively,  $\Delta T^*$  and  $\Delta R$  are the non-linear variations in attitude if they exist ( $\Delta T^*$ : combination of pitch and yaw,  $\Delta R$ : roll),  $x$ ,  $y$  and  $h$  are the ground coordinates,  $b$ ,  $c$ ,  $\kappa$  and  $\delta\gamma$  are 2<sup>nd</sup>-order parameters, which are a function of the total geometry, e.g., satellite, image and Earth.

In the equations above,  $p$ ,  $q$  are the observations,  $x$ ,  $y$ ,  $h$  are the known parameters.  $b$ ,  $c$ ,  $\kappa$ ,  $\delta\gamma$ ,  $N_0$ ,  $H_0$  are determined from latitude of the scene centre and the orbital oscillatory parameters. Therefore the basis of this approach amounts to the determination by least squares solution of the five unknowns  $P$ ,  $Q$ ,  $\tau$ ,  $\theta$  and  $a$  using collinearity equations, and three unknowns of translation and rotation between the local terrain system and the cartographic system. Thus, eight parameters have to be determined (Zoej, 1997).

Each parameter above represents the physical realities of the full viewing geometry (satellite, sensor, Earth, map projection) and each of these parameters is the combination of several correlated variables of the viewing geometry. The combination of several variables is:

- the orientation of the image is a combination of the platform heading due to orbital inclination, the yaw of the platform, the convergence of the meridian,
- the scale factor in along-track direction is a combination of the velocity, the altitude and the pitch of the platform, the detection signal time of the sensor, the component of the Earth rotation in the along-track direction,
- the levelling angle in the across-track direction is a combination of platform roll, the incidence angle, the orientation of the sensor, the Earth curvature etc.

This model applies to visible and infrared (VIR) images (Landsat 5 and 7, SPOT, IRS, ASTER and KOMPSAT), as well as radar images (ERS, JERS, SIR-C and RADARSAT) with three to six GCPs. This model applied to different image types is robust and not sensitive to GCP distribution, as long as there is no extrapolation in planimetry and elevation (Toutin 2003b).

### 3.2.2.2 Model by Salamonowicz

The model developed by Salamonowicz (1986) is not related to linear array HRSIs. However, this model is referenced for the improving of further parametric models. This model aims to reduce the number of required GCPs using the satellite orientation and position parameters. The steps of processing are:

- The sample positions are corrected for the errors in exist because of periodic variations in the scan rate. The corrected sample ( $SN_{corr}$ ) is calculated.
- The directions angles  $\psi$  and  $\theta$ , in the along- and across-track directions respectively, are computed from line numbers (LN) and sample numbers ( $SN_{corr}$ ).
- The component of a rectangular image coordinate  $x_p$ ,  $y_p$  and  $z_p$  are computed by  $\psi$  and  $\theta$ .
- The effect caused by the Earth rotation is removed in the longitude of GCPs.
- The position vector of the satellite (s) is computed.
- The tangential velocity ( $v_s$ ) is computed.
- The instantaneous satellite geocentric latitude ( $\Phi_s$ ), longitude ( $\lambda_s$ ) and azimuth ( $Az_s$ ) are computed.

- The rotation matrix (R) is computed by  $\Phi_s, \lambda_s$  and  $Az_s$ .
- The roll ( $\omega_s$ ), pitch ( $\varphi_s$ ) and yaw ( $\kappa_s$ ) for the  $i^{th}$  point is computed by satellite's roll ( $\omega_o$ ), pitch ( $\varphi_o$ ) and yaw ( $\kappa_o$ ) values and their rates ( $\dot{\omega}, \dot{\varphi}$  and  $\dot{\kappa}$  respectively) considering time delay ( $t_i-t_1$ ).
- A rotation matrix (M) is computed as a function of  $\omega_s, \varphi_s$  and  $\kappa_s$ .
- The relation between position of GCP and of satellite is determined using R and M.
- The equations  $F_x$  and  $F_y$  are defined.
- The corrections to the estimated parameters are computed.

### 3.2.2.3 Model by Gagan

Gagan's model is an approach developed for the orientation of SPOT images using its dynamic orbital parameters (Gagan, 1987). This model is similar to the model developed by Salamonowicz in 1986 (Zoej, 1997). The model is established between an earth centered coordinate system (e.g. geocentric coordinate system) and image coordinate systems to avoid distortions caused by earth curvature and map projection characteristics.

In the model, the inner orientation is different and simpler than in an aerial photogrammetry. The marks are selected as corner pixels of the image. However, in the case of exterior orientation, the elements of exterior orientation are changing during this period since a SPOT panchromatic image is recorded 9 sec. So the image geometry becomes a dynamic and has a cylindrical perspective. This condition does not allow determining six elements of exterior orientation ( $X_0, Y_0, Z_0, \omega, \varphi, \kappa$ ) and small changes on  $x$  and  $y$  parallax becomes:

$$dX_0 : px = dx \quad py = 0 \quad (3.6)$$

$$d\phi : px = -zd\phi \quad py = 0 \quad (3.7)$$

These two elements cannot be distinguished.

The satellite is moving along a well defined orbit and the EOPs of image can be modelled by consideration of the Keplerian orbital parameters. Of six Keplerian parameters, the semi-minor axis of orbital ellipse ( $b$ ), and the argument of perigee

$(\omega)$  has very little effect on the image geometry considering very low orbit eccentricity ( $e$ ).

The true anomaly ( $F$ ) and the ascending node ( $\Omega$ ) are modelled by linear angular changes with time because these two parameters are affected by two major components of dynamic motion, i.e. the movement of the satellite along the orbit path and the Earth's rotation:

$$F = F_0 + F_1x \quad (3.8)$$

$$\Omega = \Omega_0 + \Omega_1x \quad (3.9)$$

The sensor's position ( $X_s$ ) can be found as following:

$$X_s = R_0 \cdot D \quad (3.10)$$

$$R_0 = R_{\Omega'} R_{i'} R_{F'} \quad (3.11)$$

$$\Omega' = 180^\circ - \Omega \quad (3.12)$$

$$i' = i - 90^\circ \quad (3.13)$$

$$F' = 90^\circ - (F + \omega) \quad (3.14)$$

$$D = (0, 0, r)^T \quad (3.15)$$

$$r = a(1 - e^2)/(1 + e \cos F) \quad (3.16)$$

where  $R_0$  is rotation between sensor and geocentric coordinate systems,  $i$  is orbit inclination, and  $a$  is orbit semi-major axis.

The collinearity equation for one line becomes:

$$(0, y, -f)^T = sR_0(X_A - X_s) \quad (3.17)$$

where  $s$  is scale,  $f$  is focal length,  $X_A$  is  $X, Y, Z$  coordinates of GCP  $A$ .

The additional attitude rotation defined by  $R_A$  has to be considered due to the orbit perturbations. So the last equation becomes as following:

$$(0, y, -f)^T = sR_A R_0(X_A - X_s) \quad (3.18)$$

This method of image orientation where the attitude variations are described by drift rates can be used for the handling of long image strips and is particularly flexible to be used with two GCPs. This model is applied, by modification considering the

view-angle, to SPOT level 1A and 1B, MOMS-02, IRS-1C and IKONOS (Zoej, 1997; Zoej and Petrie, 1998; Zoej and Fooami, 1999; Zoej and Sadeghian, 2003) and also to SPOT-5 HRS the along-track pushbroom images as a general sensor model (Dowman and Michalis, 2003; Michalis, 2005).

#### 3.2.2.4 Model by Konecny et al.

Konecny *et al.* (1987) from Institute of Photogrammetry and Geoinformation (IPI), in the Leibniz University Hannover, evaluate the stereo SPOT Level 1A images by a bundle adjustment program BINGO on analytical photogrammetric instrument. A new approach is developed to avoid high correlation among the parameters. The parameters of orientation are estimated by thanks to orbit data and the additional parameters. The exterior orientation of each single CCD line is represented by six parameters as in the case of aerial photography. Nevertheless the parameters are highly correlated.

The flight path from A to E is considered as straight. The projection centre moves linearly from A to E. So the position of projection centre can be calculated as:

$$X_{0,i} = X_{0,A} + \frac{S_i}{S_{AE}}(X_{0,E} - X_{0,A}) \quad (3.19)$$

$$\frac{i}{n} = \frac{S_i}{S_{AE}} \quad (3.20)$$

where  $X_{0,i}$  is position-vector of the projection centre at time  $i$ ,  $X_{0,A}$  is position-vector of the first line,  $X_{0,E}$  is position-vector of the last line,  $S_i$  is distance from  $X_{0,A}$  to  $X_{0,i}$ ,  $S_{AE}$  is distance from  $X_{0,A}$  to  $X_{0,E}$ .

The orientation angles ( $\omega$ ,  $\varphi$  and  $\kappa$ ) are regarded as constant. A position-vector of discrete point on a line in the image is:

$$X - X_0 = \lambda R x' \quad (3.21)$$

$$x' = (0, y', -f) \quad (3.22)$$

where  $X$  is position-vector of a discrete point,  $X_0$  is position-vector of projection centre,  $\lambda$  is scale factor,  $R$  is rotation matrix.



Here,  $y'$  corresponds to the pixel number  $j$  and is related to the centre of the line. In reality, the orientation angles ( $\omega$ ,  $\varphi$  and  $\kappa$ ) are not constant and all six orientation parameters are functions of time. Of all EOPs,  $\varphi$  with  $X_0$  and  $\omega$  with  $Y_0$  are highly correlated assuming the flight in  $X$ -direction. However the change of  $\varphi$  or  $X_0$  is insignificant in term of ground coordinates.

The angular changes are a function of time  $i$  and these are expressed as 8 sets of additional parameters. The parameters are coordinates of the centre point  $M$  and the orientation angles ( $\omega$ ,  $\varphi$  and  $\kappa$ ) and additional parameters. The Earth rotation is considered in the model and  $t_{AE}$  is defined as real track heading. In order to stabilize the block, a weight is assigned to the parameters  $\omega$ ,  $\varphi$  and  $\kappa$ . The  $t_{AE}$ ,  $S_{AE}$  and  $H_{AE}$  (height difference between A and E) are used for the interpolation of centers of projection between A and E. The GCPs and independent check points (ICPs) are included in the adjustment, even.

In the restitution process the header file of SPOT image is used by CSPOT to compute approximate orientations and sensor specific parameters. In the model, the differences between central perspective and SPOT geometry have to be considered. The modified BINGO results in the following:

- 6 parameters of exterior orientation, i.e.  $X_M$ ,  $\omega$ ,  $\varphi$  and  $\kappa$ ,
- the values and correlations of additional parameters,
- 3D coordinates of object points,
- variances and covariances of the parameters,
- the variance components of the observations.

### 3.2.2.5 BLASPO and CORIKON by Jacobsen

Both programs for the scene orientation by geometric reconstruction BLASPO and CORIKON developed by Jacobsen since 1988, in the IPI of Leibniz University Hannover, are for the handling of satellite linear array images. BLASPO is a program for handling original images linear array images, while CORIKON handles images projected to a plane with constant height. The principle of BLASPO is to reconstruct the image geometry based on the given view-direction, the general orbit information (inclination, eccentricity and semi-major axis) and few GCPs (BLASPO, 2004; Jacobsen, 1998). Because of the high correlation between traditional EOPs, only  $Z_0$  and  $\omega$ ,  $\varphi$  and  $\kappa$  are used as unknowns. Two additional parameters are required for

image- and angular-affinity, and more additional parameters can be used if the geometric problems of image exist. The attitude and the satellite height are improved using GCPs (Jacobsen et al., 2005).

CORIKON is the other program to evaluate the images projected to a plane with constant height such as SPOT-5 level 1B, IRS-1C level 1B, IKONOS Geo, QuickBird Standard and OrthoReady image products. The principle of CORIKON is the computation of the satellite-position using the information of “nominal collection elevation” and “nominal collection azimuth” or the “satellite elevation” and “satellite azimuth”. Together with the general orbit information the individual satellite position corresponding to any ground point can be reconstructed (CORIKON, 2003). With ground control points a bias correction is possible after a terrain relief correction. This can be done by 2D-affinity transformation (6 parameters) or just a simple shift (2 parameters). For the case of poor or not available imaging information also the view direction (2 parameters) can be adjusted (Büyüksalih et al., 2004).

### 3.2.2.6 Model by Kratky

Kratky developed a model to geometric process of SPOT images considering its dynamic characteristics (Kratky, 1987 and 1989). The transformation between image and ground coordinates is dependent on time and given as:

$$\begin{bmatrix} X \\ Y \\ Z \end{bmatrix} = \begin{bmatrix} X_c \\ Y_c \\ Z_c \end{bmatrix} + rF_M(\kappa, \varphi, \omega) \begin{bmatrix} x' \\ y' \\ -f \end{bmatrix} \quad (3.23)$$

where  $X, Y, Z$  are ground coordinates,  $X_c, Y_c, Z_c$  is ground coordinates of projection centre,  $r$  is scale,  $F_M(\kappa, \varphi, \omega)$  is rotation matrix,  $x'$  and  $y'$  are image coordinates ( $y' = 0$ ), and  $f$  is focal length.

The projection centre is computed as a functions of  $y'$ , position of the centre of image ( $X_0, Y_0, Z_0$ ) and linear ( $\dot{X}, \dot{Y}, \dot{Z}$ ) and quadratic ( $\ddot{X}, \ddot{Y}, \ddot{Z}$ ) rates of change, respectively, i.e. the coordinates of projection centre is:

$$\begin{bmatrix} X_c \\ Y_c \\ Z_c \end{bmatrix} = \begin{bmatrix} X_0 + y' \dot{X} + y'^2 \ddot{X} + \dots \\ Y_0 + y' \dot{Y} + y'^2 \ddot{Y} + \dots \\ Z_0 + y' \dot{Z} + y'^2 \ddot{Z} + \dots \end{bmatrix} \quad (3.24)$$

The unknowns are:

- the position of centre of image  $(X_0, Y_0, Z_0)$  and reference attitude elements  $(\kappa, \varphi, \omega)_0$ ,
- the linear  $(\dot{X}, \dot{Y}, \dot{Z})$  and quadratic  $(\ddot{X}, \ddot{Y}, \ddot{Z})$  rates of change, and
- the change of image scale in the direction of scanline.

This model is applied for the orientation of SPOT (Baltsavias and Stallmann, 1992), MOMS-02/D2 (Baltsavias and Stallmann, 2000) and MOMS-02/Priroda (Poli et al., 2000). The model is also investigated and extended for SPOT images by Fritsch and Stallmann (2000).

### 3.2.2.7 Model by Westin

The model developed by Westin is applied on the SPOT and EROS-A1 images (Westin, 1990; Westin and Forsgren, 2001). This model is simplified assuming satellite's orbit circular during the timespan of one scene. Thus four Keplerian elements ( $i$  inclination,  $\Omega$  right ascension of the ascending node,  $t_0$  time at the ascending node and  $r_0$  orbital radius at  $t=t_0$ ) are estimated. The radial shape of the orbit is determined by fitting a third-order polynomial in time to the orbital radius derived from the ephemeris. The relative attitude angles can be calculated by integration since the attitude angular velocities are measured on board with sufficient accuracy. The attitude of the satellite is determined by first-order polynomial in time for the rotation angles  $\omega$ ,  $\varphi$  and  $\kappa$  as follows:

$$\begin{aligned}\omega &= \omega_0 + \Delta\omega(t) \\ \varphi &= \varphi_0 + \Delta\varphi(t) \\ \kappa &= \kappa_0 + \Delta\kappa(t)\end{aligned}\tag{3.25}$$

In totally, seven parameters ( $i$ ,  $\Omega$ ,  $t_0$ ,  $r_0$ ,  $\omega_0$ ,  $\varphi_0$  and  $\kappa_0$ ) have to be adjusted in this approach.

The author defines seven coordinate systems as follows:

- The Earth centered inertial coordinate system (ECI),
- The local orbital reference system,
- The attitude measurement reference system,
- The sensor coordinate system,

- The SPOT coordinate system,
- The SPOT ephemeris reference system, and
- The ground control point reference system.

The relation between image and ground coordinate system is established as:

$$\begin{bmatrix} 0 \\ y \\ -f \end{bmatrix} = \frac{1}{d} R_{IF}^T R_{FB}^T R_{BS}^T \begin{bmatrix} X - X_p \\ Y - Y_p \\ Z - Z_p \end{bmatrix} \quad (3.26)$$

where  $d$  is scaling factor,  $X_p, Y_p, Z_p$  are coordinates of satellite position,  $R_{IF}$  is flight-inertial transformation relating the orbital reference system to the ECI systems,  $R_{FB}$  is body-flight transformation relating the attitude reference system to the orbital reference system,  $R_{BS}$  is sensor-body transformation relating the sensor coordinate system to the attitude reference system,  $f$  is focal length.

The most important difference from the ordinary collinearity equations in aerial photogrammetry is that the sensor  $x$ -coordinate is always zero, and that parameters of right side apart from  $d$  in Equation (3.26) are functions of time (Westin, 1990).

### 3.2.2.8 Trade-off by Orun and Natarajan

The model named Orun & Natarajan Satellite Sensor Model is developed by Orun and Natarajan (1994) for evaluation of SPOT images. This model is applied to SPOT (Kim and Kang, 2001) and KOMPSAT-1 EOC images (Kim and Im, 2001).

The small changes ( $d\omega_s$ ) in  $\omega_s$  is not distinguished from a small change ( $dY_s$ ) in  $Y_s$ . Similarly, small changes ( $d\varphi_0$ ) in  $\varphi_s$  and ( $dx_0$ ) in  $x_s$ , can not be differentiated. Then, replacing  $x_i$  in place of  $t$  in the model, the EOPs are formulated as follows:

$$\begin{aligned} X_s &= X_0 + a_1 x_i + b_1 x_i^2 \\ Y_s &= Y_0 + a_2 x_i + b_2 x_i^2 \\ Z_s &= Z_0 + a_3 x_i + b_3 x_i^2 \\ \kappa_s &= \kappa_0 + a_4 x_i + b_4 x_i^2 \end{aligned} \quad (3.27)$$

where  $X_s, Y_s, Z_s$  are coordinates of satellite position,  $X_0, Y_0, Z_0$  are coordinates of central linear array,  $a_i, b_i$  = coefficients ( $i: 1(1)4$ ),  $\kappa_s$  is yaw angle of satellite position,  $\kappa_0$  is yaw angle of central linear array.

The rotation matrix  $R$  is given as follows:

$$R = \begin{bmatrix} \cos(\kappa_0 + a_4x_i + b_4x_i^2) & \cos\omega\sin(\kappa_0 + a_4x_i + b_4x_i^2) & \sin\omega\sin(\kappa_0 + a_4x_i + b_4x_i^2) \\ -\sin(\kappa_0 + a_4x_i + b_4x_i^2) & \cos\omega\cos(\kappa_0 + a_4x_i + b_4x_i^2) & \sin\omega\cos(\kappa_0 + a_4x_i + b_4x_i^2) \\ 0 & -\sin\omega & \cos\omega \end{bmatrix} \quad (3.28)$$

where  $w$  is the tilt angle of image.

Some non-negligible points of model are found:

- A pseudo code for the iterative determination of  $x$  image coordinate which is set to zero on the left hand side of collinearity equation is established.
- Partial pivoting is invoked during the least-squares solution of the normal equations by Gaussian elimination.
- Highly correlated parameters  $a_3$  and  $b_3$  are eliminated.
- In order to check for consistency with the photogrammetric solutions, eight parameters ( $a_1, \dots, a_4; b_1, \dots, b_4$ ) are set to zero on certain runs.

### 3.2.2.9 Model by Radhadevi and Ramachandran

In 1994, Radhadevi and Ramachandran developed a parametric model based on the collinearity equations (Zoej, 1997). The relationship between sensor and ground coordinate system is established as:

$$\begin{bmatrix} 0 \\ g_s \\ -f \end{bmatrix} = \lambda M \begin{bmatrix} X - X_p \\ Y - Y_p \\ Z - Z_p \end{bmatrix} \quad (3.29)$$

$$M = R_{GF} R_{FB} R_{BS} \quad (3.30)$$

$R_{GF}$  is flight-geocentric transformation matrix consisting in three rotations of the osculating parameters  $\Omega$ ,  $i$  and  $v$ . These parameters and  $r$  are functions of time:

$$\begin{aligned} \Omega(t) &= \Omega_0 + \Omega_1 t \\ i(t) &= i_0 + i_1 t \\ v(t) &= v_0 + v_1 t \\ r(t) &= r_0 + r_1 t + r_2 t^2 + r_3 t^3 \end{aligned} \quad (3.31)$$

$R_{FB}$  is body-flight transformation matrix which is a function of roll, pitch and yaw angles. These angles define the angular relationship between the ideal and actual platform coordinates, being a function of time as follows:

$$\begin{aligned}
\omega(t) &= \omega_0 + \omega_1 t + \omega_2 t^2 + \omega_3 t^3 \\
\phi(t) &= \phi_0 + \phi_1 t + \phi_2 t^2 + \phi_3 t^3 \\
\kappa(t) &= \kappa_0 + \kappa_1 t + \kappa_2 t^2 + \kappa_3 t^3
\end{aligned}
\tag{3.32}$$

$R_{BS}$  is sensor-body transformation matrix. This matrix is a function of angles of rotation which define the angular relationship between the PAN and actual platform coordinate system derived from the looking angles of the detector. These angles are treated as fixed parameters in the model.  $R_{BS}$  includes the interior orientation parameters such as looking angle, alignment offset etc. which are treated as constants. A co-factor matrix for observations and a weight matrix for parameter estimates into the system are applied.

### 3.2.2.10 Model by El-Manadili and Novak

El-Manadili and Novak (1996) developed a model derived from DLT. DLT is a modified model by Abdel-Aziz and Karara (1971) based on collinearity equations. In the model, the systematic distortions caused by Earth rotations and GSD variations due to off-nadir viewing are corrected. In order to remove the effects of satellite deviations from nominal positions, perturbations in satellite velocity vectors and rate of changes of the sensor attitude angles. The corrections to the image coordinates are as follows:

$$\begin{aligned}
\delta_x &= c_1 + c_2 x_i + c_3 \Delta T \\
\delta_y &= c_4 + c_5 y_i + c_6 \Delta T
\end{aligned}
\tag{3.33}$$

where  $c_j$  is constant values ( $j=1, 2, \dots, 6$ ),  $x_i, y_i$  are the metric image coordinates with respect to the scan-line coordinate system,  $\Delta T$  is time with respect to the frame centre.

The geometric corrections are applied to the image coordinates ( $u, v$ ) for systematic errors caused by the rotation of the Earth and off-nadir viewing. In the case of Earth rotation, the effects are due to the orbit inclination ( $i$ ), incidence angle of the scene ( $I$ ) and latitude of the frame centre ( $\Phi$ ); and in the case of off-nadir viewing, the source of error is incidence angle of the scene.

### 3.2.2.11 Model by Poli

Poli developed a model as flexible as possible and adaptable to a wide class of linear array sensors (Poli, 2005). The model for the purpose of indirect georeferencing estimates the parameters which model the internal and external orientation in a

bundle adjustment with least squares methods, considering the satellite's orbit and the integrations of observations on the external orientation, provided by instruments carried on board, while the internal orientation modelling takes into account the lens distortions and the CCD lines displacement in the focal plane. Namely, the systematic errors caused by the lens and CCD lines are corrected and the integration of any available Global Positioning System (GPS) and Inertial Navigation System (INS) is included in the model (Poli, 2007).

In the case of multi lens, the relative position  $(j, d_{xj}, d_{yj}, d_{zj})$  and attitude  $(\alpha_j, \beta_j, \gamma_j)$  of each lens with respect to the nadir one are imported into the collinearity equations. Piecewise Polynomial Functions (PPM) is invoked for the modelling of sensor external orientation depending on time. The platform trajectory is divided into the segments, according to the PPM approach, and in the each segments the sensor external orientation is modelled by second-order polynomials depending on  $\bar{t}$  (the time of acquisition of a generic image line). The PPM approach is extended in order to consider the integration and correction of GPS and INS observations. Thus the position and attitude of each image line  $l$  belonging the segment  $i$ , indicated with  $[X_C, Y_C, Z_C, \omega_C, \varphi_C, \kappa_C]_l^i$  are modelled as sum of the measured position and attitude data for that line  $[X_{instr}, Y_{instr}, Z_{instr}, \omega_{instr}, \varphi_{instr}, \kappa_{instr}]_l^i$  plus the second-order polynomial functions depending on  $\bar{t}$ :

$$\begin{aligned}
X_C(\bar{t}) &= X_{instr}^i + X_0^i + X_1^i \bar{t} + X_2^i \bar{t}^2 \\
Y_C(\bar{t}) &= Y_{instr}^i + Y_0^i + Y_1^i \bar{t} + Y_2^i \bar{t}^2 \\
Z_C(\bar{t}) &= Z_{instr}^i + Z_0^i + Z_1^i \bar{t} + Z_2^i \bar{t}^2 \\
\omega_C(\bar{t}) &= \omega_{instr}^i + \omega_0^i + \omega_1^i \bar{t} + \omega_2^i \bar{t}^2 \\
\varphi_C(\bar{t}) &= \varphi_{instr}^i + \varphi_0^i + \varphi_1^i \bar{t} + \varphi_2^i \bar{t}^2 \\
\kappa_C(\bar{t}) &= \kappa_{instr}^i + \kappa_0^i + \kappa_1^i \bar{t} + \kappa_2^i \bar{t}^2
\end{aligned} \tag{3.34}$$

where the constant terms  $[X_0, Y_0, Z_0, \omega_0, \varphi_0, \kappa_0]_l^i$  compensate for the shifts and angular drifts between the image system and the GPS and INS systems, whereas the linear and quadratic terms  $[X_1, Y_1, Z_1, \omega_1, \varphi_1, \kappa_1]_l^i$  and  $[X_2, Y_2, Z_2, \omega_2, \varphi_2, \kappa_2]_l^i$  model the additional systematic errors contained in the GPS and INS measurements. This model is applied for the optical images such as

ASTER VNIR, EROS-A1, MISR, MOMS-2P, SPOT-5 HRS, TLS (Poli, 2002, 2003, 2004, 2005 and 2007).

### 3.2.2.12 LOS vector adjustment model by Jung et al.

The Line-of-Sight (LOS) vector adjustment model is developed by Jung et al. (2007), depending on the core idea that only the LOS vector is adjusted during the geometric correction of SPOT-5 high resolution geometry (HRG) imagery. This model assumes:

- The satellite is moving along well-defined close-to-circular elliptical orbit.
- The predicted orbit recorded in the header file is close to the true satellite orbit.

Using all parameters available in the header file, LOS vector adjustment model performs a restitution of satellite imagery using additional corrections terms, which adjusts the LOS vector as a function of image lines and pixels for exterior orientation. Orbital parameters ( $\Omega$ ,  $Inc$ ,  $f+w_p$  and  $r$ ) are estimated using position and velocity vectors ( $\vec{S}$  and  $\vec{V}$ , respectively), with the expressions such as linear function of time for  $\Omega$ ,  $Inc$ , and third order polynomial function of time for  $f+w_p$  and  $r$ .

The relationship between the satellite position in an orbit and its ground position on the Earth is formulated as following:

$$\vec{p} - \vec{s} = \mu \vec{u} \quad (3.35)$$

where  $\vec{p}$  denotes the vector from Earth centre to a point on the Earth's surface,  $\vec{s}$  denotes the vector from Earth centre to the satellite,  $\vec{u}$  is the LOS vector, and  $\mu$  is arbitrary factor. The  $\vec{p}$  and  $\vec{u}$  can be transformed into local orbital coordinate system using the rotation matrices  $M_A$  (the rotation matrix attitude measurement through local orbital coordinate system) and  $M_E$  (the rotation matrix local orbital through Earth-centred inertial coordinate system) as following:

$$M_E^T \begin{bmatrix} p_x \\ p_y \\ p_z \end{bmatrix} - \begin{bmatrix} 0 \\ 0 \\ r \end{bmatrix} = \mu M_A \begin{bmatrix} u_x \\ u_y \\ u_z \end{bmatrix} \quad (3.36)$$

When  $\mu$  is eliminated, the equation becomes:



$$\frac{r_{11}P_x + r_{12}P_y + r_{13}P_z - b_{13}r}{r_{31}P_x + r_{32}P_y + r_{33}P_z - b_{33}r} = \frac{u_x}{u_z} \quad (3.37)$$

$$\frac{r_{21}P_x + r_{22}P_y + r_{23}P_z - b_{23}r}{r_{31}P_x + r_{32}P_y + r_{33}P_z - b_{33}r} = \frac{u_y}{u_z} \quad (3.38)$$

The elements of LOS vector ( $u_x$ ,  $u_y$  and  $u_z$ ) are the functions of the look angles in  $X$  ( $\psi_{ox}$ ) and in  $Y$  ( $\psi_{oy}$ ) in the attitude measurement coordinate system:

$$u_x = \tan(\psi_{ox}) \quad (3.39)$$

$$u_y = \tan(\psi_{oy}) \quad (3.40)$$

$$u_z = -1 \quad (3.41)$$

The residuals  $f_1$  and  $f_2$  can be formulated:

$$f_1 \equiv \tan^{-1} \left[ \frac{r_{11}P_x + r_{12}P_y + r_{13}P_z - b_{13}r}{r_{31}P_x + r_{32}P_y + r_{33}P_z - b_{33}r} \right] + \psi_{ox} = -\psi_{Sx} + \psi_{ox} = 0 \quad (3.42)$$

$$f_2 \equiv \tan^{-1} \left[ \frac{r_{21}P_x + r_{22}P_y + r_{23}P_z - b_{23}r}{r_{31}P_x + r_{32}P_y + r_{33}P_z - b_{33}r} \right] + \psi_{oy} = -\psi_{Sy} + \psi_{oy} = 0 \quad (3.43)$$

where  $\psi_{Sx}$  and  $\psi_{Sy}$  are the look angles defined by the vector between the ground and satellite positions. The  $f_1$  and  $f_2$  have to be zero; however these are not zero because of the uncertainty of orbital parameters. Residuals can be removed by adding error look angles in  $X$  and  $Y$  ( $\psi_{Ex}$  and  $\psi_{Ey}$ ) as follows:

$$f_1(i, j) + \psi_{Ex}(i, j) = -\psi_{Sx}(i) + \psi_{ox}(j) + \psi_{Ex}(i, j) = 0 \quad (3.44)$$

$$f_2(i, j) + \psi_{Ey}(i, j) = -\psi_{Sy}(i) + \psi_{oy}(j) + \psi_{Ey}(i, j) = 0 \quad (3.45)$$

The additional correction term ( $\psi_{Ex}$  and  $\psi_{Ey}$ ) for exterior orientation can be line functions given by:

$$F_1 = kf_1 + k\psi_{Ex} = kf_1 + a_0 + b_0 \cdot i + c_0 \cdot j = 0 \quad (3.46)$$

$$F_2 = kf_{21} + k\psi_{Ey} = kf_{21} + a_1 + b_1 \cdot i + c_1 \cdot j = 0 \quad (3.47)$$

where  $a_0$ ,  $b_0$ ,  $c_0$ ,  $a_1$ ,  $b_1$  and  $c_1$  are the model parameters evaluated by adjusting the LOS vector, and  $k$  is a scaling parameter that is defined by the distance between the ground and the satellite position. The basic model for the LOS vector adjustment model using the method of bias-compensated RFM becomes:

$$\begin{bmatrix} V_1 \\ V_2 \end{bmatrix}_{mn} = \begin{bmatrix} \frac{\partial F_1}{\partial p_x} & \frac{\partial F_1}{\partial p_y} & \frac{\partial F_1}{\partial p_z} & 1 & i & j & 0 & 0 & 0 \\ \frac{\partial F_2}{\partial p_x} & \frac{\partial F_2}{\partial p_y} & \frac{\partial F_2}{\partial p_z} & 0 & 0 & 0 & 1 & i & j \end{bmatrix} \begin{bmatrix} \delta p_{x_n} \\ \delta p_{y_n} \\ \delta p_{z_n} \\ a_{0_m} \\ b_{0_m} \\ c_{0_m} \\ a_{1_m} \\ b_{1_m} \\ c_{1_m} \end{bmatrix} + k_m \begin{bmatrix} f_1 \\ f_2 \end{bmatrix}_{mn} \quad (3.48)$$

where  $V_1$  and  $V_2$  are residuals,  $\delta p_x$ ,  $\delta p_y$  and  $\delta p_z$  are corrections for the approximations for  $\bar{p}$  on a point  $n$  on a single image  $m$ .

In theory this model requires 3 GCPs with triangular distribution. However the suitable results are obtained using 5 GCPs. The model is compared with the bundle adjustment model by ERDAS 8.7 Leica Photogrammetry Suite over a stereopair of SPOT-5, and more rigorous results are reached.

### 3.2.3 Overview of Existing Parametric Models

Many common and discrete points are available among the existing parametric models. However, the common assumptions of the existing parametric models are:

- the image investigated has a dynamic geometry since its each adjacent line is acquired at a different time.
- the EOPs are changing for each adjacent line, and
- the correlation among the parameters is probably available.

Various approaches are generated considering different assumptions. However, the common approach, rather an obligation, is to represent the EOPs by the polynomials. All existing parametric models given in the previous section, except the models by Toutin (1983) and Jacobsen (1988), prefer the polynomial representation. The main motivation here is that if the polynomial representation is not preferred, the EOPs of each line are considered as single parameters. For instance, the total number of parameters for one image becomes 72000 for 12000 lines of an image if the number of EOPs is 6, while their number reduces 18 if a 2nd order polynomial is preferred. The required number of observations is more than 72000 for the first- and more than 18 for the second-case respectively. The required number of GCPs is half of the

number of parameters. The representation of the EOPs by a 2<sup>nd</sup> order polynomial is formulated above.

$$P_{j,i} = P_0 + \dot{P}x_i + \ddot{P}x_i^2 \quad (3.49)$$

where  $P_{j,i}$  is one of six EOPs of the line  $i$  ( $j=1(1)6$ ),  $P_0$  is the EOP for the reference line (generally the centre line of an image),  $\dot{P}$  is drift,  $\ddot{P}$  is drift rates,  $x$  is line position of  $i^{\text{th}}$  GCP. The coefficients  $P_0$ ,  $\dot{P}$  and  $\ddot{P}$  are the new parameters.

No correct or optimal parameter selection is proposed (Kim et al., 2007). Orun and Natarajan (1994) ignore errors in  $\omega$  and  $\varphi$ , and chose the position and  $\kappa$  as the parameters with the 2<sup>nd</sup> order polynomial representation. Konency et al. (1987) ignore all positional parameters and select angular parameters. Salamonowicz (1986) prefers attitude angles with drifts whereas Radhadevi and Ramachandran (1994) take into account the angular parameters as a function of 3<sup>rd</sup> order polynomial. The order of the polynomial can be determined by a significance test for the each parameter.

### 3.3 Model and Adjustment for Geometric Analysis

At the beginning of this section, the model which establishes geometric relation between image and ground coordinate systems will be presented in its generic form. Following, the required modification and will be presented in accordance with the imaging geometry of SPOT-5 HRG sensor.

#### 3.3.1 Generic Model

The generic model in this thesis is based on Weser et al. (2008). This model establishes a well defined relation between image and ground coordinate systems, considering imaging geometry and orbital and attitude parameters of satellite. This model is modified for SPOT-5, ALOS PRISM and QuickBird images by Weser et al. (2008).

##### 3.3.1.1 Coordinate systems and transformations

The relationship between image and ground coordinate systems can be established following the definitions of auxiliary coordinate systems which are defined in Appendix A.2. The required transformations for establishing this relation are illustrated in Figure 3.2 being as following:

- First transformation is from image coordinate system (ICS) to scanline coordinate system (SCS),
- Second transformation is from SCS to camera coordinate system (CCS),
- Third transformation is from CCS to payload coordinate system (PCS),
- Fourth transformation is from PCS to orbital coordinate system (OCS), and
- Fifth, and last, transformation is from OCS to ground coordinate system (GCS).

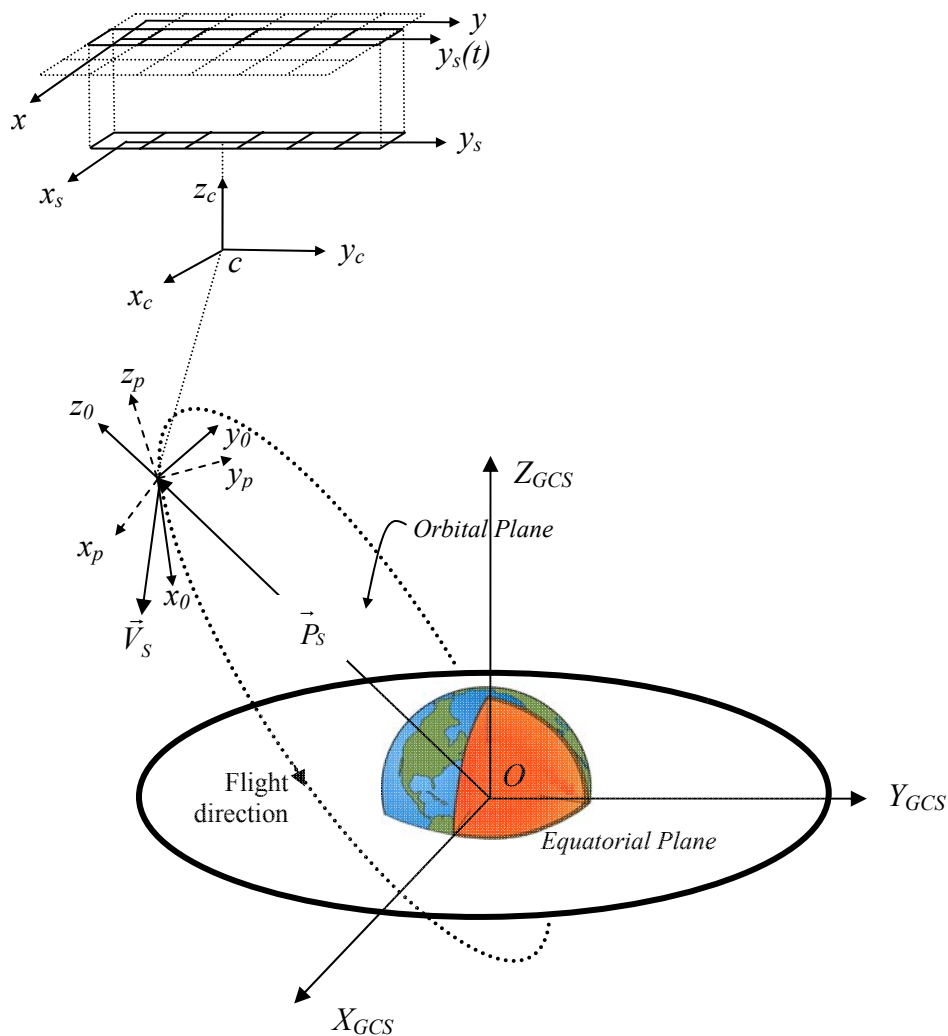


**Figure 3.2:** Transformation from ICS to GCS.

One point on the image is pointed by its image coordinates ( $x_s$  and  $y_s$ ). Since each line of an image is generated by the linear array defining the SCS, the coordinates in SCS ( $x$  and  $y$ ) has to be defined by the transformation from ICS to SCS as following:

$$\vec{p}_s = \begin{bmatrix} x_s \\ y_s \\ 0 \end{bmatrix} = \begin{bmatrix} 0 \\ y \\ 0 \end{bmatrix} \quad (3.50)$$

where  $\vec{p}_s$  is position vector in SCS. The  $x$  coordinate is related to the acquisition time ( $t$ ) in combination with the acquisition time ( $t_0$ ) for reference line (generally the centre line of image), time interval per line ( $\Delta t$ ) and also the  $x$  coordinate of reference line as following:

$$t = t_0 + \Delta t \cdot (x - x_0) \quad (3.51)$$

$t$  is required to estimate time-dependent EOPs changed for each adjacent line of image.

The second transformation, from SCS to CCS, requires taking into account the interior orientation, in other words the position and the rotation of scanline in the camera symbolized by  $\vec{c}_s = [x_s^c \quad y_s^c \quad c]^T$ . The new position vector ( $\vec{p}_c$ ) in CCS becomes:

$$\vec{p}_c = \vec{p}_s - \vec{c}_s + \delta\vec{x} \quad (3.52)$$

where  $\vec{p}_c$  is position vector in CCS,  $\delta\vec{x}$  is vector of systematic error corrections (Weser *et al.*, 2008).

The third transformation from CCS to PCS defines the position and the rotation of camera in the payload (or satellite body) as following:

$$\vec{p}_p = C_M + m \cdot R_{CP} \cdot \vec{p}_c \quad (3.53)$$

where  $\vec{p}_p$  is position vector in PCS,  $C_M$  is the camera mounting parameter, i.e. shift in each three axes,  $m$  is scale factor,  $R_{CP}$  is rotation from CCS to PCS (Weser *et al.*, 2008). Appendix A.3 explains the rotation between two 3D coordinate systems.

The fourth transformation, from PCS to OCS, is the subject of a time-dependent rotation parameterized by the angles ( $a_r, a_p, a_y$ ) as following:

$$\vec{p}_o = R_{PO} \cdot \vec{p}_p \quad (3.54)$$

where  $\vec{p}_o$  is position vector in OCS, and  $R_{PO}$  is rotation from PCS to OCS as explained in Appendix A.3.

Finally, the fifth and last transformation is from OCS to GCS as following:

$$\vec{P} = \begin{bmatrix} X \\ Y \\ Z \end{bmatrix} = \vec{P}_s + R_{OG} \cdot \vec{p}_o \quad (3.55)$$

where  $\vec{P}$  is position vector in GCS,  $\vec{P}_s$  is position vector of satellite,  $R_{OG}$  is rotation from OCS to GCS as a function of  $\vec{P}_s$  and velocity-vector ( $\vec{V}_s$ ) of satellite (Appendix A.3).

The combined equations from (3.50) to (3.55) yield with the required coordinate transformations:

$$\vec{P} = \vec{P}_s + R_{OG} \cdot R_{PO} \cdot [C_M + m \cdot R_{CP} \cdot (\vec{p}_s - \vec{c}_s + \delta\vec{x})] \quad (3.56)$$

Since each adjacent line of image is acquired at a different time, the rotation matrixes  $R_{OG}$  and  $R_{PO}$  are time-dependent. The  $R_{OG}$  is estimated by two ways: the first way is performed using Keplerian angular elements depicted in Appendix A.3 and Greenwich Mean Sidereal Time (GMST), and the second and easier way is performed using  $\vec{P}_s$  and  $\vec{V}_s$ .

### 3.3.1.2 Modelling parameters

The EOPs consist the position ( $\vec{P}_s$ ) and velocity ( $\vec{V}_s$ ) vectors, and attitude angles ( $a_r, a_p, a_y$ ), and can be modelled by the polynomial modelling. For this purpose, these parameters are estimated for each line, and then the polynomial coefficients can be calculated. The Lagrange interpolation is suggested for the estimation of position and velocity vectors of satellite while the linear interpolation is sufficient for the estimation of attitude angles for each line (SPOT Image, 2002). It is required to be given some position sets before and after the estimated position. The Lagrange interpolation can be formulated as following:

$$P(t_i) = \sum_{e=1}^g \frac{P(t_i) \prod_{\substack{d=1 \\ d \neq e}}^g (t_i - t_d)}{\prod_{\substack{d=1 \\ d \neq e}}^g (t_e - t_d)} \quad (3.57)$$

where  $P(t_i)$  is position or velocity of satellite ( $X_S, Y_S, Z_S, V_X, V_Y, V_Z$ ) for line  $i$ ,  $t$  is time,  $d$  and  $e$  are running index, integer,  $g$  is number of given positions or velocities. This interpolation is preferred since the shape of orbit defined by the position and velocity of satellite is not linear.

The attitude angles are linearly interpolated using the time-dependent attitude values as following (SPOT Image, 2002):

$$a_j(t_i) = a_j(t_k) + (a_j(t_{k+1}) - a_j(t_k)) \cdot \frac{t_i - t_k}{t_{k+1} - t_k} \quad (3.58)$$

where  $a_j$  is  $a_r, a_p$  and  $a_y$ , and  $t_k$  is the time given in metadata ( $t_{k-1} < t_i < t_k$ ).

Following the estimation of all parameters for line of each GCP, the EOPs can be represented by 2<sup>nd</sup> order polynomial modelling as following:

$$P_{j,i} = P_0 + \dot{P} \cdot t_i + \ddot{P} \cdot t_i^2 \quad (3.59)$$

where  $P_{j,i}$  is one of the EOPs of the line  $i$  ( $j=1(1)9$ , number of EOP),  $P_0$  is the EOP for the reference line (generally the centre line of image),  $\dot{P}$  is drift,  $\ddot{P}$  is drift rates. So the number of parameters reduces significantly as mentioned in section 3.2.3.

### 3.3.2 Modified Model for SPOT-5

Considering specifications and definitions for SPOT-5 HRG and HRS images, one simplification and two modifications are performed by SPOT Image (2002) comparing the generic model given in Section 3.3.1, as following:

- The look angles ( $\psi_x$  and  $\psi_y$ ) are defined and used in the model to establish interior orientation (Figure 3.3).
- A navigation reference coordinate system (NRCS) is defined corresponding to PCS (Figure 3.3). Then the rotation from NRCS to OCS is different than in the generic model (Appendix A.3).
- The rotation from OCS to GCS is different than defined in the Appendix A.3.

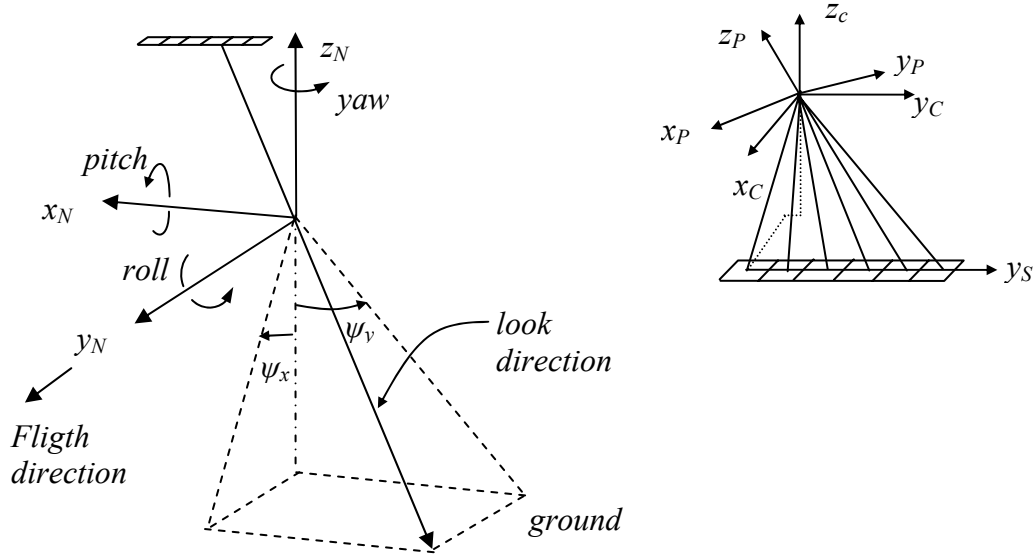


**Figure 3.3:** NRCS and look angles ( $\psi_x$  and  $\psi_y$ ) (left) (SPOT Image, 2002), and bundle rays given by the SPOT-5 look angles (Weser et al., 2008).

The look angles ( $\psi_x$  and  $\psi_y$ ) which define the look direction for each element of the linear array are available in the metadata of SPOT-5 image (Figure 3.3). As the simplification, these look angles are equal to the  $\vec{p}_p$  defining the interior orientation given in equation (3.53) as following:

$$\vec{p}_p = \begin{bmatrix} -\tan(\psi_y) \\ \tan(\psi_x) \\ 1 \end{bmatrix} = C_M + m \cdot R_{CP} \cdot \vec{p}_C = s \cdot R_{CP} \cdot (\vec{p}_S - \vec{c}_S) \quad (3.60)$$

where  $C_M = 0$  (SPOT Image, 2002). Weser *et al.* (2008) try to estimate elements of  $\vec{c}_S$  and  $R_{CP}$  while Fotev *et al.* (2005), Kornus *et al.* (2006) and Jung *et al.* (2007) try to use these look angles directly in the adjustment model.

The first modification on the generic model is suggested for the rotation from PCS (or NCRS) to OCS. SPOT Image suggests to multiply  $a_r$  and  $a_p$  angles by -1, so the rotation becomes:

$$R_{PO} = R_X^{-1}(a_p) \cdot R_Y^{-1}(a_r) \cdot R_Z^{-1}(a_y) \quad (3.61)$$

However the last equation can be simplified as following, since the attitude angles are very small (Fotev et al., 2005):



$$R_{PO} \cong \begin{bmatrix} 1 & -a_y & +a_r \\ +a_y & 1 & -a_p \\ -a_r & +a_p & 1 \end{bmatrix} \quad (3.62)$$

This last equation can be preferred since the linearization for attitude angles is less complex comparing the trigonometric functions included in the equation 3.61.

The second modification is suggested for the rotation from OCS to GCS as following:

$$\begin{bmatrix} R_{3,1}^{OG} \\ R_{3,2}^{OG} \\ R_{3,3}^{OG} \end{bmatrix} = \frac{\vec{P}_s}{\|\vec{P}_s\|} \quad (3.63 \text{ a})$$

$$\begin{bmatrix} R_{1,1}^{OG} \\ R_{1,2}^{OG} \\ R_{1,3}^{OG} \end{bmatrix} = \frac{\vec{V}_s \times \begin{bmatrix} R_{3,1}^{OG} \\ R_{3,2}^{OG} \\ R_{3,3}^{OG} \end{bmatrix}}{\|\vec{V}_s \times \begin{bmatrix} R_{3,1}^{OG} \\ R_{3,2}^{OG} \\ R_{3,3}^{OG} \end{bmatrix}\|} \quad (3.63 \text{ b})$$

$$\begin{bmatrix} R_{2,1}^{OG} \\ R_{2,2}^{OG} \\ R_{2,3}^{OG} \end{bmatrix} = \frac{\begin{bmatrix} R_{3,1}^{OG} \\ R_{3,2}^{OG} \\ R_{3,3}^{OG} \end{bmatrix} \times \begin{bmatrix} R_{1,1}^{OG} \\ R_{1,2}^{OG} \\ R_{1,3}^{OG} \end{bmatrix}}{\|\begin{bmatrix} R_{3,1}^{OG} \\ R_{3,2}^{OG} \\ R_{3,3}^{OG} \end{bmatrix} \times \begin{bmatrix} R_{1,1}^{OG} \\ R_{1,2}^{OG} \\ R_{1,3}^{OG} \end{bmatrix}\|} \quad (3.63 \text{ c})$$

The final equation becomes:

$$\vec{P} = \vec{P}_s + m \cdot \vec{u}_3 \quad (3.64)$$

where

$$\vec{u}_3 = R_{OG} \cdot \vec{u}_2 \quad (3.65)$$

$$\vec{u}_2 = \frac{R_{PO} \cdot \vec{u}_1}{\|R_{PO} \cdot \vec{u}_1\|} \quad (3.66)$$

$$\vec{u}_1 = \frac{\begin{bmatrix} -\tan(\psi_y) \\ \tan(\psi_x) \\ 1 \end{bmatrix}}{\left\| \begin{bmatrix} -\tan(\psi_y) \\ \tan(\psi_x) \\ 1 \end{bmatrix} \right\|} \cong \begin{bmatrix} -\tan(\psi_y) \\ \tan(\psi_x) \\ 1 \end{bmatrix} \quad (3.67)$$

where  $\| \|$  denotes norm of vector.

To apply the equation (3.64) into the adjustment model, this equation can be rewritten as:

$$\vec{u}_1 = \frac{1}{m} R_{PO}^{-1} \cdot R_{OG}^{-1} (\vec{P} - \vec{P}_S) \quad (3.68)$$

$$\begin{bmatrix} -\tan(\psi_y) \\ \tan(\psi_x) \\ 1 \end{bmatrix} = \frac{1}{m} \cdot R \cdot \begin{bmatrix} X - X_S \\ Y - Y_S \\ Z - Z_S \end{bmatrix} = \frac{1}{m} \cdot \begin{bmatrix} r_{11} & r_{12} & r_{13} \\ r_{21} & r_{22} & r_{23} \\ r_{31} & r_{32} & r_{33} \end{bmatrix} \cdot \begin{bmatrix} X - X_S \\ Y - Y_S \\ Z - Z_S \end{bmatrix} \quad (3.69)$$

where  $R = R_{PO}^{-1} \cdot R_{OG}^{-1}$ . Finally, the first and the second lines are divided by the third line to eliminate the scale factor, similarly within equation 3.1, the equation 3.69 becomes:

$$\begin{aligned} F_{\psi_y} &= \frac{r_{11}(X - X_S) + r_{12}(Y - Y_S) + r_{13}(Z - Z_S)}{r_{31}(X - X_S) + r_{32}(Y - Y_S) + r_{33}(Z - Z_S)} + \tan(\psi_y) = \frac{f_1}{f_3} + \tan(\psi_y) = 0 \\ F_{\psi_x} &= \frac{r_{21}(X - X_S) + r_{22}(Y - Y_S) + r_{23}(Z - Z_S)}{r_{31}(X - X_S) + r_{32}(Y - Y_S) + r_{33}(Z - Z_S)} - \tan(\psi_x) = \frac{f_2}{f_3} - \tan(\psi_x) = 0 \end{aligned} \quad (3.70)$$

This last equation suggested by Kornus *et al.* (2006) is the mathematical model used in this thesis.

### 3.3.3 Adjustment

The main aim of adjustment is to estimate both residuals ( $v$ ) of observations ( $L$ ) and unknowns ( $dP$ ) of adjustment parameters ( $P$ ) where observations are consisted by parameters. If the least square adjustment (LSA) is preferred as in this thesis, the condition of  $\underline{v}^T \underline{v} = \min$  must be expected. The observations are look angles of point  $i$  ( $\psi_x$  and  $\psi_y$ ), and the parameters are EOPs and object coordinates of ICPs. These EOPs (position, velocity and attitude angles for line of each GCPs and ICPs) can be represented as following:

$$\begin{aligned}
(X_S)_i &= X_o + \dot{X} \cdot x_i + \ddot{X} \cdot x_i^2 \\
(Y_S)_i &= Y_o + \dot{Y} \cdot t_i + \ddot{Y} \cdot x_i^2 \\
(Z_S)_i &= Z_o + \dot{Z} \cdot t_i + \ddot{Z} \cdot x_i^2 \\
(V_X)_i &= V_{X_o} + \dot{V}_X \cdot x_i + \ddot{V}_X \cdot x_i^2 \\
(V_Y)_i &= V_{Y_o} + \dot{V}_Y \cdot x_i + \ddot{V}_Y \cdot x_i^2 \\
(V_Z)_i &= V_{Z_o} + \dot{V}_Z \cdot x_i + \ddot{V}_Z \cdot x_i^2 \\
(a_r)_i &= a_{r_o} + \dot{a}_r \cdot x_i + \ddot{a}_r \cdot x_i^2 \\
(a_p)_i &= a_{p_o} + \dot{a}_p \cdot x_i + \ddot{a}_p \cdot x_i^2 \\
(a_y)_i &= a_{y_o} + \dot{a}_y \cdot x_i + \ddot{a}_y \cdot x_i^2
\end{aligned} \tag{3.71}$$

Additionally, when the tie or ICPs which their adjusted object coordinates must be determined in the adjustment, their ground coordinates ( $X$ ,  $Y$  and  $Z$ ) are considered as adjustment parameters. The approximate values of their object coordinates can be estimated via stereo images, as depicted in the Appendix A.4. So all parameters in the adjustment are:

$$P = \begin{bmatrix} X_o \dot{X} \ddot{X} Y_o \dot{Y} \ddot{Y} Z_o \dot{Z} \ddot{Z} \dots \\ V_{X_o} \dot{V}_X \ddot{V}_X V_{Y_o} \dot{V}_Y \ddot{V}_Y V_{Z_o} \dot{V}_Z \ddot{V}_Z \dots \\ a_{r_o} \dot{a}_r \ddot{a}_r a_{p_o} \dot{a}_p \ddot{a}_p a_{y_o} \dot{a}_y \ddot{a}_y \dots \\ X Y Z \end{bmatrix}^T \tag{3.72}$$

The major important point in the adjustment is the functional model derived from mathematical model. The functional model in this thesis is Gauss-Helmert model based on the establishing linkage between adjusted observations ( $\bar{L}$ ) and the adjusted parameters ( $\bar{P}$ ). Since the LSA requires the linearized form of condition equation, the linearized Gauss-Helmert model can be established as following:

$$\underline{A} \cdot d\underline{P} + \underline{B} \cdot \underline{v} + \underline{w} = \underline{0} \tag{3.73}$$

where  $A$  and  $B$  denotes design matrix of parameters and observations, respectively, and  $w$  is misclosure vector.  $A$  and  $B$  result from differentiating the non-linear condition equations using the approximate parameters and observations, respectively. The linearization can be done by a proper method, such as Taylor series ignoring second and higher degree terms. So sub-design matrix of point  $i$  ( $\underline{A}_i$ ) after the simplification using look angles ( $\psi_x$  and  $\psi_y$ ) becomes:

$$\underline{A}_i = \begin{bmatrix} \frac{1}{f_3} \frac{\partial f_1}{\partial P_j} - \frac{f_1}{f_3^2} \frac{\partial f_3}{\partial P_j} \\ \frac{1}{f_3} \frac{\partial f_2}{\partial P_j} - \frac{f_2}{f_3^2} \frac{\partial f_3}{\partial P_j} \end{bmatrix}_i = \begin{bmatrix} \frac{1}{f_3} \left( \frac{\partial f_1}{\partial P_j} + \tan(\psi_y) \frac{\partial f_3}{\partial P_j} \right) \\ \frac{1}{f_3} \left( \frac{\partial f_2}{\partial P_j} + \tan(\psi_x) \frac{\partial f_3}{\partial P_j} \right) \end{bmatrix}_i \quad (3.74)$$

Finally the size of  $\underline{A}$  reaches  $2n \times 30$  if all parameters are chosen as adjustment parameters (n is sum of number of GCPs and ICPs).

The  $\underline{dP}$  matrix consists unknown of adjustment parameter as shown in following:

$$\underline{dP} = \begin{bmatrix} dX_o \\ \vdots \\ d\ddot{a}_y \\ dX_{ICP} \\ dY_{ICP} \\ dY_{ICP} \end{bmatrix} \quad (3.75)$$

The size of  $\underline{dP}$  matrix is  $30 \times 1$  when all parameters is chosen as adjustment parameters.

The  $\underline{B}$  matrix related to the observations of point  $i$  becomes:

$$\underline{B}_i = \begin{bmatrix} \frac{1}{\cos(\psi_y)} & 0 \\ 0 & -\frac{1}{\cos(\psi_x)} \end{bmatrix}_i \quad (3.76)$$

The size of  $\underline{B}$  matrix becomes  $2n \times 2n$  when all parameters is chosen as adjustment parameters. And  $w$  for point  $i$  is:

$$\underline{w}_i = \begin{bmatrix} F_{\psi_y} (P|_0, \psi_y|_0) \\ F_{\psi_x} (P|_0, \psi_x|_0) \end{bmatrix}_i \quad (3.77)$$

When all parameters are chosen as adjustment parameters, the equation (3.73) can be rewritten with showing size of matrixes as following:

$$\underline{A}_{2n \times 30} \underline{dP}_{30 \times 1} + \underline{B}_{2n \times 2n} \underline{v}_{2n \times 1} + \underline{w}_{2n \times 1} = \underline{0}_{2n \times 1} \quad (3.73)$$

The unknowns ( $\underline{dP}$ ) can be estimated ignoring the weight of observations as following:

$$\underline{dP} = -(\underline{A}^T (\underline{B}\underline{B}^T)^{-1} \underline{A})^{-1} \underline{A}^T (\underline{B}\underline{B}^T)^{-1} \underline{w} \quad (3.78)$$

So the adjusted parameters become:

$$\bar{\underline{P}} = \underline{P}|_0 + \underline{dP} \quad (3.79)$$

The residuals can be estimated as following:

$$\underline{v} = \underline{B}^T (\underline{B}\underline{B}^T)^{-1} (\underline{A}\bar{\underline{P}} + \underline{w}) \quad (3.80)$$

So the adjusted observations become:

$$\bar{\underline{L}} = \underline{L}|_0 + \underline{v} \quad (3.81)$$

Finally the validation of adjustment can be checked using both adjusted parameters and observations in the mathematical model given by equation (3.70), as following:

$$F(\bar{\underline{L}}, \bar{\underline{P}}) = 0 \quad (3.82)$$

As depicted in the following section, the pre-adjustment of both observations and parameters is required before bundle adjustment of images in this thesis.

### 3.3.3.1 Pre-adjustment

According to Kornus *et al.* (2006), the pre-adjustment before the bundle adjustment is a mandatory process. The major motivation of pre-adjustment is the requirement of correction of look angles. Two types of pre-adjustment are performed in this thesis. In the first type, the look angles are adjusted assuming the EOPs constant for each mono image (i.e.  $\underline{dP} = \underline{0} \rightarrow \underline{A} \cdot \underline{dP} = \underline{0}$ ). So the functional model and the residuals of look angles become:

$$\underline{B} \cdot \underline{v} + \underline{w} = 0 \quad (3.83)$$

$$\underline{v} = -\underline{B}^T (\underline{B} \cdot \underline{B}^T)^{-1} \underline{w} \quad (3.84)$$

The second type of pre-adjustment depends on an additional step following the first type. Namely the adjusted look angles in the first type are assumed constant (i.e.  $\underline{v} = \underline{0} \rightarrow \underline{B} \cdot \underline{v} = \underline{0}$ ), and the parameters are adjusted. The functional model and unknowns become:

$$\underline{A} \cdot \underline{dP} + \underline{w} = \underline{0} \quad (3.85)$$

$$\underline{dP} = -(\underline{A} \cdot \underline{A}^T)^{-1} \underline{A}^T \underline{w} \quad (3.86)$$

The adjusted EOPs and observations can be calculated as in equations (3.79) and (3.81) respectively.

The observations and EOPs of each mono image are estimated separately and also using only GCPs. However estimation of the adjusted look angles of ICPs are required in the bundle adjustment. These look angles are estimated using the adjusted look angles of GCPs. Thus, the coefficients of look angles ( $\psi_{x0}, \dot{\psi}_x, \ddot{\psi}_x, \psi_{y0}, \dot{\psi}_y, \ddot{\psi}_y$ ) are estimated using the equation (3.49), and the look angles of ICPs are calculated using their line number ( $x$ ).

The final adjustment following both types of pre-adjustment is bundle adjustment which is mentioned in the following section.

### 3.3.3.2 Bundle adjustment

The bundle adjustment can be performed if at least two stereo images are available. The advantage of bundle adjustment is that all adjustment parameters and observations of at least both two images are adjusted together as following:

$$\begin{bmatrix} \underline{A}_1 & \cdots & \underline{0} \\ \vdots & \ddots & \vdots \\ \underline{0} & \cdots & \underline{A}_m \end{bmatrix} \cdot \begin{bmatrix} \underline{dP}_1 \\ \vdots \\ \underline{dP}_m \end{bmatrix} + \begin{bmatrix} \underline{B}_1 & \cdots & \underline{0} \\ \vdots & \ddots & \vdots \\ \underline{0} & \cdots & \underline{B}_m \end{bmatrix} \cdot \begin{bmatrix} \underline{v}_1 \\ \vdots \\ \underline{v}_m \end{bmatrix} + \begin{bmatrix} \underline{w}_1 \\ \vdots \\ \underline{w}_m \end{bmatrix} = \underline{0} \quad (3.87)$$

where  $m$  is the number of image.

The adjustment parameters are EOPs for GCPs while the correction of ground coordinates are required assuming the ground coordinates as additional parameters for the new point. This new point can be tie point whose true object coordinates are not known, or ICPs whose true coordinates are known. The approximate coordinate of these points can be intersected from at least two images using approximate parameters and uncorrected observations (see Appendix 4).

The root mean-square error (RMSE) of ground coordinates, as the geometric accuracy of images, can be estimated as following:

$$m_x = \pm \sqrt{\frac{\underline{\Delta X}^T \underline{\Delta X}}{n}} \quad (3.88 \text{ a})$$

$$m_y = \pm \sqrt{\frac{\underline{\Delta Y}^T \underline{\Delta Y}}{n}} \quad (3.88 \text{ b})$$

$$m_z = \pm \sqrt{\frac{\underline{\Delta Z}^T \underline{\Delta Z}}{n}} \quad (3.88 \text{ c})$$

$$\underline{\Delta X} = \bar{X} - \underline{X}_e \quad (3.89 \text{ a})$$

$$\underline{\Delta Y} = \bar{Y} - \underline{Y}_e \quad (3.89 \text{ b})$$

$$\underline{\Delta Z} = \bar{Z} - \underline{Z}_e \quad (3.89 \text{ c})$$

where  $\bar{X}$ ,  $\bar{Y}$  and  $\bar{Z}$  are true ground coordinates, such as observed by GPS and adjusted, and  $\underline{X}_e$ ,  $\underline{Y}_e$ , and  $\underline{Z}_e$  are estimated coordinates by intersection from at least two images and compensated in the adjustment.





## **4. GEOMETRIC ANALYSIS OF SPOT-5 HRG LEVEL 1A STEREO IMAGES**

This section subjects the geometric analysis performed by the suggested modified and simplified mathematical model. At first the test field, images and auxiliary data used in this thesis are mentioned with the description of SPOT-5 satellite and its HRG sensor. Then the workflow of geometric analysis is subjected. Finally the geometric analysis results are presented.

### **4.1 Test Field**

Zonguldak test-field is located in Western Karadeniz Region of Turkey. The position of Zonguldak city centre is about  $31^{\circ} 47' 41''$  East and  $41^{\circ} 27' 25''$  North. This test-field has rolling topography with steep and rugged terrain in some parts. The elevation ranges roughly up to 1800 m. Despite urbanised along the sea coast, some agricultural lands and forest areas exist inland. This area is investigated for different aims in the frame of remote sensing researches, such as georeferencing, geometric analysis, DEM generation and validation, deformation monitoring, information content analysis, change detection, urban growth monitoring, environment, forestry, biology etc. The main importance of this test-field is its mountainous characteristic in our scope. Because the real analysis require optimal distributed GCPs in both horizontal and vertical planes whereas many mathematical models reach very precise results on the flat areas.

### **4.2 Description of Satellite, Image, and Auxiliary Data**

The investigated images are stereo HRG level 1A images of SPOT-5. The SPOT-5 satellite and its brief specifications are summarized before promoting the image and related metadata information.

### 4.2.1 SPOT-5

SPOT-5, the last satellite of SPOT series, was launched on its sun-synchronous, polar and circular orbit with 832 km altitude by CNES (in French: Centre National d'Études Spatiales; French Space Agency) on 4<sup>th</sup> May 2002. SPOT-5 carries HRG, HRS (High Resolution Stereoscopic) and Vegetation-2 imaging sensors, and other sensors and instruments such as star tracker, truster, DORIS antenna, payload telemetry antenna and Digital Earth Sensor, which are required for the operation of the satellite, illustrated in Figure 4.1.

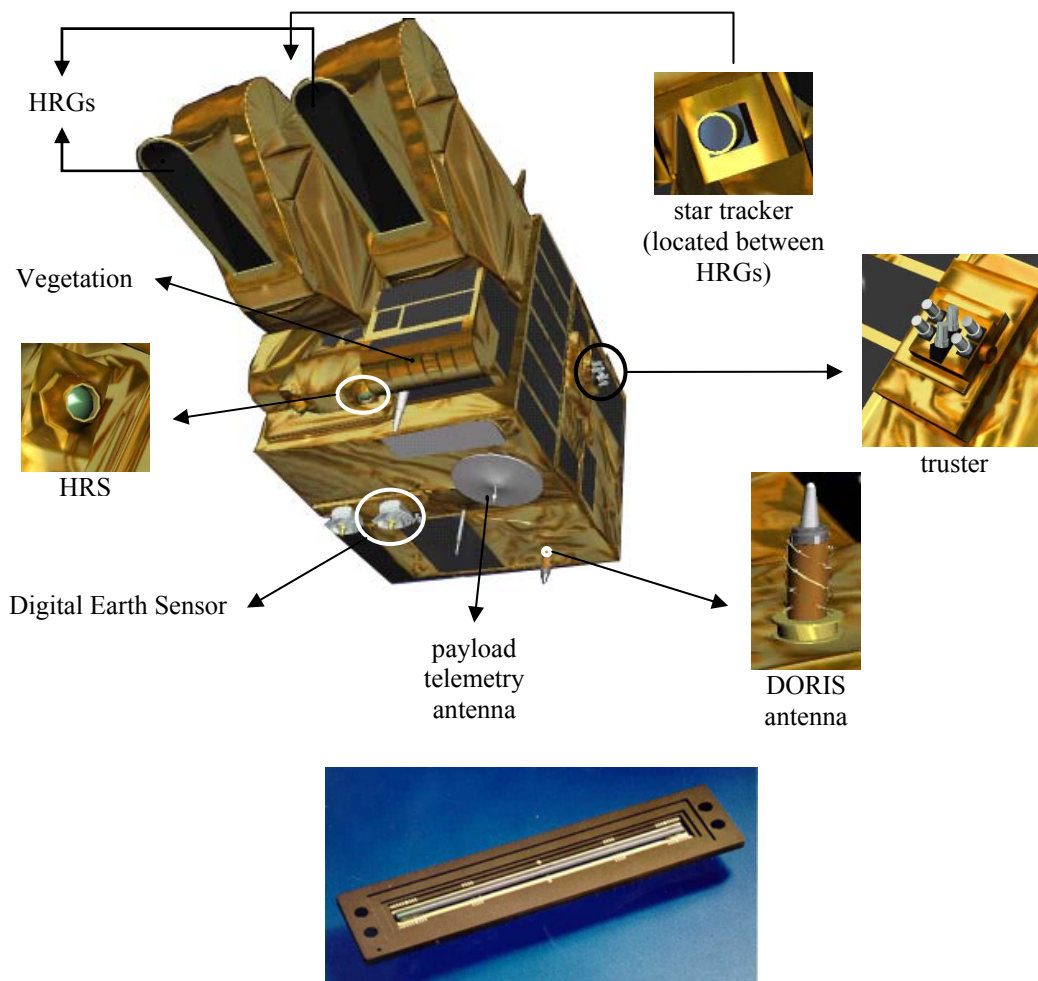


**Figure 4.1:** Imaging sensors and some instruments of SPOT-5 satellite (above) and the CCD array of panchromatic band (below) (SPOT Image, 2002).

Two identical HRG cameras are linear push-broom systems to ensuring multispectral images at four resolution levels, namely the SWIR (short wave infrared) band is at a resolution of 20 m, multispectral mode called HX corresponding to three spectral bands B1 (green), B2 (red) and B3 (near infrared) is at 10 m and panchromatic band

is at 5 m GSD. THR (Very High-Resolution) is a 2.5 m sampled images in the same panchromatic band, namely the thanks to two staggered CCD arrays shifted one from the other 0.5 meter in the cross-track direction and 3.45 m in the along-track direction in focal plane by the process called “Supermode”. Both HRG instruments have a pointing mirror, allowing the viewing angle from nadir to vary within a range of  $\pm 27^\circ$ . This tracking capacity allows high revisit frequency and cross-track stereo-acquisition capability. HRS is able acquire stereopairs in a single pass by two telescopes with an along-track viewing angle of  $20^\circ$  forwards and also backwards. Both telescopes have a focal length of 580 mm and a single CCD array consisting of 12000 pixels projected on the ground as 120 km. The B/H ratio is close to 0.8. The ground resolution is 10 m, but the sampling rate is 5 m along the track allowing a higher elevation precision of DEM with  $\pm 4$  m RMSE to be obtained (Gleyzes *et al.* 2003). Vegetation-2 instruments has 1 km geometric resolution and 2250 km wide-swath, and its capacity allows covering land mass of the earth in one day (Fontannaz *et al.* 2002). DORIS antenna supplies the accurate position and velocities and also the absolute dating of the satellite whereas star tracker provides the attitude of the satellite.

#### 4.2.2 Images and metadata used

The images used in this thesis are stereo SPOT-5 HRG level 1A panchromatic images, provided by the joint research project, coded 104Y050, between TÜBİTAK (in Turkish: Türkiye Bilimsel ve Teknik Araştırma Kurumu, in English: The Scientific and Technical Research Council of Turkey) and JÜLICH Research Centre (Germany). Level 1A is the definition by SPOT Image meaning the images are only radiometric corrected to compensate the differences of sensitivities among the various elements of a CCD array (SPOT Image, 2002). So the level 1A image carries its original geometry. Specifications of images analysed are summarized in Table 4.1. Both images are in 5 m GSD and 8 bits (256 grey values) in Digital Image MAP (DIMAP) format with 12000 by 12000 pixels. The B/H ratio of stereo images is 0.54.

**Table 4.1:** Specifications for SPOT-5 HRG level 1A images

Specification	Left image	Right image
Date	13 <sup>th</sup> August 2003	14 <sup>th</sup> August 2003
Acquisition time for centre line	09: 03: 30.345268	08: 44: 14.552376
Time interval per line	0.00075199509335 sec	0.00075199660510 sec

The detailed metadata file provided by the image vendors includes many parameters related to the image. The parameters taken into account in this thesis are manually derived from the metadata file. These parameters are followings:

- Position and velocity vectors (i.e.  $\vec{P}_s$  and  $\vec{V}_s$ ) describing the orbit of satellite. These vectors are available in geocentric coordinates in International Terrestrial Reference Frame (ITRF), and produced by DORIS-DIODE system being acquired with 30 second time interval. The accuracy of orbit is reported as  $\pm 0.71$  m,  $\pm 0.67$  m and  $\pm 0.36$  m in  $X$ ,  $Y$ , and  $Z$  axis (SPOT Image, 2002). The number of samples for positions and velocities and their acquisition time is at 10 and 11 for the images dated 13<sup>th</sup> and 14<sup>th</sup> August 2003, respectively.
- Attitude angles ( $a_r$ ,  $a_p$  and  $a_y$ ) in radian. These angles are sampled 8 Hz (i.e. 8 per second) by onboard star tracker of SPOT-5. Totally 150 and 148 time dependent samples are available for the images dated 13<sup>th</sup> and 14<sup>th</sup> August 2003, respectively.
- Look angles for each elements of linear array ( $\psi_x$  and  $\psi_y$ ) in radian, defining the transformation between scanline and payload coordinate systems. These look angles are given for each 12000 elements of CCD array.

The position and velocity vectors and attitude angles define the exterior orientation whereas look angles supplies the interior orientation.

#### 4.2.3 Points observed by GPS survey

47 points in total are measured with GPS observations collected at 15 seconds intervals in static mode for relative positioning, using TOPCON TURBO-SII GPS receiver and each session took about 15 minutes. The geocentric coordinates of points are produced in WGS-84 by the software package of TOPCON, and their horizontal and vertical accuracies are  $\pm 0.06$  m and  $\pm 1.00$  m, respectively. The points are distributed as homogeneous as on both horizontal and vertical planes (Figure 4.2). However accessibility of the points during field survey was the major obstacle considering mountainous and forestry characteristic of Zonguldak test field. The points were obtained generally on the road intersections, centre of short and narrow bridges etc. which are sharp on the image. The GPS observation of all points was performed by the team from Zonguldak Karaelmas University Department of

Geodesy and Photogrammetry Engineering, and photographed to point them into their correct position on PCI Geomatica OrthoEngine software.

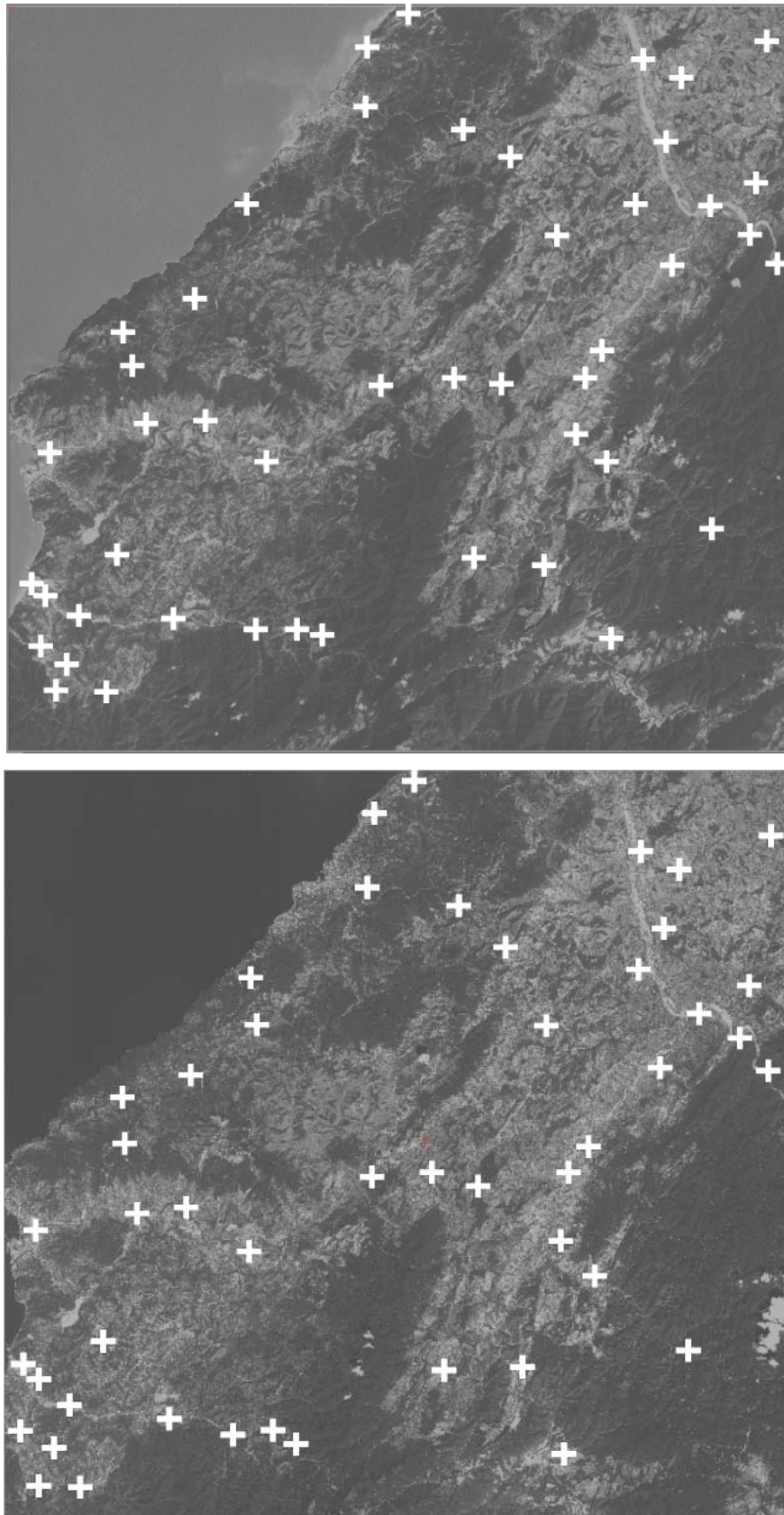


**Figure 4.2:** Distribution of points on the image dated 13<sup>th</sup> and 14<sup>th</sup> August 2003 above and below, respectively.



**Figure 4.3:** One of the points selected on road intersection (left hand-side) and scene of GPS observation in the field (right hand-side).

### 4.3 Programming

All calculations and graphical presentations in the section 4.4.2 including analysis results of this thesis are coded by the author in the MATLAB 7.0 environment ignoring some usage of functions in MATLAB library such as inversing or transposing the matrix etc. The derived program called GeoSpot-1.0 consist the steps graphically shown in Figure 4.4.

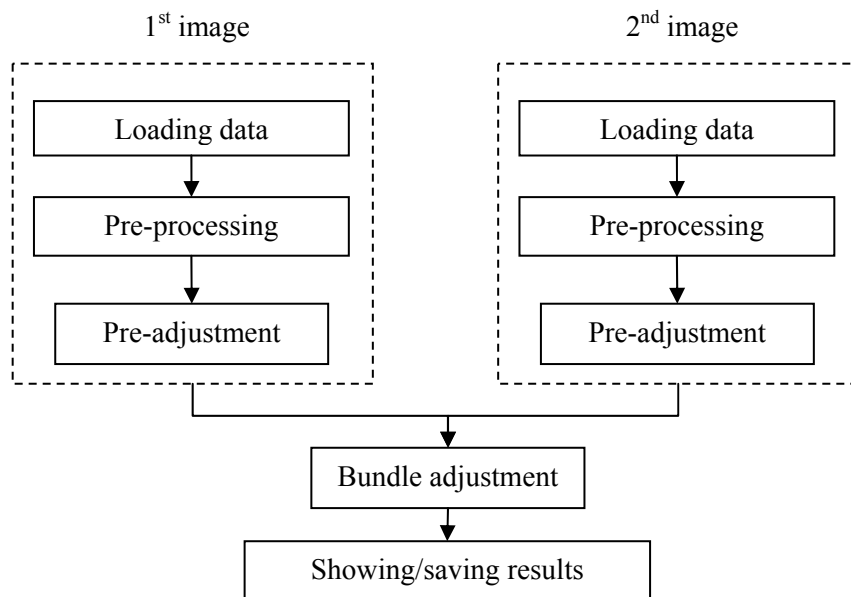


**Figure 4.4:** Main steps of developed program (GeoSpot-1.0).

The definitions of stages of program GeoSpot-1.0 are explained in the following sections.

### 4.3.1 Loading data

This stage includes the following steps for both images:

- i. Reading ID, line ( $x$ ) and column ( $y$ ) position, i.e. image coordinates, and GPS surveyed ground ( $X, Y, Z$ ) coordinates of each point,
- ii. Reading position ( $\vec{P}_s$ ) and velocity ( $\vec{V}_s$ ) of samples on the satellite orbit, and their acquisition time in hour, minute and second mode.
- iii. Reading the attitude angles ( $a_r, a_p, a_y$ ) and their acquisition time in hour, minute and second mode.
- iv. Reading the look angle ( $\psi_x$  and  $\psi_y$ ) of each elements of CCD array.
- v. Reading header information including the line and column position for the centre of image, time interval per line and acquisition time for the centre line.

### 4.3.2 Pre-processing

This stage includes the following steps remembering the section 3.3.1.2:

- i. The position and velocity for all 47 points considering their line ( $x$ ) position are estimated using the Lagrange interpolation.
- ii. The attitude angles for all 47 points considering their line ( $x$ ) position are estimated using the linear interpolation.
- iii. The coefficients of polynomial modelling ( $P_\theta, \dot{P}$  and  $\ddot{P}$ ) for position, velocity and attitudes angles are estimated by 2<sup>nd</sup> order polynomial. So totally 27 coefficient are estimated with this method.
- iv. The look angles for all 47 points considering their column ( $y$ ) position are estimated using the linear interpolation.

Figure 4.5 illustrates given time dependent positions of satellite both given in metadata and estimated for each points, and also the GPS observed positions of points.

### 4.3.3 Pre-adjustment

This stage varies in two types as mentioned in the Section 3.3.3.1. The first one consists pre-adjustment of look angles assuming the parameters are constant. The second type of pre-adjustment depends on an additional step to the first type, i.e. the adjusted look angles in the first type are assumed constant and the parameters are adjusted. The pre-adjustment is performed using only GCPs.

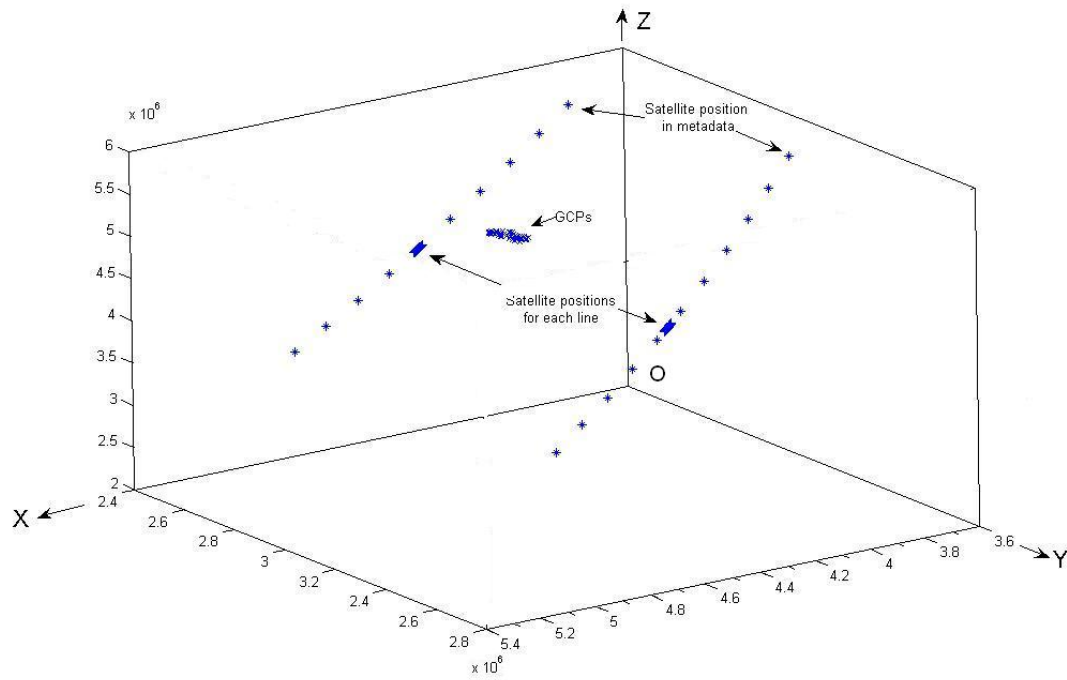


**Figure 4.5:** Plotting of positions of both satellite (given in metadata and estimated for each points) and points.

The graphical representation of both types of pre-adjustment is illustrated in Figure 4.6. The second type pre-adjustment runs at most 3 times. However this limit can be changed if it is required. Here  $\Delta P = dP_{j+1} - dP_j$  where  $j$  is iteration number and  $\Delta$  is the threshold. The adjusted look angles and parameters of each images are introduced into the bundle adjustment.

#### 4.3.4 Bundle adjustment

This stage varies according to the pre-adjustment performed in two types. In the first type, the bundle adjustment compensates adjusted look angles and non-adjusted EOPs derived from the first type pre-adjustment, and also object coordinates of check points. In the second one, both the look angle and parameters introduced into bundle adjustment are adjusted together in the pre-adjustment. The comparative results are presented into the following section.

#### 4.4 Geometric Analysis

The results of geometric analysis are presented in this section. At first the organization of the geometric analysis is mentioned to guide the reader. Then the analysis results are presented. Finally the results are concluded.



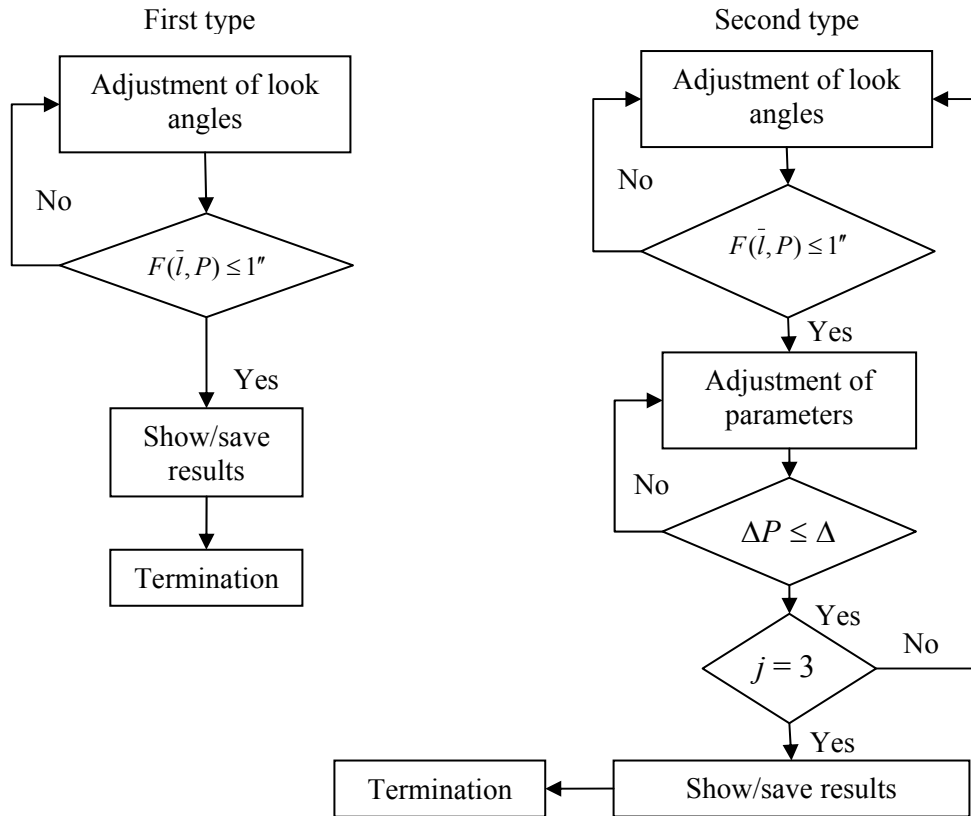
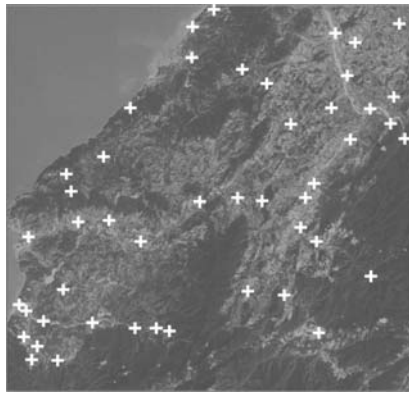


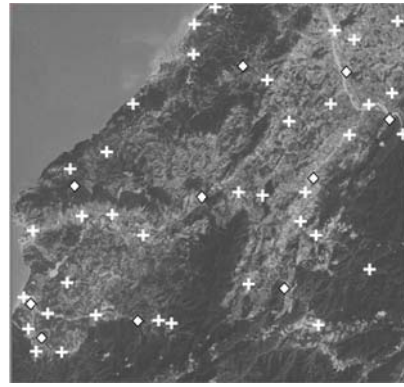
**Figure 4.6:** Steps of pre-adjustment.

#### 4.4.1 Preface of Geometric Analysis

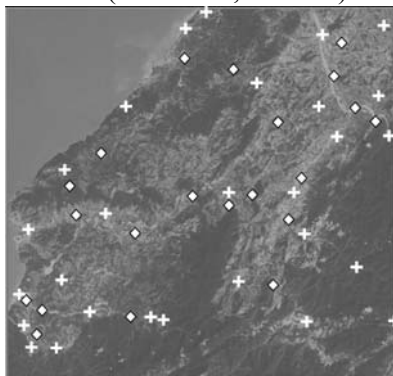
The geometric analysis is performed on the geometric accuracy on points (GCPs or ICPs) with respect to look angles and parameters. In other words, the ground coordinates of points in meter unit are estimated using look angles and parameters with their approximate and adjusted values, and this estimated coordinates are compared with their GPS observed values. 7 point sets and 19 EOP sets are configured. The distribution of GCPs and ICPs in various configurations on the image dated 13<sup>th</sup> August 2003 is shown in Figure 4.7. The points are homogeneously distributed (H) locating the ICPs covered by GCPs, i.e. the GCPs are always located at the corners and borders of the images. The grouped distribution (G) depends on the grouping GCPs and ICPs as shown in Figure 4.7. The motivation in the grouped set is to see effects of accumulated distribution of GCPs and ICPs on the image. The  $y$  coordinate of ICPs in the set G-A is smaller than 6001, the  $x$  coordinate of ICPs in the set G-B is smaller than 6001, and the  $x$  and  $y$  coordinates of GCPs in the set G-C are smaller and bigger than 6001, respectively.



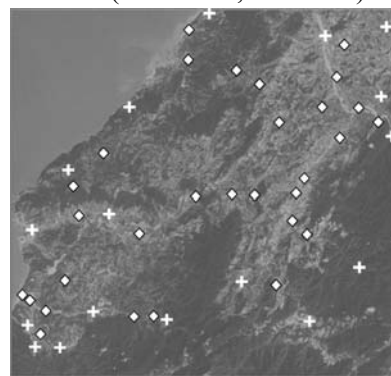
H-0 (#GCP: 47, #ICP: 0)



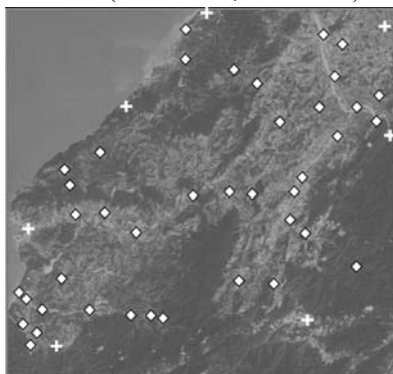
H-10 (#GCP: 37, #ICP: 10)



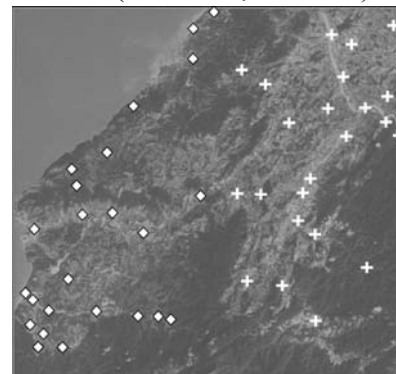
H-20 (#GCP: 27, #ICP: 20)



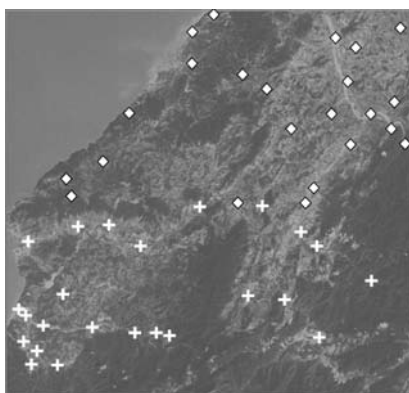
H-30 (#GCP: 17, #ICP: 30)



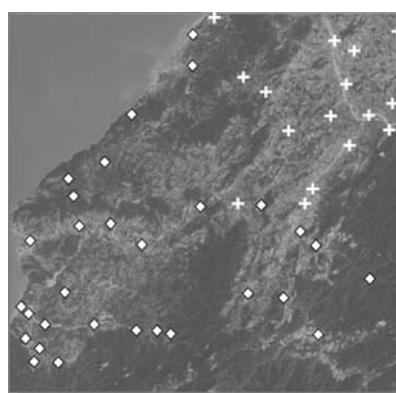
H-40 (#GCP: 7, #ICP: 40)



G-A (#GCP: 23, #ICP: 24)



G-B (#GCP: 24, #ICP: 23)



G-C (#GCP: 17, #ICP: 30)

**Figure 4.7:** Various configuration of point distribution. (H: Homogenous distribution, G: Grouped distribution, +: GCP, ◇: ICP)

The EOP sets are established in various configurations as listed in Table 4.2. Actually, no optimal or correct set of adjustment parameter has been proposed in the previous studies with the choice of adjustment parameters varies (Kim *et al.*, 2007). However the overparameterisation problem occurred when all parameters were chosen as adjustment parameters, caused by high correlation among the parameters occurring diverging of adjustment. The effects of parameter choice on the results can be examined for the various parameter sets listed in Table 4.2. The reader must notice that unknowns of ground coordinates ( $X$ ,  $Y$ , and  $Z$ ) are added these parameter sets for the ICPs in the bundle adjustment process.

**Table 4.2:** Configurations of choosing EOP as adjustment parameter

No	ID	Adjusted EOPs
1	P <sub>S</sub>	$X_o, \dot{X}, \ddot{X}, Y_o, \dot{Y}, \ddot{Y}, Z_o, \dot{Z}, \ddot{Z}$
2	P <sub>S0</sub>	$X_o, Y_o, Z_o$
3	P <sub>S1</sub>	$\dot{X}, \dot{Y}, \dot{Z}$
4	P <sub>S2</sub>	$\ddot{X}, \ddot{Y}, \ddot{Z}$
5	V <sub>S</sub>	$V_{Xo}, \dot{V}_X, \ddot{V}_X, V_{Yo}, \dot{V}_Y, \ddot{V}_Y, V_{Zo}, \dot{V}_Z, \ddot{V}_Z$
6	V <sub>S0</sub>	$V_{Xo}, V_{Yo}, V_{Zo}$
7	V <sub>S1</sub>	$\dot{V}_X, \dot{V}_Y, \dot{V}_Z$
8	V <sub>S2</sub>	$\ddot{V}_X, \ddot{V}_Y, \ddot{V}_Z$
9	A	$a_{ro}, \dot{a}_r, \ddot{a}_r, a_{po}, \dot{a}_p, \ddot{a}_p, a_{yo}, \dot{a}_y, \ddot{a}_y$
10	A <sub>0</sub>	$a_{ro}, a_{po}, a_{yo}$
11	A <sub>1</sub>	$\dot{a}_r, \dot{a}_p, \dot{a}_y$
12	A <sub>2</sub>	$\ddot{a}_r, \ddot{a}_p, \ddot{a}_y$
13	P <sub>S</sub> V <sub>S</sub>	$X_o, \dot{X}, \ddot{X}, Y_o, \dot{Y}, \ddot{Y}, Z_o, \dot{Z}, \ddot{Z}, V_{Xo}, \dot{V}_X, \ddot{V}_X, V_{Yo}, \dot{V}_Y, \ddot{V}_Y, V_{Zo}, \dot{V}_Z, \ddot{V}_Z$
14	(P <sub>S</sub> V <sub>S</sub> ) <sub>0</sub>	$X_o, Y_o, Z_o, V_{Xo}, V_{Yo}, V_{Zo}$
15	P <sub>S</sub> A	$X_o, \dot{X}, \ddot{X}, Y_o, \dot{Y}, \ddot{Y}, Z_o, \dot{Z}, \ddot{Z}, a_{ro}, \dot{a}_r, \ddot{a}_r, a_{po}, \dot{a}_p, \ddot{a}_p, a_{yo}, \dot{a}_y, \ddot{a}_y$
16	(P <sub>S</sub> A) <sub>0</sub>	$X_o, Y_o, Z_o, a_{ro}, a_{po}, a_{yo}$
17	V <sub>S</sub> A	$V_{Xo}, \dot{V}_X, \ddot{V}_X, V_{Yo}, \dot{V}_Y, \ddot{V}_Y, V_{Zo}, \dot{V}_Z, \ddot{V}_Z, a_{ro}, \dot{a}_r, \ddot{a}_r, a_{po}, \dot{a}_p, \ddot{a}_p, a_{yo}, \dot{a}_y, \ddot{a}_y$
18	(V <sub>S</sub> A) <sub>0</sub>	$V_{Xo}, V_{Yo}, V_{Zo}, a_{ro}, a_{po}, a_{yo}$
19	(P <sub>S</sub> V <sub>S</sub> A) <sub>0</sub>	$X_o, Y_o, Z_o, V_{Xo}, V_{Yo}, V_{Zo}, a_{ro}, a_{po}, a_{yo}$

The results are presented in tables and graphical presentations. The points are located on their image coordinates ( $x$  and  $y$ ) whereas the residuals are plotted in meter unit. The scale can be varied for GCPs and ICPs on the same figure.

#### 4.4.2 Results Achieved

As mentioned in the previous sections, the ground coordinates of GCPs and ICPs using approximate and adjusted values of look angles and EOPs are estimated and compared with their GPS surveyed coordinates. The results are reported in two sections. The first one includes the results using the first type of pre-adjustment, i.e. adjusting only look angles in the pre-adjustment process. The second one depends on adjustment of both look angles and adjustment parameters in the pre-adjustment process.

##### 4.4.2.1 Results based on first type pre-adjustment

The first results of this section listed in Table 4.3 are achieved by comparison between GPS surveyed and estimated ground coordinates of points. The estimation is performed using approximate and adjusted look angles without adjustment of EOPs both in the stages of pre-adjustment and bundle adjustment. In other words the EOPs are assumed as constant in these two stages.

**Table 4.3:** RMSE of GCPs and ICPs using approximate and adjusted look angles

Point			$L$			$\bar{L}$			$B$		
set	type	#	$m_X$	$m_Y$	$m_Z$	$m_X$	$m_Y$	$m_Z$	$m_X$	$m_Y$	$m_Z$
H-0	GCP	47	1230150.23	762556.41	1260608.51	0.515	0.169	0.928	-	-	-
H-10	GCP	37	1230020.35	762582.93	1260714.43	0.515	0.169	0.928	0.603	0.219	0.975
	ICP	10	1230630.66	762458.25	1260216.54	6.065	5.768	6.461	5.970	5.745	6.609
H-20	GCP	27	1230372.88	762579.15	1260424.05	0.515	0.169	0.928	0.620	0.220	0.970
	ICP	20	1229849.58	762525.70	1260857.50	4.782	5.335	5.943	4.827	5.310	6.174
H-30	GCP	17	1230851.61	762294.90	1260277.25	0.514	0.170	0.927	0.593	0.226	0.968
	ICP	30	1229752.60	762704.55	1260796.18	4.992	5.996	5.936	5.208	5.937	6.219
H-40	GCP	7	1229216.73	763039.36	1261574.80	0.516	0.168	0.929	0.569	0.236	1.045
	ICP	40	1230313.51	762471.86	1260439.33	6.793	6.966	6.107	7.216	6.814	6.327
G-A	GCP	23	1226524.57	766698.58	1260566.64	0.530	0.157	0.937	0.678	0.194	0.925
	ICP	24	1233614.81	758565.60	1260648.63	24.751	33.251	7.079	25.643	32.499	6.921
G-B	GCP	24	1234135.02	760543.55	1258344.29	0.509	0.174	0.923	0.500	0.203	1.010
	ICP	23	1225978.37	764651.13	1262966.85	5.601	5.939	9.678	5.257	5.871	10.000
G-C	GCP	17	1224884.38	766662.14	1262500.62	0.528	0.157	0.937	0.720	0.214	0.892
	ICP	30	1233124.22	760219.98	1259535.05	29.166	54.568	6.825	30.009	53.557	6.790

$L$  : approximate look angle,  $\bar{L}$  : pre-adjusted look angle,  $B$ : bundle adjustment, RMSE ( $m$ ) is  $\pm$  meter

The effect of look angles can be easily realized when the results are examined. The RMSE values are significantly reduced for all point sets and also types. The RMSE of GCPs in all sets are sub-meter level and almost equal with adjusted look angles, meaning possibly the model is fitting on the GCPs very well. However, the RMSEs of ICPs are about  $\pm 5$  m, i.e.  $\pm 1$  pixel, in all sets except G-A and G-C. The RMSEs

larger than  $\pm 5$  m in the sets G-A and G-C for ICPs depends on their distribution on the images remembering the Figure 4.7. The reason of this situation is that the adjusted look angles of ICPs are based on the adjusted look angles of GCPs. When the GCPs located on only the right or left half of image, the look angles on outside GCPs, i.e. on the area of ICPs, are extrapolated with the help of adjusted look angles of GCPs. In other words, the half of one line has adjusted look angles by GCPs while other side has extrapolated look angles related to the column number ( $y$ ) of a line. This problem had not occurred for the ICPs of G-B since the GCPs lay on whole line on this point set.

The residual errors at GCPs and ICPs are plotted in Figures 4.8 for all GCPs (H-0) and in Figure 4.9 and 4.10 for other sets using different scales for GCPs and ICPs. The residual errors are systematic using both approximate and pre-adjusted look angles in the Figure 4.8. If the pre-adjusted look angles are used the errors on GCPs are systematic for all point sets as shown in Figure 4.9 and 4.10. However this systematic effect is not observed in the bundle adjustment.

ICPs have no systematic errors in all point sets homogenously distributed (H) and in G-B. The ICPs in the sets G-A and G-C have similar systematic errors growing in the bottom side of images. This systematic effect means the GPS surveyed position of the GCPs is on upper-right in planimetry and below in height against their estimated position. Notably, the magnitude and the direction of residual errors of both GCPs

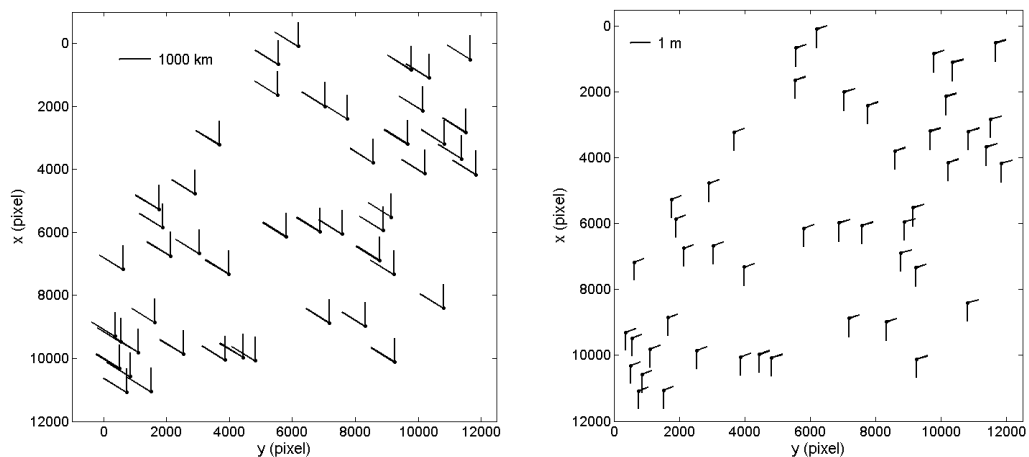
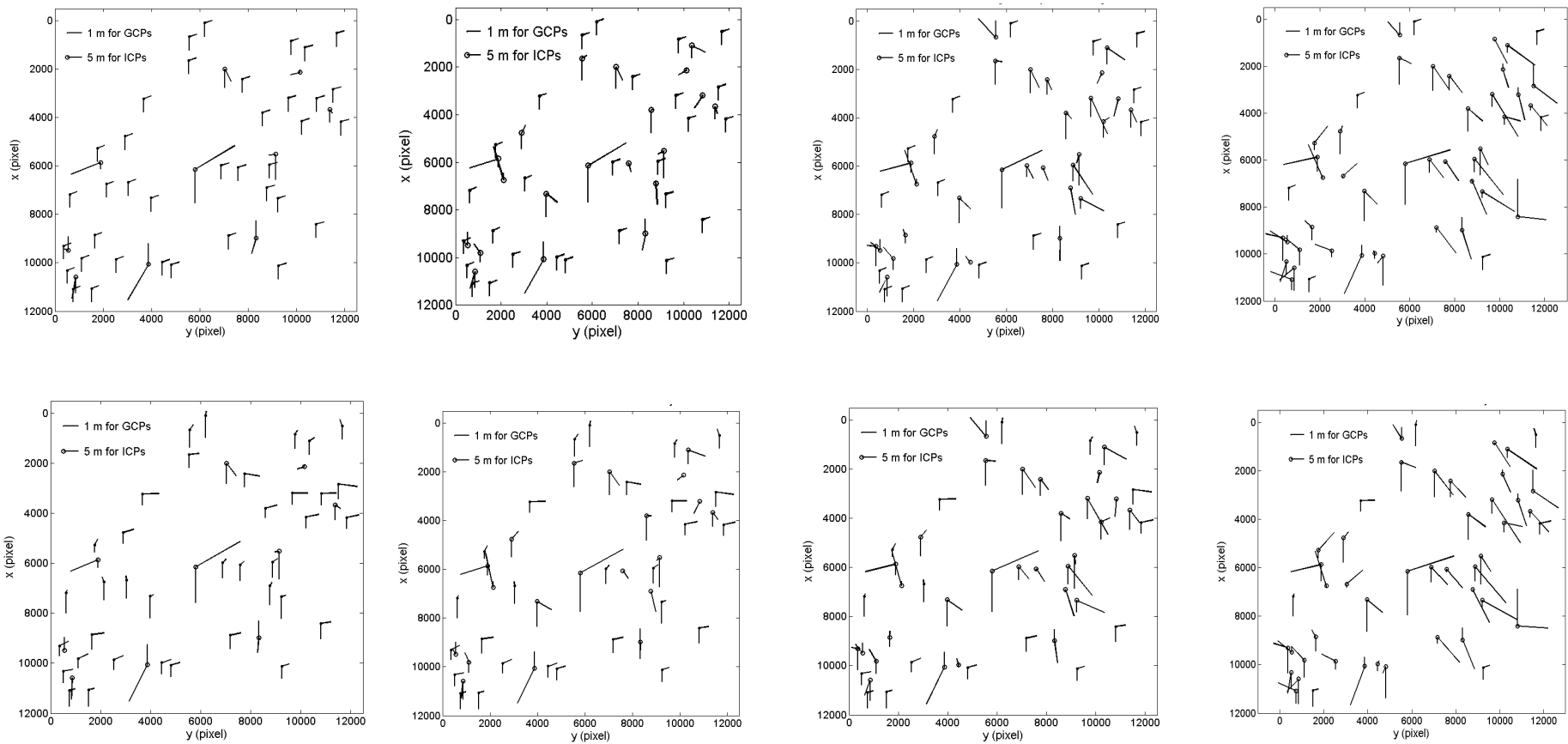


**Figure 4.8:** Plot of residual errors in planimetry (diagonal) and in height (up-down) at all GCPs (H-0). left: using approximate look angles, right: using pre-adjusted look angles.



H-10

H-20

H-30

H-40

**Figure 4.9:** Plot of residual errors in planimetry (diagonal) and in height (up-down) at GCPs and ICPs for homogenously distributed point sets. (above: results of pre-adjusted look angles, below: results of bundle adjusted look angles, H: Homogenous distribution, G: Grouped distribution,  $\bullet$ : GCP,  $\circ$ : ICP).

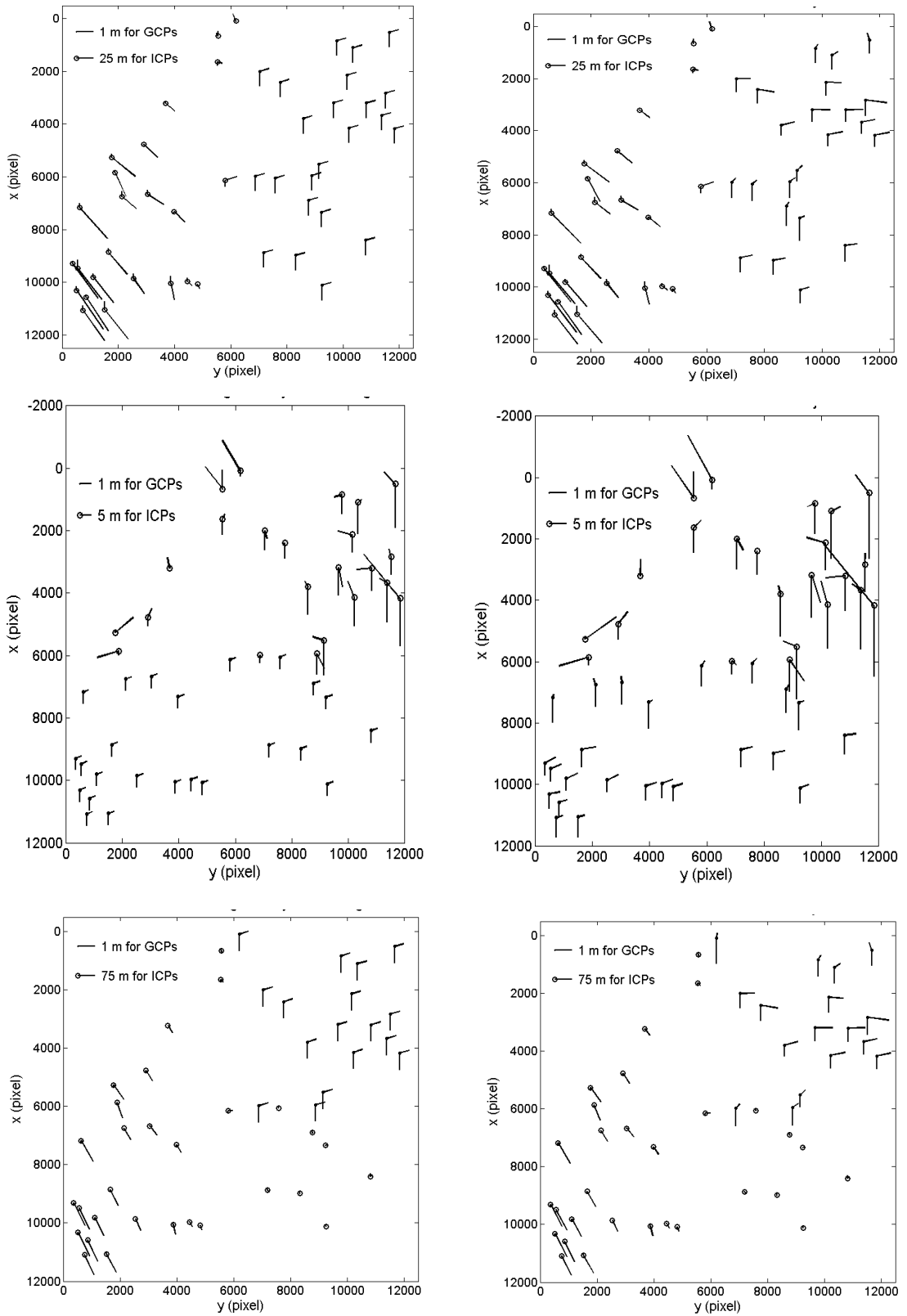


**Figure 4.10:** Plot of residual errors in planimetry (diagonal) and in height (up-down) at GCPs and ICPs for grouped point sets (from above to below: G-A, G-B, G-C). left: results of pre-adjusted look angles, right: results of bundle adjustment. (H: Homogenous distribution, G: Grouped distribution, •: GCP, o: ICP).

and ICPs are almost similar. For instance the ICP located in the centre of image has equal residual errors with respect to direction and magnitude in all homogeneously distributed images in Figure 4.9.

These results mean that the approximate values of EOPs can be assumed correct and used for adjustment of look angles. However the point distribution must have homogenous distribution to reach at least about  $\pm 1$  pixel ( $\pm 5$  m) accuracy for the ICPs. This must be taken into account that the look angles of images are adjusted within running the pre-adjustment for each image individually while they and EOPs are adjusted in bundle adjustment at the same time.

The RMSE of GCPs and ICPs in the bundle adjustment are generally larger than in the results of pre-adjusted look angles. Thus, the bundle adjustment has no improvement on the results according to the Table 4.3. Nevertheless, the systematic effect on the residual errors of GCPs is not observed following the bundle adjustment (Figure 4.9 and 4.10). Here the EOPs are not adjusted and assumed constant, and the ground coordinates of ICPs are assumed as the adjustment parameters in the bundle adjustment.

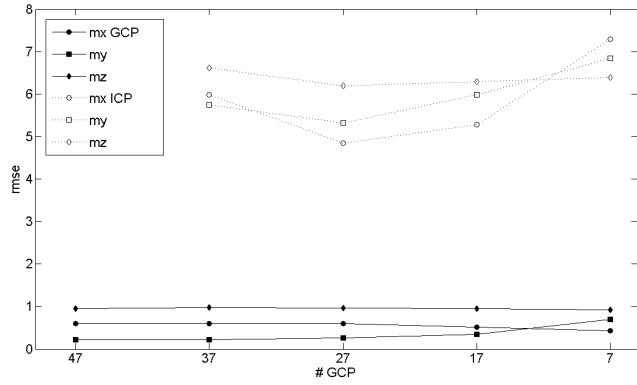
The second and final results of this section are related to the various EOP sets. The effect of various EOP sets on the accuracy of GCPs and ICPs are analysed presenting the results in Appendix A.5.1. The results of bundle adjustment are almost equal to the first results of this section for the parameter sets from 1<sup>st</sup> to 11<sup>th</sup> except the 5<sup>th</sup> set. In other words the accuracy is generally sub-meter for the GCPs and about  $\pm 1$  pixel ( $\pm 5$  m) for the ICPs on the sets having homogeneously distributed points (H). Other EOP sets, i.e. 5<sup>th</sup> and from 13<sup>th</sup> to 19<sup>th</sup>, have inaccurate results especially for the GCPs; on the other hand, ICPs have accurate ground coordinates about  $\pm 1$  pixel ( $\pm 5$  m). This has to be taken into account that the true ground coordinates of GCPs are estimated using the adjusted both EOPs and look angles intersecting two images where the true ground coordinates of ICPs are some of the adjustment parameters in the bundle adjustment. If the results are assessed following this explanation, the accuracy of GCPs is blurred by the 5<sup>th</sup> and from 13<sup>th</sup> to 19<sup>th</sup> EOP sets. This results means that the unknowns of EOPs are inaccurate as a result of the correlation among the elements of these EOP sets.



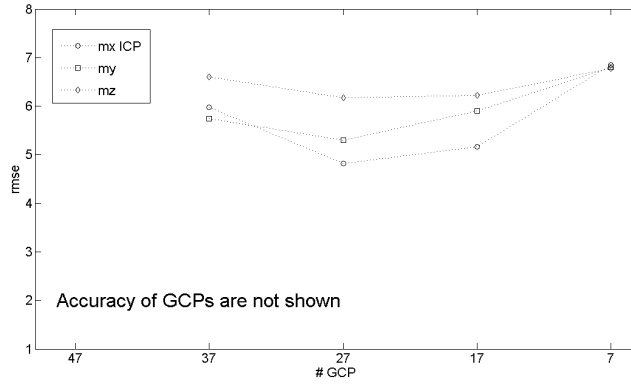
The accuracy of point sets is mostly varied by the EOP sets. The adjusted EOP sets excepting the 5<sup>th</sup> and from 13<sup>th</sup> to 19<sup>th</sup>, the accuracy of GCPs are generally sub-meter level whereas the accuracy of ICPs are about  $\pm 1$  pixel ( $\pm 5$  m) and between  $\pm 1$  pixel ( $\pm 5$  m) and  $\pm 20$  pixels ( $\pm 100$  m) in the point sets homogenously distributed and grouped, respectively. The results based on these adjusted EOP sets are graphically illustrated in the Figures 4.11 and 4.12. Generally the accuracies of GCPs are smaller than  $\pm 1$  m being  $m_z > m_x > m_y$ . The accuracy in height ( $Z$ ) is generally larger than the accuracy in the planimetry ( $X$  and  $Y$ ). Here the accuracy of  $Y$  is the highest since this axis is related to the look angles which is important on the estimation of true ground coordinates (see Table 4.3). The effects of the 5<sup>th</sup> and from 13<sup>th</sup> to 19<sup>th</sup> parameter sets can be negligible if the Figures 4.11 and 4.12 are examined. Only the sets V and V<sub>o</sub> including all velocity elements and the constant terms, respectively, are separated from the other parameter sets. The set V has inaccurate accuracy on the GCPs whereas the accuracy of its ICPs is acceptable. The set V<sub>o</sub> is blurring the accuracy on the GCPs whereas there is no any problem with the ICPs. Other results based on EOP sets from 13<sup>th</sup> and 19<sup>th</sup> are not shown since the accuracy of GCPs is extremely less.

The sets 5<sup>th</sup>, 6<sup>th</sup> and from 13<sup>th</sup> to 19<sup>th</sup> cause inaccurate results on the grouped points (G) as similar as in the homogenously distributed points (H). The higher accuracy on the GCPs is reached on the point set G-C whereas others have lower. The cause of these inaccurate results on G-A and G-C is based on the dependency of look angles with column number ( $y$ ) remembering the similar results achieved in the Table 4.3. The graphical representation of the accuracies of grouped point sets are not shown unlike in Figures 4.12 since there is no any continuity among them.

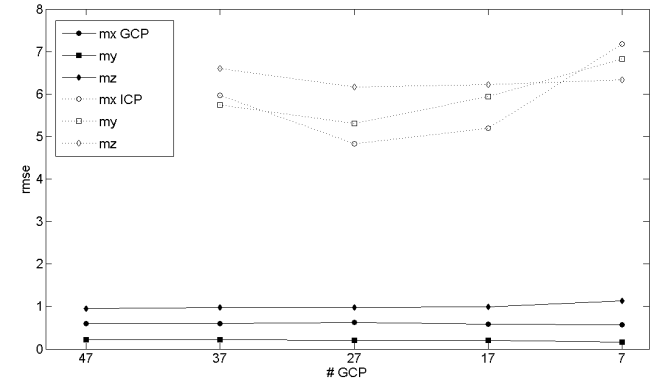
Finally this can be concluded that the accuracy of GCPs and ICPs are not changing significantly with respect to number of points and the type of EOP sets, excepting 5<sup>th</sup>, 6<sup>th</sup>, 13<sup>th</sup>-19<sup>th</sup> set. And the most accurate results are available if the EOPs are used individually. In other words, if position, velocity and attitude angles are adjusted together (EOP sets from 13<sup>th</sup> to 19<sup>th</sup>), the high correlation among them is possibly occurred and the inaccurate results are produced. All residual errors can be plotted for each results depending of each EOP sets. However some of them are chosen and shown in Figure 4.13 instead to show all of them. Here, the general situation is that



$P_S$  (above)  $P_{S_0}$  (below)



$V_S$  (above)  $V_o$  (below)



$A$  (above)  $A_o$  (below)

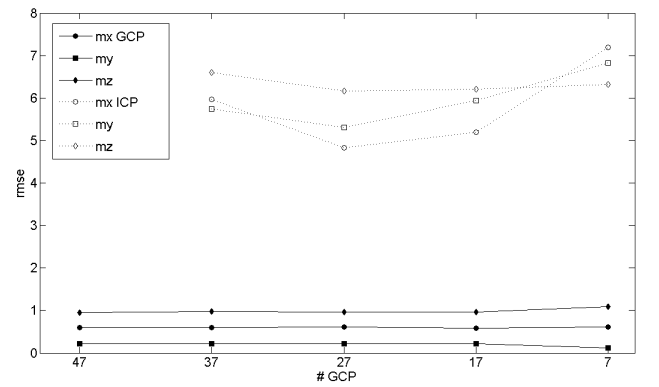
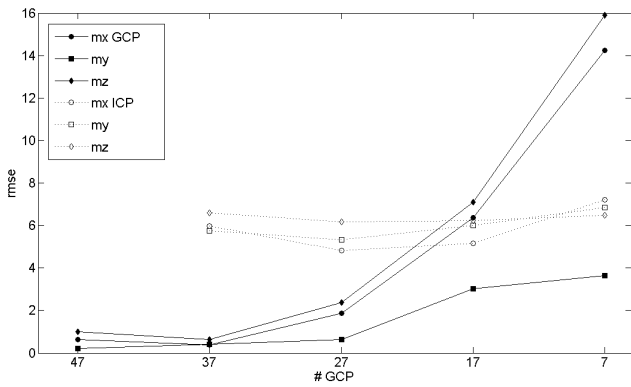
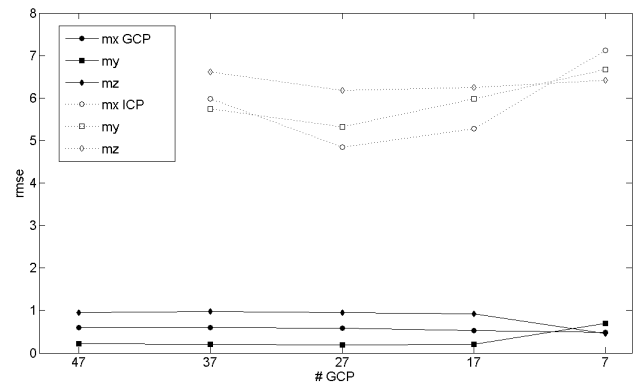
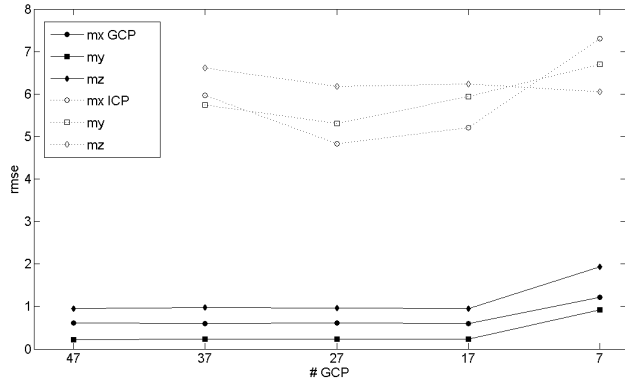
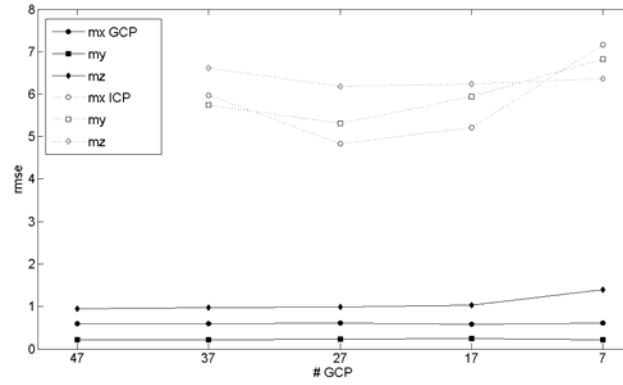


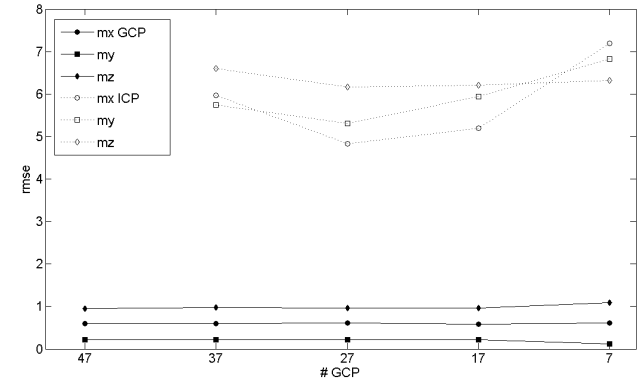
**Figure 4.11:** Graphical representation of accuracy of GCPs and ICPs in point sets homogenously distributed.



$P_{S1}$  (above)  $P_{S2}$  (below)



$V_1$  (above)  $V_2$  (below)



$A_1$  (above)  $A_2$  (below)

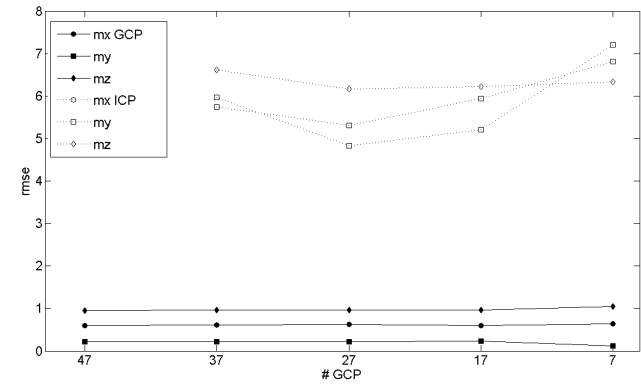
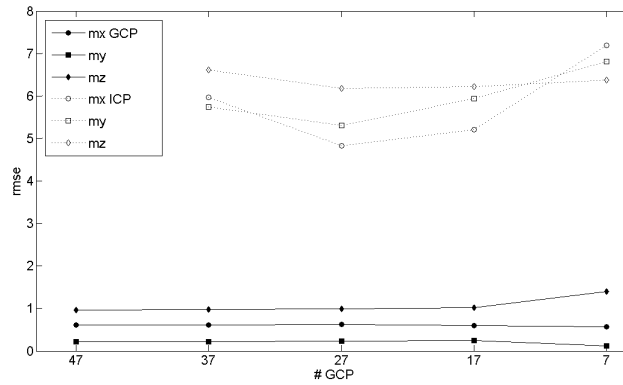
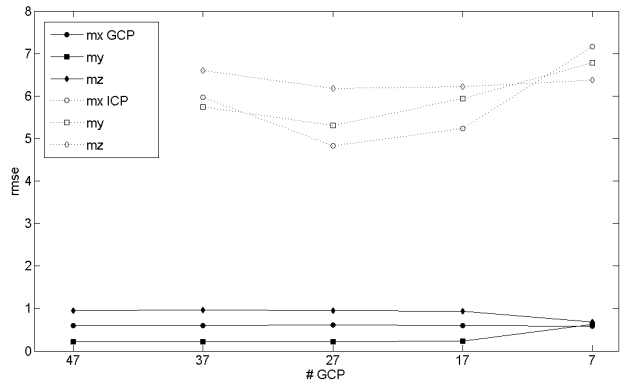
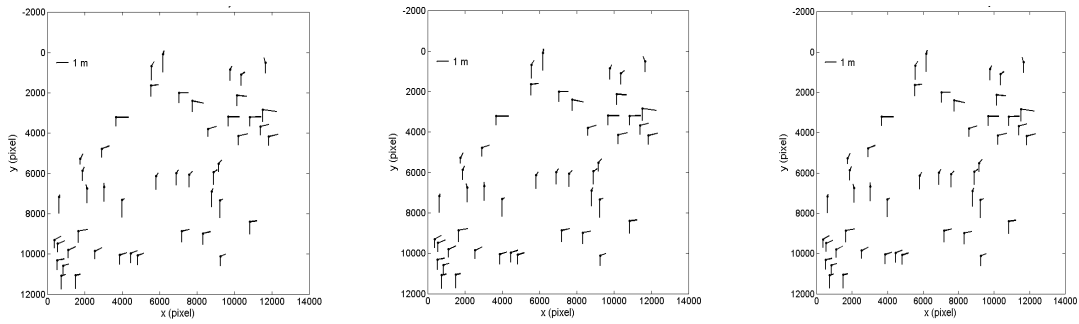
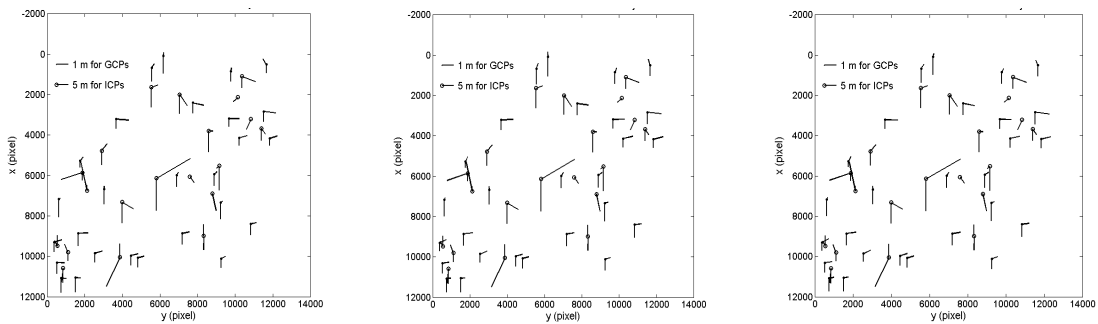


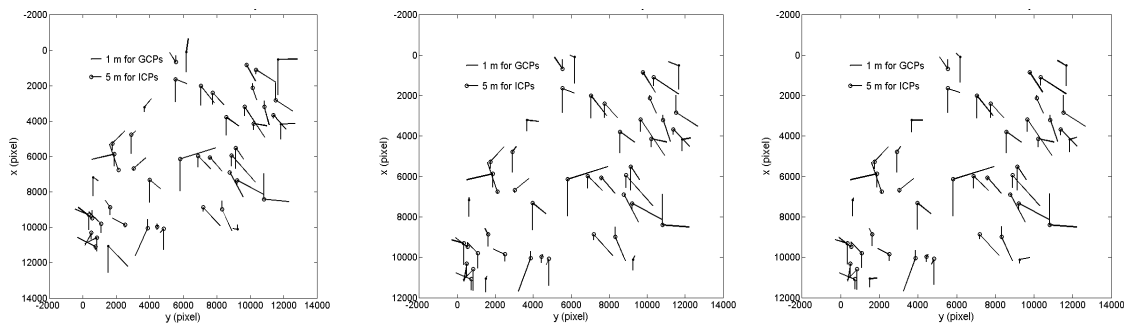
**Figure 4.12:** Graphical representation of accuracy of GCPs and ICPs in point sets homogenously distributed.



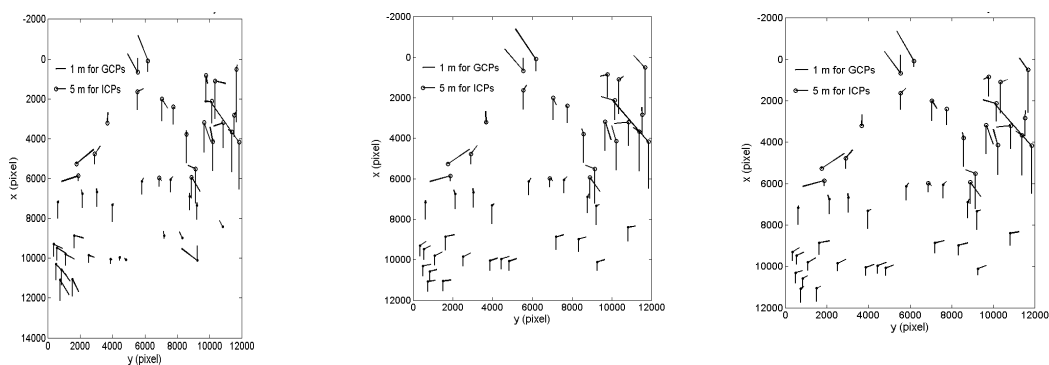
All GCPs (from left to right:  $P_S, V_1, A$ )



H-20 (from left to right:  $P_{S_0}, V_1, A_0$ )



H-40 (from left to right:  $P_{S_1}, V_1, A_1$ )



G-B (from left to right:  $P_{S_2}, V_2, A_2$ )

**Figure 4.13:** Plot of residual errors in planimetry (diagonal) and in height (up-down) at GCPs and ICPs for some point sets with respect to EOP sets. (H: Homogenous distribution, G: Grouped distribution,  $\bullet$ : GCP,  $\circ$ : ICP)

the direction and magnitude of the residuals errors are independent from the adjusted EOP, and they are almost same with the plots in Figure 4.9. This means the EOPs chosen to be adjusted do not affect the direction and magnitude of the residual errors. Here the major domination is based on the look angles adjusted. Only the GCPs located on left-below of the point set G-B have different geometry depending on the  $P_{S2}$ . Nevertheless this does not change the general condition.

#### 4.4.2.2 Results based on second type pre-adjustment

As mentioned several times, the difference between this and the previous sections depends on the pre-adjustment of EOPs. These EOPs are individually pre-adjusted for each image before their use in the bundle adjustment in this second type. Table 4.3 and Figure 4.8 in the previous section are valid for both sections. The results related to this section are summarized in the Appendix A.5.2 and A.5.3.  $\overline{LP}$  is the pre-adjusted look angles and EOPs where  $B$  is the bundle adjustment. At first, this can be said that both processes ( $\overline{LP}$  and  $B$ ) produce equal RMSEs for the point sets including all GCPs (H-0). And secondly the RMSEs based on  $\overline{LP}$  are sub-meter whereas they are blurred following the bundle adjustment for the EOPs from 13<sup>th</sup> to 19<sup>th</sup>. This can not be said that the bundle adjustment improves the RMSEs since some of them becomes equal in both processes ( $\overline{LP}$  and  $B$ ) where others of them becomes better or worse. Moreover, bundle adjustment gives inaccurate RMSEs for the GCPs for the EOP sets from 13<sup>th</sup> to 19<sup>th</sup>.

Figures 4.14 illustrates the plotting of residual errors of H-0 (including only GCPs) for some EOP sets such as  $P_s$ ,  $V_s$  and  $A$ . The direction and the magnitude of the residuals are almost similar depending on both the second type pre-adjustment (i.e. pre-adjusted look angles and EOPs) and the bundle adjustment. However the same examination has to be performed for the various point sets as shown in Figure 4.15 with various comparison. For instance, the residuals depending on the set  $P_{S0}$  for H-10, the pre- and bundle-adjustment have different results growing in the second one. The direction of the residual errors are similar, nevertheless the magnitude on GCPs and ICPs are growing in the bundle adjustment. Similarly the magnitude of residuals on GCPs are growing for the set  $V_0$  for H-20.  $A_0$  has almost equal results with respect to direction and magnitude of accuracies for the point set H-30 and G-A.

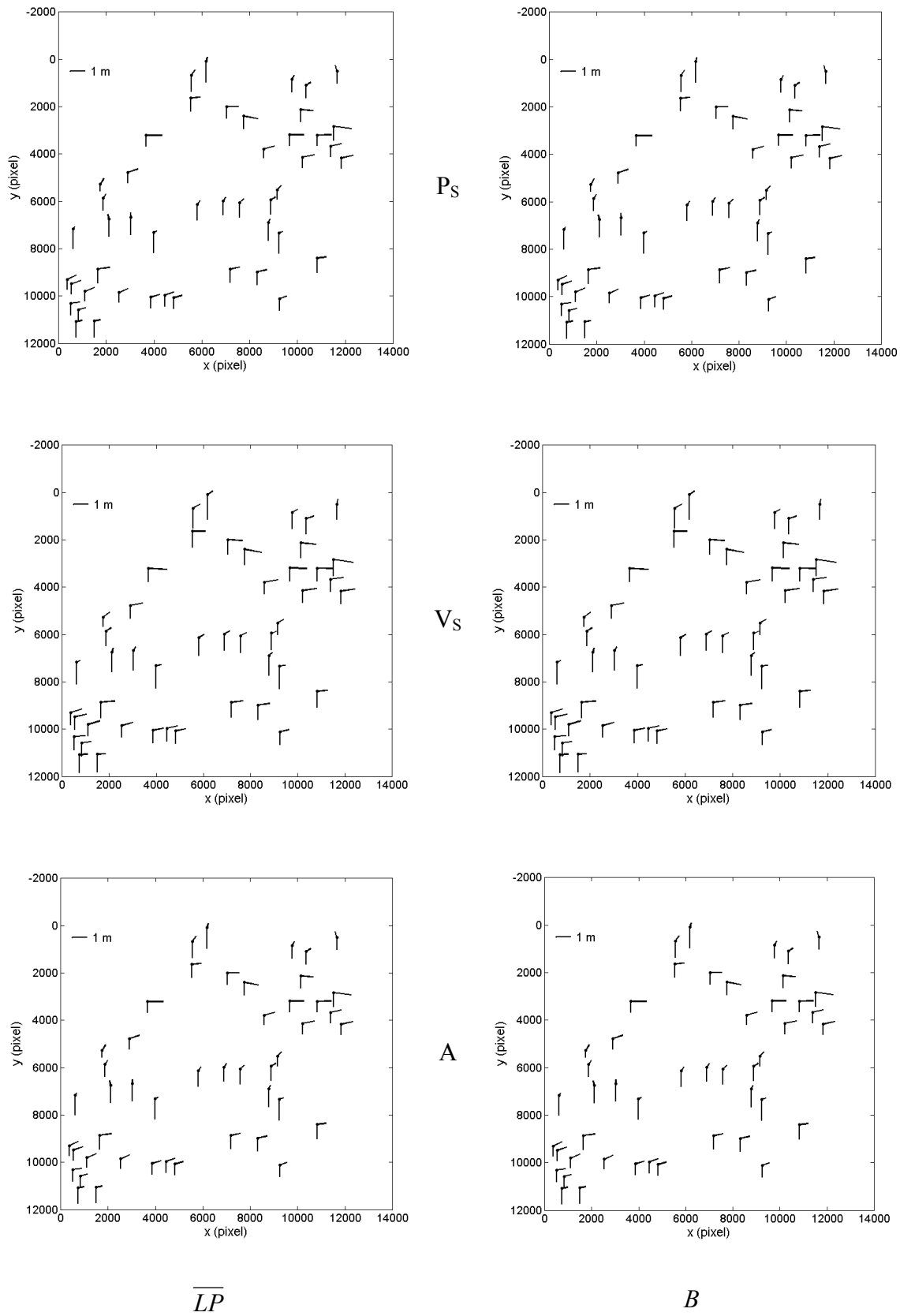


**Figure 4.14:** Plot of residual errors in planimetry (diagonal) and in height (up-down) at all GCPs for some EOP sets.

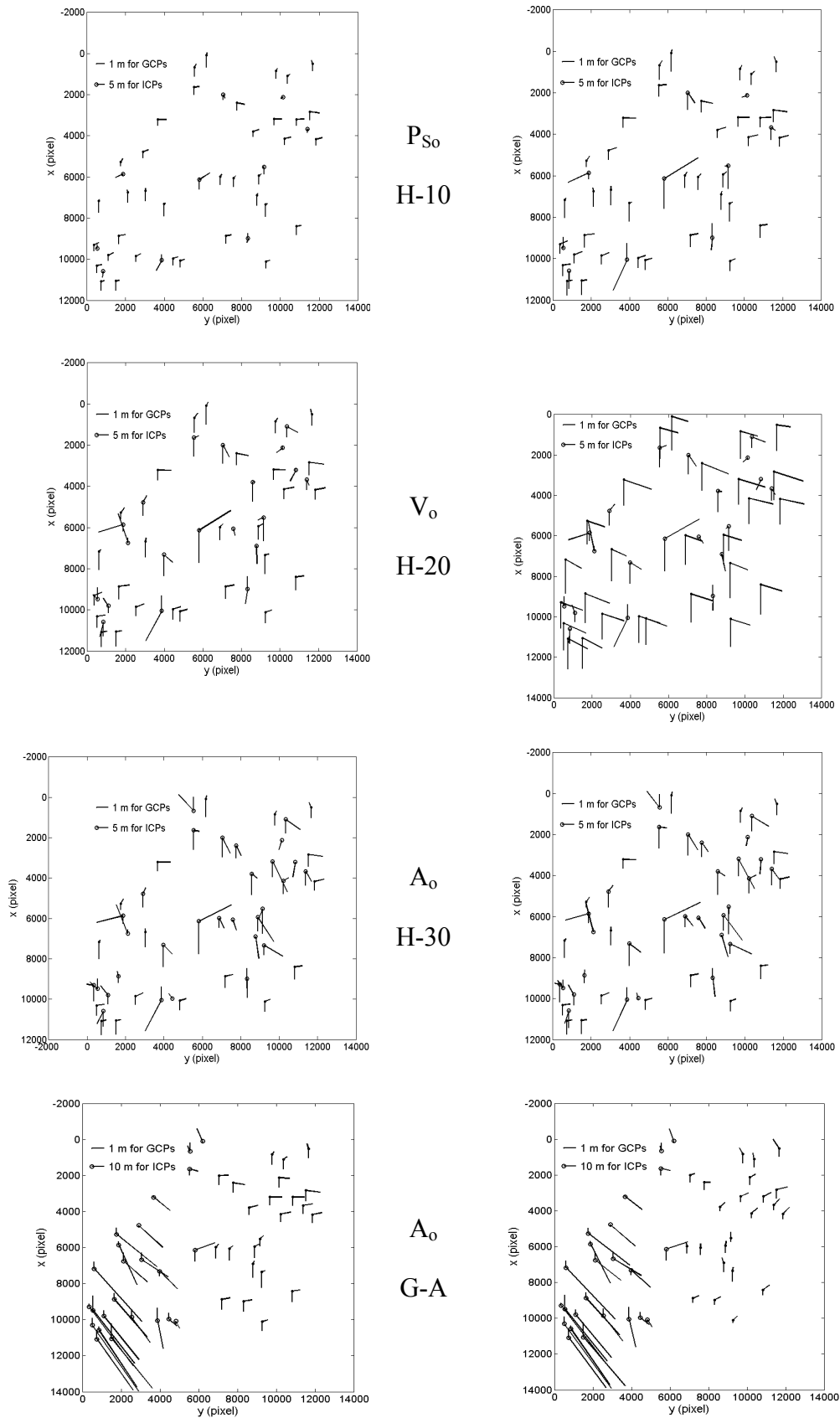


**Figure 4.15:** Plot of residual errors in planimetry (diagonal) and in height (up-down) for some sets of points and EOPs. (left: pre-adj., right: bundle adj., H: Homogenous, G: Grouped, •: GCP, o: ICP)

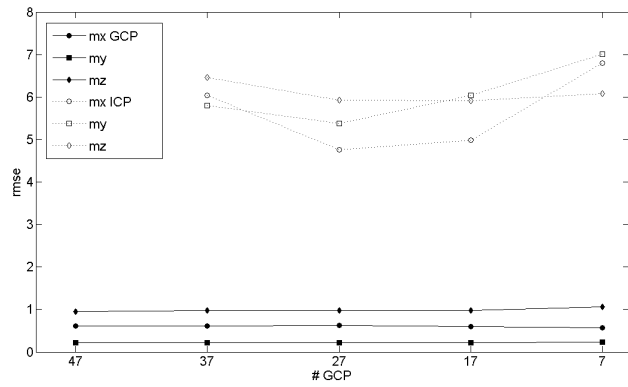
These examples chosen and shown in Figure 4.15 provides the direction and the magnitude of the residual errors can be changed depending on the EOP sets and the processing type (pre- or bundle adjustment). However the direction seems very strong against to be changed in the examples given. Similarly in the section of first type pre-adjustment, the accuracy is mostly varied by the EOP sets. The adjusted EOP sets excepting the 5<sup>th</sup> and from 13<sup>th</sup> to 19<sup>th</sup>, the accuracy of GCPs are generally sub-meter level as in the section related to the first type pre-adjustment. The accuracy of ICPs are about  $\pm 1$  pixel ( $\pm 5$  m) and from  $\pm 1$  pixel ( $\pm 5$  m) to  $\pm 20$  pixels ( $\pm 100$  m) in the point sets homogenously distributed and grouped respectively. The results based on these adjusted EOP sets are graphically illustrated in the Figure 4.16. Generally the accuracies of GCPs are smaller than  $\pm 1$  m being  $m_z > m_x > m_y$  like in the first type pre-adjustment. In other words the accuracy in height ( $Z$ ) is generally larger than the accuracy in the planimetry ( $X$  and  $Y$ ). Here the accuracy of  $Y$  is the smallest by reason of that this axis is related to the look angles which is important on the estimation of true ground coordinates (see Table 4.3). The effects of the EOP sets  $P_s$  and  $A$  both pre- and bundle-adjusted is in the Figure 4.16. The most important results achieved is that bundle adjustment has no advantage on the accuracies of both GCPs and ICPs. The accuracy of ICPs becomes worse with the increasing of their number from 10 to 40 where GCPs have almost equal accuracy for each point sets. Other results based on EOP sets from 13<sup>th</sup> and 19<sup>th</sup> are not shown since the accuracy of GCPs is extremely less.

The sets 5<sup>th</sup>, 6<sup>th</sup> and from 13<sup>th</sup> and 19<sup>th</sup> cause inaccurate results on the grouped points (G) as similar as in the homogenously distributed points (H). The higher accuracy on the GCPs is reached on the point set G-C whereas others have lower accuracy. The cause of these inaccurate results on G-A and G-C is based on the dependency of look angles with column number ( $y$ ) remembering the similar results achieved in the Table 4.3. The graphical representation of the accuracies of grouped point sets are not shown in Figure 4.16 since there is no any continuity among them.

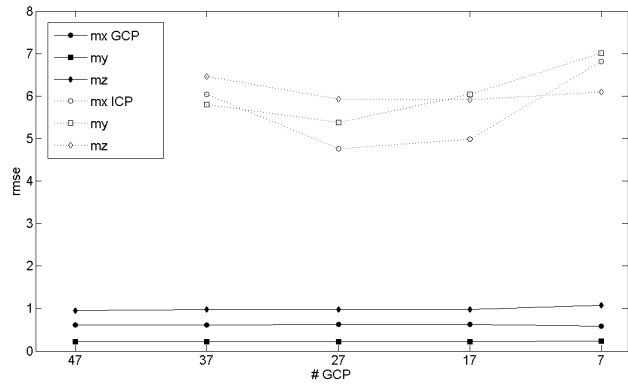
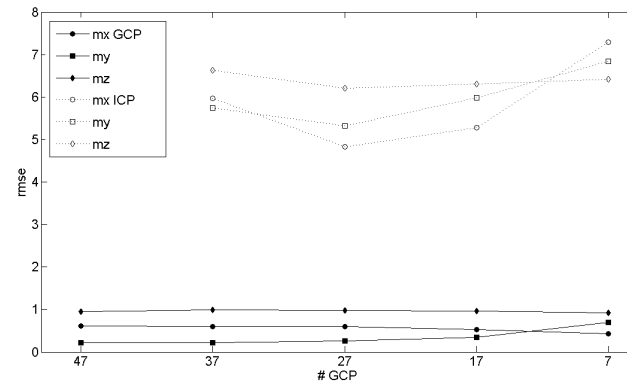
#### 4.4.3 Overview of Geometric Analysis

The geometric analysis is performed into two sections depending on the pre-adjustment of EOPs. In the first section only the look angles are pre-adjusted, and

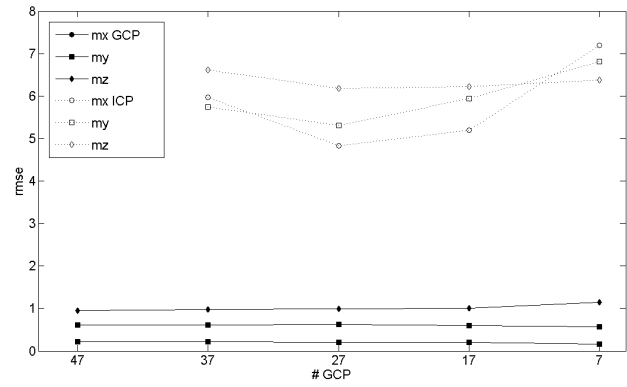




$P_s$



$A$



$B$

**Figure 4.16:** Graphical representation of accuracy of GCPs and ICPs in point sets  $P_s$  and  $A$  for the homogenous distributed points.  $\overline{LP}$  : pre-adjusted look angles and EOPs,  $B$ : bundle adjustment.

various EOPs are compensated in the bundle adjustment process. The effects of pre-adjusted EOPs are analysed in the second section.

The major domination on the getting accurate ground coordinates is based on the look angles. If the look angles are not pre- or bundle-adjusted, the estimated ground coordinates are extremely different compared to their true values. Usage of the pre-adjusted look angles assuming the EOPs constant overcomes this problem and the resulting the accuracy is sub-meter level and about  $\pm 1$  pixel ( $\pm 5$  m) for GCPs and ICPs respectively. The pre- or bundle-adjusted EOPs in all analysis do not improve the results. However the assuming of all EOPs as the adjustment parameter is not available since the possible high correlation among them. The EOPs from 1<sup>st</sup> to 12<sup>th</sup> excepting 5<sup>th</sup> and 6<sup>th</sup> provide accurate results where others cause unstable solutions.

The point distribution is the other subject to be examined. The accuracy of the GCPs and ICPs are similar in the point sets having homogenously distributed points. However if the GCPs or ICPs are located on one side of the image, the accuracy of ICPs becomes worse and the residual errors have systematic bias. This should be noted that the systematic effect is seen on the GCPs if the bundle adjustment is not applied.

## 5. CONCLUSION

Many imaging technologies and methods are developed for the wide range of applications. The linear array sensors, one of the imaging technologies, have many widespread usage on the geospatial applications. The geometry and the geometric accuracy provided by the image becomes important in this case. The questions can be “how the image has to be evaluated”, “which methods should be used”, and “whether auxiliary data is necessary” etc. Many answers for these questions can be found if previous studies and research are reviewed. However the main aim in this thesis is to geometrically analysis HRSIs based on linear array imaging technology using the parametric models and considering the orbital and attitude parameters of satellite.

Many parametric models are developed and have been presented. In this thesis the parametric model establishing the transformation from image to ground and vice versa is first presented in its generic form, and then its modification and simplification for the stereo SPOT-5 HRG level 1A images is explained. The generic model is cited from Weser *et al.* (2008) where the modified and simplified model is suggested by the SPOT Image (2002) and Fotev *et al.* (2005). Thus, this thesis does not claim and also not aim to generate a new parametric approach. The main motivation of this thesis is analysing the geometric accuracy of the images mentioned above, and strives to understand which component and parameter has to be considered to obtain accurate ground coordinates.

This section is continued into two parts. At first, both the pre- and bundle-adjustments, effects of look angles and EOPs are discussed, and then the further works are suggested.

### 5.1 Discussion of Thesis

The major correction is required for the look angles consisting the inner orientation of the used model in this thesis. If the EOPs, i.e. exterior orientation parameters, are assumed constant and the look angles are compensated in the pre-adjustment process,

the accuracies on GCPs and ICPs can be extremely improved. However, a systematic effect on the GCPs occurs with respect to the direction and the magnitude of their residual errors. The compensation of the EOPs in both pre- and bundle adjustment is not meaningful. Moreover, their various configurations produces inaccurate results on both the homogenously distributed and grouped point sets. On the other hand, the advantage of bundle adjustment has to be discussed. The bundle adjustment recovers the systematic residual errors on the GCPs. Nevertheless, it has no any significant advantage with respect to the accuracy.

The point distribution is the other important issue which has to be considered. The types of point sets are established into two. One of them is based on homogenous distribution decreasing the number of GCPs from 47 to 7 and increasing the number of ICPs from 10 to 40. The other sets include the located points on one side of the image. The point distribution is very important, since the accuracy of GCPs and ICPs are not significant for the homogenously distributed points. However the similar decision is not valid for the grouped points. If the GCPs lie on a whole line of the image similarly in G-B, its accuracy is higher than the others in comparison G-A and G-C. This reason can be explained by the look angles which are related to the line of image.

Finally the accuracy of GCPs are sub-meter level where ICPs have about  $\pm 1$  pixel ( $\pm 5$  meter). If the confidence interval is assumed as 99.7% ( $\pm 3\sigma$ ), the accuracy of ground coordinates of ICPs equal or smaller than  $\pm 3$  pixel ( $\sigma = \pm 1$  pixel) are statistically valid. It is interesting that this value (3 pixel) is the minimum required number of adjacent pixels for point determination (Srivastava *et al.*, 1996) on the images having high radiometric resolution. The radiometric resolution of the images investigated in this thesis, stereo SPOT-5 HRG level 1A panchromatic images, have 8 bits (256 grey values) radiometric resolution. This resolution was compared by the other linear array images (Topan *et al.*, 2009), and it is realized that its radiometric quality is sufficient for the point detection within 3 pixels. Thus, the results of this thesis can be scientifically acceptable.

## **5.2 Further Work**

Some further works can be suggested as following:

- The generic adjustment model, called collocation, includes the constraints between the adjustment parameters which is not considered in this thesis. So the functional model can be extended by the collocation, and the results can be compared with the results in this thesis.
- Many auxiliary interpolation and extrapolations, such as Lagrange or linear estimation, are preferred both in the pre-processing and the adjustment. The effects of these inevitable methods can be investigated.
- SPOT Image suggests and provides the transformation parameters between level 1A and 1B images. So the level 1B images can be back-projected and their accuracy can be investigated as similar as in this thesis.

Finally, the readers should take note the fact that the further aims can be varied by the many methods and many assumptions to investigate (or analyse) the images with or without high geometric resolution. Thus, much further research based on this scope can be performed. The needed is only the wish.



## REFERENCES

- BLASPO**, 2004: BLASPO User Guide, Institute of Photogrammetry and Geoinformation, Leibniz University Hannover, 2004.
- Baltsavias, E. P. and Stallmann, D.**, 1992, Metric information extraction from Spot images and the role of polynomial mapping functions, *International Archives of Photogrammetry and Remote Sensing*, Washington DC., USA, Vol. 29, Part B4, pp. 358 – 364.
- Baltsavias, E. P. and Stallmann, D.**, 2000, SPOT stereo matching for DTM generation, *Conference on Integrating Photogrammetric Techniques with Scene Analysis and Machine Vision*, 12-16 April, Orlando, USA. In Proceedings of SPIE, Vol. 1944, pp. 152 - 163.
- Büyüksalih, G.**, 2000. Doğrusal dizin (pushbroom) görüntüleme sistemleri, *Pamukkale Üniversitesi Mühendislik Bilimleri Dergisi*, sayı 6(2-3), s. 219-229.
- Büyüksalih, G., Oruç, M. and Jacobsen, K.**, 2004. Precise georeferencing of rectified high resolution space images, *International Archives of Photogrammetry, Remote Sensing and Spatial Information Sciences*, Vol. 35, Part B1, pp. 184-188.
- CORIKON**, 2003. CORIKON User Guide, Institute of Photogrammetry and Geoinformation, Leibniz University Hannover, 2003.
- Dowman, I. J. and Michalis, P.**, 2003. Generic rigorous model for along track stereo satellite sensors. *Joint Workshop of ISPRS/EARSeL High Resolution Mapping from Space 2003, Hannover, October. 6-8.*
- Fontannaz, D. and Begni, G.**, 2002, A new generation satellite: SPOT 5 in orbit, *ISPRS Highlights*, Vol. 7, No. 3, 30-31.
- Fotev, S., Georgiev, and Nedkov, N.R.**, 2005, Viewing Geometry Model Evaluation for Spaceborne Pushbroom Imagery, *2nd International Conference on Recent Advances in Space Technologies, Istanbul.* 540-544.
- Fritsch, D. and Stalman, D.**, 2000, Rigorous photogrammetric processing of high resolution satellite imagery, *International Archives of Photogrammetry, Remote Sensing and Spatial Information Sciences*, Amsterdam, Netherlands, 16–22 July, Vol. 33 (B1), pp. 313-321.

- Gleyzes, J. P., Meygret, A., Fratter, C., Panem, C., Baillarin, S. And Valorge, C.,** 2003, SPOT 5: system overview and image ground segment. *IEEE International Geoscience and Remote Sensing Symposium*, 21-25 July 2003, Toulouse, France.
- Gugan, D. J.,** 1987, Practical aspects of topographic mapping from SPOT imagery, *Photogrammetric Record*, 12(69): 349-355.
- Gupta, R. and Hartley, R. I.,** 1997. Linear pushbroom cameras, *IEEE Transactions on Pattern Analysis and Machine Intelligence*, September 1997, Vol. 19, No. 9.
- Jacobsen, K.,** 1998. Mapping with IRS-1C images, *ASPRS Annual Convention*, Tampa, USA.
- Jacobsen, K.,** 1999. Simple Solution of the special IRS-1C Pan-camera Problems, *Seminar In-orbit geometric characterization of optical imaging systems*, CNES, Bordeaux, France.
- Jacobsen, K.,** 2005. High resolution imaging satellite systems, *EARSeL 3D Remote Sensing Workshop*, Porto, Portugal, 9 p.
- Jacobsen, K., Büyüksalih, G. and Topan, H.,** 2005. Geometric models for the orientation of high resolution optical satellite sensors, *ISPRS Hannover Workshop 2005: High-Resolution Earth Imaging for Geospatial Information*, Hannover, Germany, 17-20 May.
- Jacobsen, K.,** 2006. Calibration of optical satellite sensors, *International Calibration and Orientation Workshop EuroCOW 2006*, Casteldefels, 6 p.
- Jacobsen, K.,** 2008, Geometric modelling of linear CCDs and panoramic imagers, (Eds) Li, Z., Chen, J. Baltsavias, E., *Advances in Photogrammetry, Remote Sensing and Spatial Information Science. Taylor and Francis*, UK, pp. 145-155
- Kim, T. and Im, Y.,** 2001. Automated DEM extraction from the KOMPSAT-1 EOC images, *22th Asian Conference on Remote Sensing*, Singapore, 5-9 November.
- Kim, S. and Kang, S.,** 2001: Automatic generation of a SPOT DEM: towards coastal disaster monitoring, *Korean Journal of Remote Sensing*, Vol.17, No.2, 2001, pp.121-129.
- Kim, T., Kim, H., and Rhee, S.,** 2007: Investigation of physical sensor models for modelling SPOT 3 orbits, *The Photogrammetric Record*, **22**(119), pp. 257-273.
- Konecny, G., Lohmann, P., Engel, H. and Kruck, E.,** 1987, Evaluation of SPOT imagery on analytical photogrammetric instruments, *Photogrammetric Engineering and Remote Sensing*, vol.53, No.9, pp.1223-1230.



- Kornus, W., Alamús, R., Ruiz, A. and Talaya, J.,** 2006, DEM generation from SPOT-5 3-fold along track stereoscopic imagery using autocalibration, *ISPRS Journal of Photogrammetry and Remote Sensing*, **60** (2006), pp. 147-159.
- Kraus, K.,** 1993, *Photogrammetry Volume I Fundamentals and Standard Processes*, Ferd. Dümmlers Verlag, Germany.
- Kratky, V.,** 1987, Rigorous Stereophotogrammetric Treatment of SPOT Images, *SPOT 1 Image Utilization, Assessment, Results*, Paris, November.
- Kratky, V.,** 1989, On-line aspects of stereophotogrammetric processing of SPOT images, *Photogrammetric Engineering and Remote Sensing*, vol.55, no.3, pp.311-316
- Latry, C. and Rougé B.,** 2003. Super resolution : quincunx sampling and fusion processing, *Proceedings of IEEE IGARSS '03*, Toulouse.
- Liedtke, J.,** 2002. QuickBird-2 system description and product overview, *JACIE Workshop*, Washington D.C., USA.
- Michalis, P.,** 2005. Generic rigorous model for along track stereo satellite sensors, *PhD Thesis*, Department of Geomatic Engineering, University Colloge London, UK.
- Orun, A. B.,** 1990, SPOT satellite imagery for topographic mapping, *M.Ph. Thesis*, Department of Civil Engineering, Oxford Polytechnic, UK.
- Orun, A. B. and Natarajan, K.,** 1994, A modified bundle adjustment software for SPOT imagery and photography: Tradeoff, *Photogrammetric Engineering and Remote Sensing*, Vol. 60, No. 12, December 1994, pp. 1431-1437.
- Poli, D., Seiz, G., Baltasvias, E. P.,** 2000. Cloud-top height estimation from satellite stereopairs for weather forecasting and climate change analysis. *International Archives of Photogrammetry, Remote Sensing and Spatial Information Sciences*, Amsterdam, Netherlands, 16–22 July, Vol. 33, Part B7/3, pp.1162-1169.
- Poli, D.,** 2002. General model for airborne and spaceborne linear array sensors, *International Archives of Photogrammetry, Remote Sensing and Spatial Information Sciences*, Denver, USA, 10–15 november, Vol. 33, Part B1, pp.177-182.
- Poli, D.,** 2003. Georeferencing of multi-line CCD array optical sensors with a general photogrammetric model, *International Geoscience and Remote Sensing Symposium*, Toulouse, France, 21-25 July.

- Poli, D.**, 2004., Orientation of satellite and airborne imagery from multi-line pushbroom sensors with a rigorous sensor model, *International Archives of Photogrammetry and Remote Sensing*, Vol. 35, Part B1, Istanbul, Turkey, pp.130-135.
- Poli, D.**, 2005. Modelling of space linear array sensors, *PhD Thesis*, ETHZ, Zürich, Switzerland, 203 p.
- Poli, D.**, 2007, A rigorous model for ppaceborne linear array sensors, *Photogrammetric Engineering and Remote Sensing*, Vol. 73, No. 2, pp. 187-196.
- Radhadevi, P.V., Ramanchandran, R. and Murali Mohan A.S.R.K.V.**, 1998. Restitution of IRS-1C PAN data using an orbit attitude model and minimum control, *ISPRS Journal of Photogrammetry and Remote Sensing*, 53(5), pp. 262–271.
- Richards, J. A. and Jia X.**, 1999. Remote Sensing Digital Image Analysis, *Springer*, Australia.
- Salamonowicz, P. H.**, 1986. Satellite orientation and position for geometric correction of scanner imagery, *Photogrammetric Engineering and Remote Sensing*, Vol.52, No. 4, pp.491-499.
- Schröder, M., Mooshuber, W., Müller, R., Reinartz, P.**, 2001. Resolution tests with a TDI – camera, *Joint Workshops of ISPRS Working Groups I/2, I/5 and IV/7 High Resolution Mapping from Space 2001*, Hannover, Germany, 19-21 September.
- Seeber, G.**, 1993. Satellite Geodesy, *de Gruyter*, Germany.
- SPOT Image**, 2002. SPOT Satellite Geometry Handbook, Reference S-NT-73-12-SI, Edition 1, Revision 0, Date 2002-01-15.
- Srivastava, P. K., Gopala Krishna, B., Majumder, K. L.**, 1996. Cartography and terrain mapping using IRS-1C data, *National Natural Resources Management System, Current Science*, Vol. 70, No. 7.
- Topan, H.**, 2004. Yörünge düzeltmeli IRS-1C/1D pankromatik mono görüntüsünün geometrik doğruluk ve bilgi içeriği açısından incelenmesi, *Msc. Thesis*, ZKU Institute of Natural and Applied Sciences, 77 pgs.
- Topan, H., Büyüksalih, G. and Jacobsen, K.**, 2006. Information content of high-resolution satellite image: mapping with OrbView-3 images, *GIM International*, Volume 20, Issue 12.
- Topan, H. and Kutoglu, H.**, 2009, Georeferencing accuracy assessment of high resolution satellite images using figure condition method, *IEEE Transactions on Geoscience and Remote Sensing*, Volume 47, Issue 4: 1256-1261

- Topan, H., Maktav, D., Jacobsen, K., and Büyüksalih, G.**, 2009, Information content of optical satellite images for topographic mapping, *International Journal of Remote Sensing*, Volume 30, Issue 7: 1819-1827.
- Toutin, T.**, 2003a. Geometric correction of remotely sensed images, in *Remote Sensing of Forest Environments: Concepts and Case Studies*, M. A. Wulder and S. E. Franklin Editors, Kluwer Academic Publishers, 2003, Chapter 6, pp. 143-180.
- Toutin, T.**, 2003b. Error tracking in IKONOS geometric processing using a 3D parametric model, *Photogrammetric Engineering & Remote Sensing*, Vol. 69, No. 1, pp. 43-51.
- Weser, T., Rottensteiner, F., Willneff, J., Poon, J., and Fraser, C.**, 2008. Development and testing of a generic sensor model for pushbroom satellite imagery, *The Photogrammetric Record*, **23**(123), pp. 255-274.
- Westin, T.**, 1990. Precision rectification of SPOT imagery, *Photogrammetric Engineering & Remote Sensing*, Vol 56, No. 2, pp. 247-253.
- Westin, T. and Forsgren, J.**, 2001. Orthorectification of EROS A1 images, *IEEE/ISPRS Joint Workshop On Remote Sensing And Data Fusion Over Urban Areas*, 8-9 November, Rome.
- Wikipedia**, 2007. Charge-Coupled Device, [http://en.wikipedia.org/wiki/Charge-coupled\\_device](http://en.wikipedia.org/wiki/Charge-coupled_device), last visit: 24th Marc 2007.
- Yamakawa, T.**, 2004. Linear Orientation Models for High-Resolution Satellite Line Scanner Imagery, *Ph.D. Thesis*, The University of Melbourne, Department of Geomatics, Melbourne, Australia, 191 p.
- Zoej, M. J. V.**, 1997. Photogrammetric evaluation of space linear array imagery for medium scale topographic mapping, *Ph.D. Thesis*, University of Glasgow, Faculty of Science, Glasgow, United Kingdom, 303 p.
- Zoej, M. J. V. and Petrie, G.**, 1998. Mathematical modelling and accuracy Testing of SPOT Level 1B Stereopairs, *Photogrammetric Record*, 16 (919), pp. 67-82.
- Zoej, M. J. V. and Foomani, M. J.**, 1999. Mathematical Modelling and Geometric Accuracy Testing of IRS-1C Stereo Pairs, *Joint Workshop of ISPRS WG I/1, I/3 and IV/4 Sensors and Mapping from Space, Hannover*.
- Zoej, M. J. V. and Sadeghian, S.**, 2003. Rigorous and Non-Rigorous Photogrammetric Processing of Ikonos Geo Image, *Joint Workshop of ISPRS/EARSeL High Resolution Mapping from Space, Hannover*.



## **APPENDICES**

**APPENDIX A.1** : Symbols

**APPENDIX A.2** : Coordinate Systems

**APPENDIX A.3** : Rotation Around 3D Coordinate Systems

**APPENDIX A.4** : Ground Coordinate Estimation from Stereo Images

**APPENDIX A.5** : Results of Geometric Analysis



## APPENDIX A.1: Symbols\*

$a_r, a_p, a_y$	: roll, pitch, yaw, respectively.
$\underline{A}$	: Design matrix of unknowns
$\underline{B}$	: Design matrix of residuals
$c$	: Focal length
$\vec{c}$	: vector consisting exterior orientation parameters
$C_M$	: Camera mounting parameter
$\underline{dP}$	: Unknown vector
$f$	: True anomaly
$F$	: Function
$g$	: number of position and velocity of satellite
$H$	: Flying height
$inc$	: Orbital inclination
$\underline{l}$	: Absolute term vector
$L$	: Observation
$m$	: Scale factor
$m$	: Number of images
$n$	: Number of points
$N$	: Ascending node
$N'$	: Descending node
$N_c$	: Number of column
$N_r$	: Number of row
$O$	: Centre of Earth
$p$	: Pixel size ( $p_x, p_y$ in $x$ and $y$ direction, respectively)
$P$	: Perigee
$\vec{P}$	: Position vector in GCS
$P_{j,i}$	: One of the parameters of the line $i$ ( $j=1(1)30$ )
$\vec{p}_c$	: Position vector in CCS
$\vec{p}_0$	: Position vector in OCS
$\vec{p}_p$	: Position vector in PCS

---

\* Symbols used in alphabetic order. The specific symbols used by other researches (e.g. in Section 3.2.2) are ignored.

$\vec{p}_s$	: Position vector in SCS
$\vec{P}_s$	: Satellite position vector
$P_0$	: Exterior orientation parameter for the reference line
$\dot{P}$	: Drift
$\ddot{P}$	: Drift rates,
$psg_x$	: Pixel size on ground in the direction of motion (x)
$psg_y$	: Pixel size on ground in the perpendicular direction to the motion (y)
$r$	: Geocentric distance to the satellite
$r$	: Elements of $R$
$R$	: Rotation matrix around related axis in a right-hand coordinate system
$S$	: Satellite
$t$	: Time
$t_0$	: Acquisition time for reference line
$v$	: Residual,
$V$	: Velocity of satellite/platform
$\vec{V}_s$	: Satellite velocity vector
$w_p$	: Argument of perigee
$w$	: Misclosure
$x, y$	: Image coordinates
$x_0, y_0$	: Image coordinates of principal point
$x_s, y_s$	: Scanline coordinates
$X, Y, Z$	: Ground/object coordinates
$X_0, Y_0, Z_0$	: Ground/object coordinates of perspective center
$\Delta t$	: Time interval
$\Omega$	: Right ascension of the ascending node
$\theta_{GR}$	: Greenwich Mean Sidereal Time
$\omega, \varphi, \kappa$	: rotation angles around $X, Y$ and $Z$ axis, respectively
$\gamma$	: First point of aries
$\vec{\delta x}$	: vector of systematic error corrections
$\pi$	: Pi constant
$\psi_x$	: Look angle in $x$ direction



$\psi_y$  : Look angle in  $y$  direction

$|_0$  : Initial value of parameters

$\| \|$  : Norm of vector



## APPENDIX A.2: Coordinate Systems

A generic model establishes a geometric relationship between image and ground coordinate systems which the points are measured on both. However, the real relationship is established among the auxiliary coordinate systems. All required coordinate systems are:

1. Image coordinate system (ICS)
2. Scanline coordinate system (SCS)
3. Camera coordinate system (CCS)
4. Payload coordinate system (PCS)
5. Orbit coordinate system (OPS), and
6. Ground coordinate system (GCS)

### Image coordinate system

Image coordinate system is a 2D coordinate system. Its origin is at the centre of left-top pixel, and the position is defined by row ( $x$ ) and column ( $y$ ) number in pixel unit (Figure A.2.1). The image dimensions are described by total number of rows ( $N_r$ ) and of columns ( $N_c$ ). Both axis are perpendicular to each other.

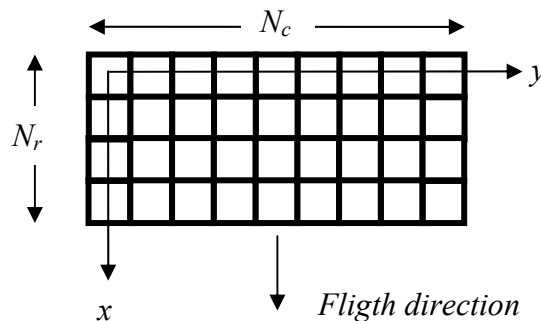


**Figure A.2.1:** Image coordinate system.

### Scanline coordinate system

In the case of imaging using linear array sensors, each sensor has its own coordinate system called as scanline coordinate system with its origin is leftmost pixel of the corresponding line (Figure A.2.2).  $x_s$  is related to the acquisition time of line and always equals to zero. Both axes are perpendicular to each other (Poli, 2005).  $N_c$  refers number of elements in each line.

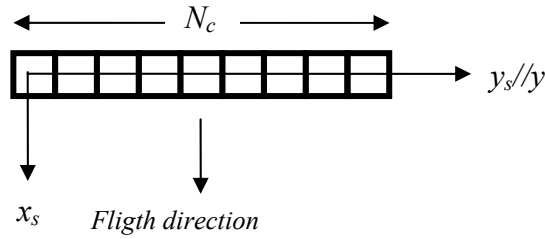


**Figure A.2.2:** Scanline coordinate system.

In an ideal case without lens distortions and geometric errors in the CCD line, the  $y_s$  in meter can be calculated by the image coordinate  $y$  as following:

$$y_s = y \cdot p_y \tag{A.2.1}$$

### Camera coordinate system

Camera coordinate system is a 3D right-hand coordinate system. Its origin is at the projection center, with the  $y_c$  axis being along the  $y_s$ , and the  $z_c$  axis being orthogonal to the focal plane (Figure B.3).

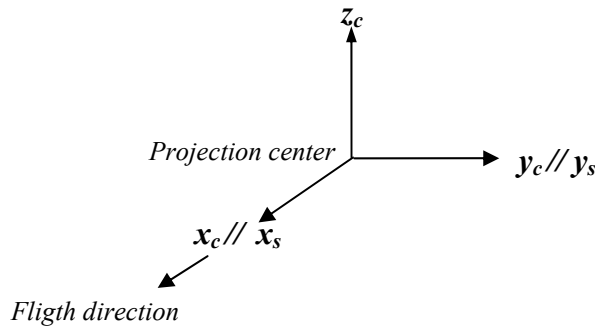


**Figure A.2.3:** Camera coordinate system.

### Payload coordinate system

Payload coordinate system, a 3D right-hand coordinate system, is fixed to the payload. Its origin is payload's mass center. The transformation from this coordinate system to orbital coordinate system is a time-dependent rotation parameterised by the three attitude angles ( $a_r, a_p, a_y$ ) around  $x, y$  and  $z$  axes, respectively.

### Orbital coordinate system

Orbital coordinate system, a 3D right-hand coordinate system, is fixed to the payload. Its origin is payload's mass center, with the  $x_o$  axis being close to mean flight direction,  $x_o z_o$  plane is on the orbital plane and  $y_o$  axis completes a right-hand

coordinate system (Figure A.2.4). The transformation from this to ground coordinate system is a time-dependent rotation performed by Keplerian angular elements and GMST, or position and velocity vectors of satellite.

### Ground coordinate system

The ground coordinate system corresponds Conventional Terrestrial Coordinate System (CTCS) in this thesis since the GCPs and satellite position vector are defined in this coordinate system. CTCS is a geocentric system that its origin is at the centre of Earth.  $Z$  axis points to the conventional origin which is defined as the mean position of the instantaneous pole during the period 1900 to 1905. The  $XZ$  plane contains the mean Greenwich Observatory and  $Y$  axis completes a right-hand coordinate system (Zoej, 1997).

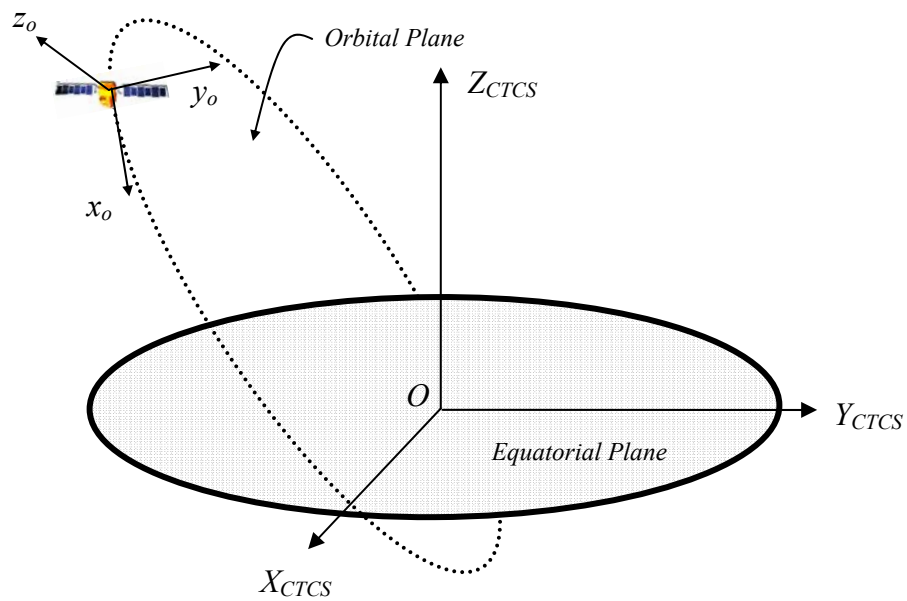


**Figure A.2.4:** Orbital and ground coordinate systems.



### APPENDIX A.3: Rotation Around 3D Coordinate Systems

Rotation around the  $j$  axis in a right-hand coordinate system illustrated in Figure A.3.1. can be written in a matrix form as followings:

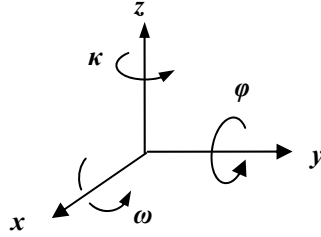


**Figure A.3.1.** Contraclockwise rotations.

$j$	<b>Contraclockwise</b>	<b>Clockwise</b>
$x$	$R_x = \begin{bmatrix} 1 & 0 & 0 \\ 0 & \cos \omega & -\sin \omega \\ 0 & \sin \omega & \cos \omega \end{bmatrix}$	$R_x^{-1} = \begin{bmatrix} 1 & 0 & 0 \\ 0 & \cos \omega & \sin \omega \\ 0 & -\sin \omega & \cos \omega \end{bmatrix}$
$y$	$R_y = \begin{bmatrix} \cos \varphi & 0 & \sin \varphi \\ 0 & 1 & 0 \\ -\sin \varphi & 0 & \cos \varphi \end{bmatrix}$	$R_y^{-1} = \begin{bmatrix} \cos \varphi & 0 & -\sin \varphi \\ 0 & 1 & 0 \\ \sin \varphi & 0 & \cos \varphi \end{bmatrix}$
$z$	$R_z = \begin{bmatrix} \cos \kappa & -\sin \kappa & 0 \\ \sin \kappa & \cos \kappa & 0 \\ 0 & 0 & 1 \end{bmatrix}$	$R_z^{-1} = \begin{bmatrix} \cos \kappa & \sin \kappa & 0 \\ -\sin \kappa & \cos \kappa & 0 \\ 0 & 0 & 1 \end{bmatrix}$

The clockwise rotation is inverse or transpose of contraclockwise rotation matrix since the rotation matrix is orthogonal.

#### **Elements of Matrix $R_{PO}$**

$R$  is the final matrix to transform PCS into GCS. Step by step matrix calculation and elements of both auxiliary and final matrix are summarized. Matrix  $R_{PO}$  is calculated as following:

	$R_Z(a_y) = \begin{bmatrix} \cos(a_y) & \sin(a_y) & 0 \\ -\sin(a_y) & \cos(a_y) & 0 \\ 0 & 0 & 1 \end{bmatrix}$
$R_Y(a_p) = \begin{bmatrix} \cos(a_p) & 0 & -\sin(a_p) \\ 0 & 1 & 0 \\ \sin(a_p) & 0 & \cos(a_p) \end{bmatrix}$	$R_Y(\text{pitch})R_Z(\text{yaw})$
$R_X(a_r) = \begin{bmatrix} 1 & 0 & 0 \\ 0 & \cos(a_r) & \sin(a_r) \\ 0 & -\sin(a_r) & \cos(a_r) \end{bmatrix}$	$R_{OP}$

Elements of matrix  $R_{OP}$  become:

$$\begin{aligned}
R_{1,1}^{OP} &= \cos(a_p) \cdot \cos(a_y) \\
R_{1,2}^{OP} &= -\cos(a_p) \cdot \sin(a_y) \\
R_{1,3}^{OP} &= \sin(a_p) \\
R_{2,1}^{OP} &= \cos(a_r) \cdot \sin(a_y) + \sin(w) \cdot \sin(a_p) \cdot \cos(a_y) \\
R_{2,2}^{OP} &= \cos(a_y) \cdot \cos(w) - \sin(a_y) \cdot \sin(a_p) \cdot \sin(w) \\
R_{2,3}^{OP} &= -\cos(a_p) \cdot \sin(w) \\
R_{3,1}^{OP} &= \sin(a_r) \cdot \sin(a_y) - \cos(a_r) \cdot \sin(a_p) \cdot \cos(a_y) \\
R_{3,2}^{OP} &= \sin(a_y) \cdot \sin(a_p) \cdot \cos(a_r) + \cos(a_y) \cdot \sin(a_r) \\
R_{3,3}^{OP} &= \cos(a_p) \cdot \cos(a_r)
\end{aligned} \tag{A.3.1}$$

### Elements of Matrix $R_{OG}$

Matrix  $R_{OG}$  can be established by two ways. The first way is performed by the angular Keplerian elements ( $f$ ,  $w_p$ ,  $\Omega$  and  $inc$ ) shown in Figure A.3.2 and Greenwich Mean Sidereal Time ( $\theta_{GR}$ ), the angle between CICS and GCS around  $Z$  axis. The second and easier way is performed by the position ( $\vec{P}_s$ ) and velocity ( $\vec{V}_s$ ) vectors of satellite.

In the first way, the Keplerian elements can be estimated as following:



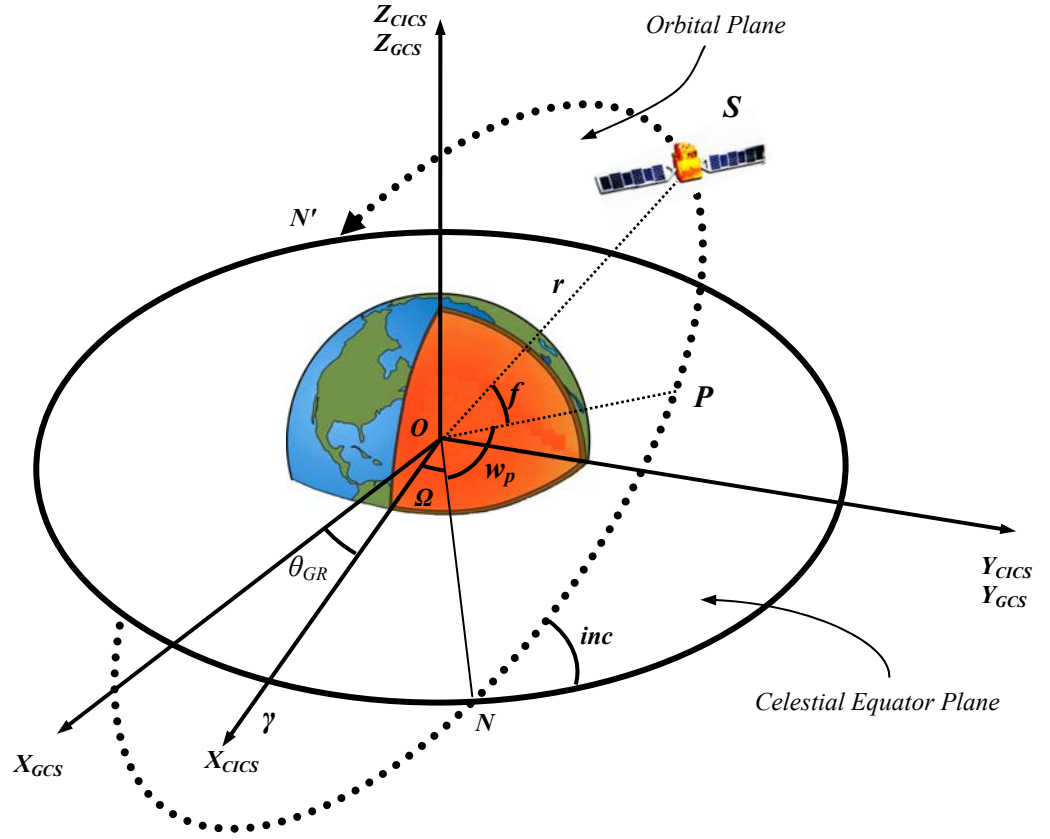


**Figure A.3.2:** Keplerian elements in CICS and GCS.

$$\vec{C} = \vec{P}_s \times \vec{V}_s = \begin{bmatrix} C_X \\ C_Y \\ C_Z \end{bmatrix} \quad (\text{A.3.2})$$

$$C = \|\vec{C}\| \quad (\text{A.3.3})$$

$$r = \|\vec{P}_s\| \quad (\text{A.3.4})$$

$$inc = \arccos\left(\frac{C_Z}{C}\right) \quad (\text{A.3.5})$$

$$\Omega = \arctan\left(\frac{C_X}{C_Y}\right) \quad (\text{A.3.6})$$

$$f + w_p = \arcsin\left(\frac{Z_s}{r \cdot \sin(inc)}\right) \quad (\text{A.3.7})$$

where  $\times$  = cross product, and  $\|\cdot\|$  = norm of the vector.

Matrix  $R_{OG}$  is calculated as following:

	$R_Z(\pi - (\Omega - \theta_{GR})) =$ $\begin{bmatrix} -\cos(\Omega - \theta_{GR}) & \sin(\Omega - \theta_{GR}) & 0 \\ -\sin(\Omega - \theta_{GR}) & -\cos(\Omega - \theta_{GR}) & 0 \\ 0 & 0 & 1 \end{bmatrix}$
$R_X\left(\frac{\pi}{2} - inc\right) =$ $\begin{bmatrix} 1 & 0 & 0 \\ 0 & \sin(inc) & -\cos(inc) \\ 0 & \cos(inc) & \sin(inc) \end{bmatrix}$	$R_X\left(\frac{\pi}{2} - inc\right)R_Z(\pi - (\Omega - \theta_{GR}))$
$R_Y\left(\frac{\pi}{2} - (f + w_p)\right) =$ $\begin{bmatrix} \sin(f + w_p) & 0 & -\cos(f + w_p) \\ 0 & 1 & 0 \\ \cos(f + w_p) & 0 & \sin(f + w_p) \end{bmatrix}$	$R_{OG}$

Elements of matrix  $R_{OG}$  becomes:

$$\begin{aligned}
R_{1,1}^{OG} &= -\cos(\Omega - \theta_{GR})\sin(f + w_p) - \sin(\Omega - \theta_{GR})\cos(inc)\cos(f + w_p) \\
R_{1,2}^{OG} &= \sin(\Omega - \theta_{GR})\sin(inc) \\
R_{1,3}^{OG} &= \cos(\Omega - \theta_{GR})\cos(f + w_p) - \sin(\Omega - \theta_{GR})\cos(inc)\sin(f + w_p) \\
R_{2,1}^{OG} &= -\sin(\Omega - \theta_{GR})\sin(f + w_p) + \cos(\Omega - \theta_{GR})\cos(inc)\cos(f + w_p) \\
R_{2,2}^{OG} &= -\cos(\Omega - \theta_{GR})\sin(inc) \\
R_{2,3}^{OG} &= \sin(\Omega - \theta_{GR})\cos(f + w_p) + \cos(\Omega - \theta_{GR})\cos(inc)\sin(f + w_p) \\
R_{3,1}^{OG} &= \sin(inc)\cos(f + w_p) \\
R_{3,2}^{OG} &= \cos(inc) \\
R_{3,3}^{OG} &= \sin(inc)\sin(f + w_p)
\end{aligned} \tag{A.3.8}$$

where  $inc$  is the orbital inclination,  $\Omega$  is right ascension of the ascending node,  $f$  is true anomaly,  $w_p$  argument of perigee,  $\theta_{GR}$  is Greenwich Mean Sidereal Time.

In the second way, using  $\vec{P}_S$  and  $\vec{V}_S$  elements of  $R_{OG}$  becomes:

$$\begin{bmatrix} R_{3,1}^{OG} \\ R_{3,2}^{OG} \\ R_{3,3}^{OG} \end{bmatrix} = \frac{\vec{P}_S}{\|\vec{P}_S\|} \tag{A.3.9}$$

$$\begin{bmatrix} R_{2,1}^{OG} \\ R_{2,2}^{OG} \\ R_{2,3}^{OG} \end{bmatrix} = \frac{\begin{bmatrix} R_{3,1}^{OG} \\ R_{3,2}^{OG} \\ R_{3,3}^{OG} \end{bmatrix} \times \vec{V}_s}{\left\| \begin{bmatrix} R_{3,1}^{OG} \\ R_{3,2}^{OG} \\ R_{3,3}^{OG} \end{bmatrix} \times \vec{V}_s \right\|} \quad (\text{A.3.10})$$

$$\begin{bmatrix} R_{1,1}^{OG} \\ R_{1,2}^{OG} \\ R_{1,3}^{OG} \end{bmatrix} = \frac{\begin{bmatrix} R_{2,1}^{OG} \\ R_{2,2}^{OG} \\ R_{2,3}^{OG} \end{bmatrix} \times \begin{bmatrix} R_{3,1}^{OG} \\ R_{3,2}^{OG} \\ R_{3,3}^{OG} \end{bmatrix}}{\left\| \begin{bmatrix} R_{2,1}^{OG} \\ R_{2,2}^{OG} \\ R_{2,3}^{OG} \end{bmatrix} \times \begin{bmatrix} R_{3,1}^{OG} \\ R_{3,2}^{OG} \\ R_{3,3}^{OG} \end{bmatrix} \right\|} \quad (\text{A.3.11})$$



### Appendix A.4: Ground Coordinate Estimation from Stereo Images

The ground coordinates of a point can be intersected from at least two stereo images (Figure A.4.1).

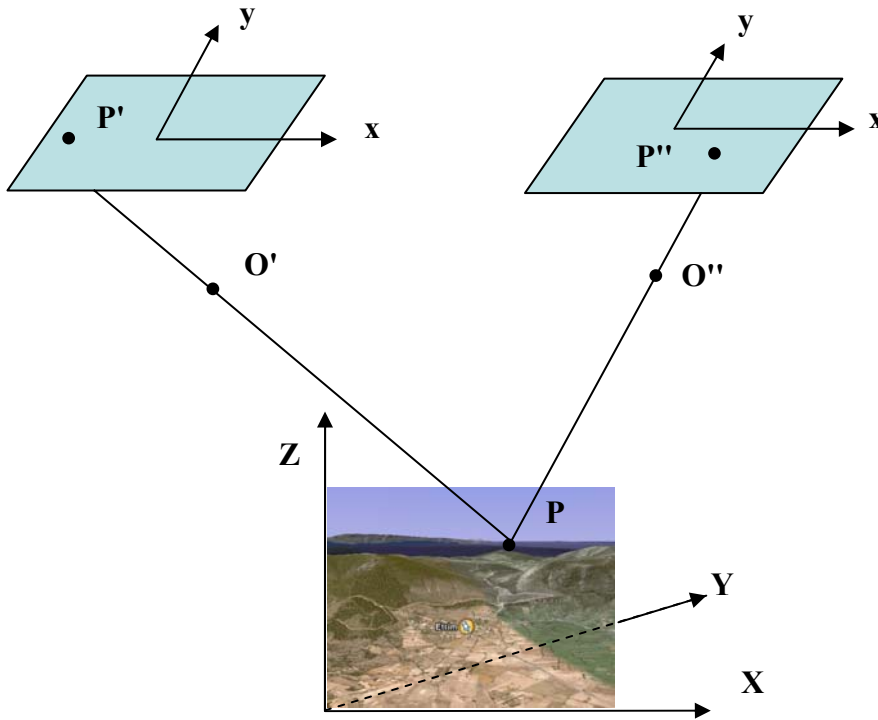


**Figure A.4.1:** Point intersection from stereo images.

The ground coordinates can be estimated by the mathematical model derived from the colinearity equations as following:

$$\begin{bmatrix} X \\ Y \\ Z \end{bmatrix} = \begin{bmatrix} X_0 \\ Y_0 \\ Z_0 \end{bmatrix} + m \underline{R} \begin{bmatrix} x - x_o \\ y - y_o \\ -c \end{bmatrix} \quad (\text{A.4.1})$$

Since the ground coordinates of a point has to be equal from the derivation of both images, the following equation can be written:

$$\begin{bmatrix} X \\ Y \\ Z \end{bmatrix} = \begin{bmatrix} X_0 \\ Y_0 \\ Z_0 \end{bmatrix}_1 + m_1 \underline{R}_1 \begin{bmatrix} x - x_o \\ y - y_o \\ -c \end{bmatrix}_1 = \begin{bmatrix} X_0 \\ Y_0 \\ Z_0 \end{bmatrix}_2 + m_2 \underline{R}_2 \begin{bmatrix} x - x_o \\ y - y_o \\ -c \end{bmatrix}_2 \quad (\text{A.4.2})$$

It yields the system in matrix notation that:

$$\begin{bmatrix} \underline{R}_1 \begin{bmatrix} x-x_o \\ y-y_o \\ -c \end{bmatrix}_1 & -\underline{R}_2 \begin{bmatrix} x-x_o \\ y-y_o \\ -c \end{bmatrix}_2 \end{bmatrix} \cdot \begin{bmatrix} m_1 \\ m_2 \end{bmatrix} = \begin{bmatrix} \begin{bmatrix} X_0 \\ Y_0 \\ Z_0 \end{bmatrix}_2 & -\begin{bmatrix} X_0 \\ Y_0 \\ Z_0 \end{bmatrix}_1 \end{bmatrix} \quad (\text{A.4.3})$$

$$\underline{A} \cdot \underline{m} = \underline{b} \quad (\text{A.4.4})$$

$$\underline{m} = (\underline{A}^T \underline{A})^{-1} \underline{A}^T \underline{b} \quad (\text{A.4.5})$$

Replacing these scales ( $m_1$  and  $m_2$ ) the ground coordinates of a point can be estimated in equation A.4.1.

**Appendix A.5.1. Results based on first type pre-adjustment**

Point	set	H-0	H-10		H-20		H-30		H-40		G-A		G-B		G-C	
	type	GCP	GCP	ICP	GCP	ICP	GCP	ICP	GCP	ICP	GCP	ICP	GCP	ICP	GCP	ICP
EOP	#	47	37	10	27	20	17	30	7	40	23	24	24	23	17	30
1. P <sub>S</sub>	$m_X$	0.597	0.596	5.979	0.592	4.838	0.515	5.284	0.427	7.293	11.454	20.291	0.686	15.140	39.595	109.251
	$m_Y$	0.215	0.221	5.743	0.265	5.325	0.343	5.982	0.696	6.838	8.953	16.239	0.829	15.683	24.061	88.602
	$m_Z$	0.943	0.978	6.622	0.965	6.199	0.947	6.295	0.919	6.397	12.699	14.102	1.012	9.242	42.480	96.538
2. P <sub>S0</sub>	$m_X$	0.597	0.595	5.976	0.587	4.846	0.532	5.284	0.487	7.128	5.685	12.244	0.602	4.989	8.962	10.880
	$m_Y$	0.215	0.208	5.739	0.191	5.323	0.200	5.981	0.699	6.672	9.426	19.381	0.342	5.727	15.136	32.999
	$m_Z$	0.943	0.972	6.610	0.947	6.176	0.924	6.246	0.455	6.412	7.261	21.801	1.028	10.720	11.264	21.426
3. P <sub>S1</sub>	$m_X$	0.606	0.601	5.971	0.616	4.828	0.595	5.210	1.211	7.309	4.659	18.626	0.875	4.940	6.621	21.072
	$m_Y$	0.213	0.225	5.749	0.227	5.313	0.236	5.940	0.920	6.704	10.236	19.621	0.648	5.620	12.590	40.075
	$m_Z$	0.950	0.971	6.612	0.960	6.181	0.950	6.231	1.937	6.048	6.100	28.842	1.292	10.926	7.578	22.468
4. P <sub>S2</sub>	$m_X$	0.599	0.599	5.972	0.613	4.835	0.591	5.234	0.589	7.160	5.637	21.670	0.634	4.990	5.808	20.886
	$m_Y$	0.215	0.223	5.742	0.219	5.310	0.232	5.945	0.630	6.786	11.725	21.277	0.542	5.580	10.105	43.183
	$m_Z$	0.944	0.965	6.608	0.949	6.173	0.932	6.219	0.686	6.382	7.377	36.448	1.052	11.047	6.976	16.473
5. V <sub>S</sub>	$m_X$	0.735	939489.984	5.971	857488.941	4.819	1426273.558	5.167	925835.426	6.855	2788377.306	24.144	0.394	5.296	1223649.079	69.468
	$m_Y$	0.181	1193598.058	5.743	601294.331	5.305	1748692.408	5.907	578400.232	6.804	1392198.459	32.283	0.348	5.298	941124.562	50.211
	$m_Z$	1.091	1058066.953	6.601	881630.195	6.175	1617679.447	6.217	955731.588	6.777	2736008.555	9.318	1.229	12.913	1284129.062	88.309
6. V <sub>0</sub>	$m_X$	0.637	0.371	5.972	1.873	4.819	6.360	5.170	14.250	7.218	1489.062	29.475	77.553	5.235	7173.940	42.218
	$m_Y$	0.205	0.415	5.738	0.625	5.337	3.025	5.999	3.631	6.856	526.387	31.650	46.626	5.756	1597.374	55.948
	$m_Z$	0.986	0.641	6.603	2.388	6.169	7.097	6.237	15.892	6.483	1460.937	6.132	79.687	9.686	6894.834	11.020
7. V <sub>1</sub>	$m_X$	0.602	0.603	5.972	0.614	4.828	0.579	5.207	0.614	7.169	0.825	26.239	0.518	5.290	1.230	34.041
	$m_Y$	0.214	0.221	5.742	0.229	5.310	0.252	5.937	0.218	6.825	0.393	32.862	0.167	5.930	0.371	54.108
	$m_Z$	0.948	0.980	6.609	0.991	6.180	1.034	6.232	1.404	6.367	0.833	7.491	1.051	10.061	2.793	10.958
8. V <sub>2</sub>	$m_X$	0.613	0.614	5.971	0.630	4.826	0.594	5.207	0.574	7.188	0.714	26.023	0.513	5.474	1.762	33.091
	$m_Y$	0.211	0.223	5.744	0.229	5.311	0.240	5.938	0.116	6.811	0.228	32.900	0.221	5.931	0.315	54.086
	$m_Z$	0.960	0.984	6.609	0.986	6.174	1.022	6.223	1.402	6.375	0.868	7.147	1.045	10.378	1.408	9.203
9. A	$m_X$	0.601	0.600	5.971	0.621	4.827	0.587	5.200	0.564	7.183	0.645	23.024	0.584	5.246	2.011	26.994
	$m_Y$	0.214	0.215	5.743	0.208	5.309	0.203	5.935	0.164	6.825	0.399	32.445	0.221	5.678	0.509	48.639
	$m_Z$	0.946	0.974	6.607	0.980	6.172	0.992	6.216	1.134	6.327	0.975	5.146	1.076	7.012	2.723	63.261
10. A <sub>0</sub>	$m_X$	0.601	0.600	5.970	0.617	4.824	0.589	5.199	0.605	7.185	0.451	25.632	0.473	5.271	0.441	30.178
	$m_Y$	0.214	0.218	5.744	0.215	5.309	0.211	5.935	0.121	6.824	0.432	32.788	0.268	5.882	0.558	53.995
	$m_Z$	0.946	0.972	6.605	0.968	6.169	0.969	6.213	1.092	6.319	0.623	6.907	0.974	10.040	0.478	6.756
11. A <sub>1</sub>	$m_X$	0.601	0.604	5.971	0.623	4.828	0.597	5.209	0.654	7.166	1.076	24.397	0.494	5.196	1.384	29.259
	$m_Y$	0.214	0.222	5.743	0.222	5.310	0.228	5.937	0.235	6.811	0.307	32.520	0.164	5.869	0.337	53.713
	$m_Z$	0.947	0.975	6.610	0.971	6.178	0.983	6.227	1.270	6.333	1.331	5.738	1.077	9.881	1.252	7.381
12. A <sub>2</sub>	$m_X$	0.601	0.606	5.971	0.623	4.828	0.593	5.208	0.637	7.210	0.611	24.741	0.510	5.208	0.846	29.259
	$m_Y$	0.214	0.220	5.743	0.223	5.310	0.230	5.936	0.115	6.817	0.412	32.565	0.238	5.871	0.543	53.713
	$m_Z$	0.946	0.970	6.609	0.963	6.171	0.966	6.216	1.044	6.329	1.110	6.010	0.970	9.857	0.849	7.381
13. P <sub>S</sub> V <sub>S</sub>	$m_X$	94.687	3363754.206	5.993	2480619.438	4.850	3299827.426	5.415	1194847.286	46.426	2214311.619	19.880	35111.533	14.855	94018.431	405.849
	$m_Y$	25.882	2038666.201	5.690	1358110.296	5.314	2058852.485	5.954	868950.819	39.492	667503.266	28.373	25961.300	24.132	53648.759	351.632
	$m_Z$	91.547	3371220.737	6.579	2457473.719	6.147	3315454.877	6.513	1239793.430	46.702	2135298.602	7.112	36660.399	20.767	95661.648	432.227
14. (P <sub>S</sub> V) <sub>0</sub>	$m_X$	0.331	614.359	5.976	1540.174	4.835	4310.204	5.231	82961.642	7.521	15111.947	25.055	1033.349	5.257	156780.579	28.222
	$m_Y$	0.332	189.215	5.750	418.697	5.319	1157.833	5.948	24295.106	6.924	7559.826	32.487	288.964	5.907	90957.713	52.399
	$m_Z$	0.454	597.950	6.604	1490.247	6.166	4165.599	6.222	80604.260	6.493	15147.503	7.293	995.090	9.823	160271.802	7.026
15. P <sub>S</sub> A	$m_X$	6.614	93.776	5.977	86.367	4.817	949.367	5.014	461575.423	220.047	6967.113	16.205	1476.484	51.142	24930.954	77.463
	$m_Y$	2.311	81.840	5.743	423.180	5.298	647.874	5.942	330422.466	89.154	10035.801	12.922	802.246	30.264	18424.392	52.487
	$m_Z$	6.196	65.991	6.595	178.262	6.132	598.511	5.963	423234.552	241.121	6705.377	19.952	916.408	62.691	7794.052	109.205
16. (P <sub>S</sub> A) <sub>0</sub>	$m_X$	1.762	16.701	5.971	42.951	4.814	85.024	5.178	157.044	7.171	1253.439	27.873	93.470	5.195	1882.853	28.279
	$m_Y$	0.852	37.442	5.739	169.735	5.319	304.137	5.982	457.906	6.885	250.475	31.354	551.640	5.837	673.271	52.796
	$m_Z$	1.814	14.821	6.601	63.885	6.150	124.554	6.186	326.735	6.329	343.224	6.602	245.020	10.208	1359.740	7.005
17. V <sub>S</sub> A	$m_X$	437352.820	2677225.250	5.986	1710947.167	4.855	1855043.749	5.274	573282.242	29.712	378437.359	24.165	939513.405	25.168	502784.361	241.554
	$m_Y$	547928.028	1152129.924	5.736	1269998.173	5.307	497372.024	5.881	404705.516	79.708	363825.969	50.175	598629.738	20.127	380398.629	303.424
	$m_Z$	492436.992	2622689.290	6.613	1818760.336	6.176	1912697.458	6.220	542825.278	39.172	397867.069	46.751	967996.618	17.352	715962.609	227.476
18. (V <sub>S</sub> A) <sub>0</sub>	$m_X$	0.324	13.270	5.972	31.407	4.827	81.115	5.200	529.367	7.189	2329.453	25.978	253.662	5.176	8761.155	32.633
	$m_Y$	0.327	5.025	5.743	19.449	5.311	27.017	5.936	109.334	6.809	1439.783	31.855	278.665	5.845	11109.504	53.114
	$m_Z$	0.532	11.531	6.604	34.412	6.166	96.601	6.211	505.031	6.319	2568.341	6.660	365.584	9.971	11187.116	7.550
19. (P <sub>S</sub> V <sub>S</sub> A) <sub>0</sub>	$m_X$	6.472	40264.446	5.969	55840.525	4.809	51106.442	5.194	150584.540	7.934	352592.286	7.633	116492.271	5.182	410555.029	13.172
	$m_Y$	2.387	21629.191	5.759	23043.296	5.320	18432.817	5.942	107670.593	6.939	268285.143	14.417	30460.778	5.753	330881.852	38.387
	$m_Z$	6.596	38231.576	6.569	52804.785	6.128	47947.779	6.176	143467.394	6.757	350676.991	24.954	109597.512	9.907	415125.033	11.705

**Appendix A.5.2.** Results based on second type pre-adjustment for homogenously distributed points

Point	set	H-0		H-10				H-20				H-30				H-40			
	type	GCP		GCP		ICP		GCP		ICP		GCP		ICP		GCP		ICP	
	#	47		37				27				17				7			
EOP	Process	$\overline{LP}$	$B$	$\overline{LP}$	$B$	$\overline{LP}$	$B$	$\overline{LP}$	$B$	$\overline{LP}$	$B$	$\overline{LP}$	$B$	$\overline{LP}$	$B$	$\overline{LP}$	$B$	$\overline{LP}$	$B$
1. P <sub>S</sub>	$m_X$	0.605	0.605	0.607	0.604	6.037	5.973	0.624	0.600	4.754	4.835	0.598	0.524	4.985	5.282	0.573	0.423	6.803	7.292
	$m_Y$	0.212	0.212	0.217	0.218	5.800	5.747	0.218	0.263	5.374	5.326	0.224	0.341	6.042	5.983	0.234	0.693	7.013	6.840
	$m_Z$	0.953	0.953	0.982	0.987	6.456	6.626	0.977	0.975	5.929	6.208	0.978	0.958	5.908	6.307	1.058	0.925	6.082	6.414
2. P <sub>S0</sub>	$m_X$	0.605	0.605	0.606	0.603	6.037	5.971	0.624	0.597	4.753	4.843	0.598	0.542	4.984	5.281	0.573	0.477	6.802	7.127
	$m_Y$	0.212	0.212	0.217	0.205	5.800	5.743	0.218	0.190	5.374	5.324	0.224	0.200	6.042	5.982	0.235	0.695	7.013	6.673
	$m_Z$	0.952	0.952	0.981	0.981	6.454	6.614	0.976	0.958	5.927	6.185	0.978	0.938	5.907	6.257	1.056	0.463	6.082	6.428
3. P <sub>S1</sub>	$m_X$	0.617	0.617	0.618	0.612	6.036	5.966	0.634	0.627	4.755	4.825	0.606	0.607	4.988	5.206	0.583	1.223	6.809	7.304
	$m_Y$	0.209	0.209	0.214	0.221	5.801	5.753	0.215	0.223	5.374	5.314	0.221	0.231	6.043	5.941	0.231	0.922	7.015	6.704
	$m_Z$	0.966	0.966	0.994	0.986	6.462	6.614	0.989	0.976	5.938	6.185	0.990	0.969	5.917	6.238	1.070	1.952	6.088	6.054
4. P <sub>S2</sub>	$m_X$	0.610	0.610	0.612	0.610	6.036	5.967	0.629	0.624	4.752	4.832	0.603	0.602	4.986	5.230	0.579	0.591	6.806	7.157
	$m_Y$	0.211	0.211	0.216	0.219	5.800	5.746	0.218	0.216	5.374	5.311	0.223	0.230	6.043	5.945	0.235	0.627	7.014	6.787
	$m_Z$	0.958	0.958	0.986	0.979	6.459	6.610	0.980	0.963	5.932	6.178	0.981	0.949	5.913	6.226	1.059	0.705	6.087	6.392
5. V <sub>S</sub>	$m_X$	0.751	0.751	0.748	962043.081	6.002	5.966	0.773	2478851.193	4.736	4.818	0.743	2581511.487	4.994	5.175	2536096.516	808634.245	2072611.140	15.744
	$m_Y$	0.177	0.177	0.183	924231.288	5.827	5.743	0.185	1359971.849	5.385	5.307	0.191	1473031.690	6.057	5.989	627658.877	497754.652	450254.949	6.961
	$m_Z$	1.110	1.110	1.135	1038974.333	6.487	6.605	1.138	2455864.367	5.997	6.189	1.136	2570855.510	5.996	6.300	2451801.227	823513.996	1987952.832	17.808
6. V <sub>0</sub>	$m_X$	0.649	0.649	0.648	0.375	6.028	5.968	0.665	1.823	4.749	4.818	0.636	6.236	4.989	5.168	0.603	14.154	6.815	7.222
	$m_Y$	0.201	0.201	0.206	0.411	5.807	5.741	0.208	0.614	5.377	5.337	0.214	3.007	6.046	5.999	0.226	3.595	7.018	6.857
	$m_Z$	1.000	1.000	1.027	0.655	6.468	6.609	1.022	2.341	5.950	6.179	1.022	6.982	5.934	6.248	1.094	15.794	6.102	6.492
7. V <sub>1</sub>	$m_X$	0.618	0.618	0.619	0.618	6.033	5.968	0.638	0.629	4.750	4.825	0.612	0.592	4.984	5.204	0.583	0.620	6.805	7.166
	$m_Y$	0.208	0.208	0.214	0.216	5.803	5.745	0.215	0.225	5.375	5.310	0.221	0.247	6.044	5.937	0.232	0.213	7.015	6.826
	$m_Z$	0.967	0.967	0.995	0.999	6.457	6.609	0.991	1.011	5.932	6.182	0.993	1.056	5.914	6.236	1.068	1.424	6.089	6.375
8. V <sub>2</sub>	$m_X$	0.624	0.624	0.624	0.625	6.032	5.967	0.642	0.642	4.751	4.825	0.615	0.606	4.985	5.205	0.586	0.581	6.806	7.186
	$m_Y$	0.207	0.207	0.212	0.219	5.804	5.747	0.213	0.225	5.376	5.312	0.219	0.237	6.044	5.938	0.230	0.114	7.015	6.811
	$m_Z$	0.973	0.973	1.001	0.998	6.458	6.611	0.997	0.999	5.936	6.180	1.000	1.037	5.917	6.230	1.074	1.421	6.090	6.383
9. A	$m_X$	0.608	0.608	0.609	0.608	6.037	5.967	0.626	0.629	4.754	4.825	0.598	0.594	4.985	5.200	0.586	0.571	6.806	7.186
	$m_Y$	0.211	0.211	0.217	0.212	5.800	5.747	0.218	0.205	5.374	5.310	0.224	0.200	6.042	5.936	0.230	0.163	7.015	6.811
	$m_Z$	0.956	0.956	0.984	0.983	6.458	6.610	0.979	0.990	5.931	6.180	0.979	1.004	5.909	6.228	1.074	1.146	6.090	6.383
10. A <sub>0</sub>	$m_X$	0.608	0.608	0.609	0.607	6.036	5.967	0.627	0.624	4.752	4.824	0.599	0.597	4.984	5.200	0.575	0.614	6.802	7.188
	$m_Y$	0.211	0.211	0.216	0.215	5.801	5.747	0.218	0.212	5.374	5.310	0.224	0.209	6.042	5.936	0.235	0.120	7.013	6.826
	$m_Z$	0.956	0.956	0.984	0.982	6.455	6.611	0.979	0.977	5.929	6.178	0.979	0.980	5.907	6.226	1.057	1.103	6.083	6.331
11. A <sub>1</sub>	$m_X$	0.617	0.617	0.618	0.620	6.035	5.967	0.635	0.638	4.753	4.825	0.607	0.611	4.987	5.205	0.583	0.665	6.807	7.163
	$m_Y$	0.209	0.209	0.214	0.217	5.802	5.746	0.215	0.217	5.375	5.311	0.221	0.223	6.043	5.937	0.232	0.231	7.015	6.811
	$m_Z$	0.966	0.966	0.994	0.994	6.460	6.610	0.990	0.992	5.936	6.180	0.991	1.006	5.916	6.231	1.069	1.289	6.088	6.340
12. A <sub>2</sub>	$m_X$	0.612	0.612	0.614	0.617	6.036	5.967	0.631	0.635	4.752	4.826	0.604	0.604	4.986	5.206	0.580	0.665	6.806	7.209
	$m_Y$	0.210	0.210	0.216	0.216	5.801	5.747	0.217	0.219	5.374	5.311	0.223	0.227	6.043	5.937	0.234	0.231	7.014	6.818
	$m_Z$	0.960	0.960	0.988	0.984	6.459	6.611	0.983	0.976	5.932	6.177	0.983	0.982	5.914	6.223	1.062	1.289	6.087	6.337
13. P <sub>S</sub> V <sub>S</sub>	$m_X$	143.192	143.192	93.266	1436350.889	96.580	5.969	155.675	1378011.919	128.290	4.776	54.470	2058748.908	41.139	5.099	4.941	3829303.264	8.163	362.688
	$m_Y$	39.369	39.369	25.559	1773095.665	31.412	5.805	42.479	1686469.231	37.916	5.325	15.636	1412877.835	14.507	5.916	1.138	2059551.366	7.425	103.105
	$m_Z$	138.181	138.181	90.182	1628973.813	94.151	6.621	150.283	1560829.158	126.031	6.148	52.953	2075642.521	42.380	6.073	5.241	3966074.841	8.812	359.442
14. (P <sub>S</sub> V) <sub>0</sub>	$m_X$	0.329	0.329	0.347	42.819	6.157	5.966	0.353	64.469	4.817	4.824	0.373	792.812	4.958	5.212	0.414	7898.025	6.675	7.260
	$m_Y$	0.329	0.329	0.334	45.705	5.735	5.757	0.327	44.889	5.348	5.319	0.328	253.666	6.006	5.945	0.331	5428.240	6.968	6.885
	$m_Z$	0.461	0.461	0.489	47.513	6.322	6.599	0.505	68.942	5.698	6.169	0.538	776.487	5.635	6.228	0.621	8214.423	5.874	6.378
15. P <sub>S</sub> A	$m_X$	6.623	6.623	6.448	94.819	10.373	5.971	7.309	86.578	9.284	4.814	8.570	952.609	9.654	5.009	7.518	482936.244	10.240	388.881
	$m_Y$	2.314	2.314	2.274	82.034	4.971	5.747	2.539	423.603	5.280	5.298	2.964	648.680	5.700	5.942	1.941	344851.187	7.007	177.722
	$m_Z$	6.204	6.204	6.000	65.717	9.000	6.599	6.849	178.147	7.446	6.140	8.011	599.221	7.027	5.973	8.025	444653.596	7.880	424.213
16. (P <sub>S</sub> A) <sub>0</sub>	$m_X$	1.897	1.897	1.695	16.855	6.752	5.965	1.780	42.779	5.389	4.811	1.664	84.852	5.166	5.175	1.011	157.089	6.482	7.169
	$m_Y$	0.891	0.891	0.838	37.434	5.513	5.743	0.853	169.686	5.260	5.319	0.818	304.033	5.861	5.982	0.647	457.713	6.837	6.886
	$m_Z$	1.990	1.990	1.825	14.639	6.223	6.605	1.762	63.691	5.161	6.159	1.540	124.346	4.800	6.197	1.464	326.481	5.388	6.345
17. V <sub>S</sub> A	$m_X$	18.679	18.679	14.421	936297.357	17.640	5.960	21.151	1638923.530	20.674	4.811	18.482	627999.282	19.393	5.184	94.315	606870.208	88.631	274.730
	$m_Y$	5.122	5.122	4.439	1021817.177	5.278	5.746	5.580	376023.351	6.271	5.307	5.313	449218.938	6.477	5.791	19.858	235035.787	17.260	207.358
	$m_Z$	1.704	1.704	9.943	984037.447	13.746	6.609	4.853	1551614.818	5.718	6.168	8.979	720597.936	9.936	6.080	78.560	613477.167	72.893	288.327
18. (V <sub>S</sub> A) <sub>0</sub>	$m_X$	0.326																	



Appendix A.5.3. Results based on second type pre-adjustment for grouped points

Point	set	G-A				G-B				G-C			
	type	GCP		ICP		GCP		ICP		GCP		ICP	
	#	23		24		24		23		17		30	
EOP	Process	$\overline{LP}$	$B$	$\overline{LP}$	$B$	$\overline{LP}$	$B$	$\overline{LP}$	$B$	$\overline{LP}$	$B$	$\overline{LP}$	$B$
1. P <sub>S</sub>	$m_x$	0.678	11.456	24.725	20.309	0.510	0.692	5.622	15.166	39.595	29.139	39.595	109.269
	$m_y$	0.193	8.954	33.253	16.244	0.199	0.827	5.985	15.690	24.061	54.563	24.061	88.595
	$m_z$	0.926	12.701	7.083	14.086	1.019	1.022	9.560	9.264	42.480	6.811	42.480	96.555
2. P <sub>S0</sub>	$m_x$	0.678	5.687	24.726	12.257	0.511	0.619	5.614	4.989	8.964	29.142	8.962	10.890
	$m_y$	0.193	9.427	33.253	19.385	0.199	0.346	5.984	5.725	15.137	54.563	15.136	33.003
	$m_z$	0.926	7.263	7.083	21.784	1.019	1.045	9.568	10.720	11.266	6.811	11.264	21.410
3. P <sub>S1</sub>	$m_x$	0.682	4.658	24.729	18.632	0.512	0.881	5.598	4.939	6.620	29.148	6.621	21.080
	$m_y$	0.192	10.236	33.256	19.625	0.198	0.642	5.980	5.620	12.589	54.566	12.590	40.079
	$m_z$	0.930	6.100	7.080	28.831	1.025	1.303	9.592	10.931	7.577	6.812	7.578	22.465
4. P <sub>S2</sub>	$m_x$	0.680	5.639	24.727	21.667	0.515	0.650	5.613	4.989	5.810	29.145	5.808	20.895
	$m_y$	0.193	11.726	33.254	21.278	0.197	0.545	5.984	5.578	10.105	54.564	10.105	43.187
	$m_z$	0.928	7.379	7.083	36.431	1.028	1.073	9.575	11.049	6.977	6.812	6.976	16.463
5. V <sub>S</sub>	$m_x$	0.717	2766973.512	24.768	23.783	0.725	2.248	5.536	5.027	1368058.738	29.181	1223649.079	72.216
	$m_y$	0.180	2346779.341	33.271	32.141	0.142	0.340	5.966	5.475	275362.699	54.580	941124.562	52.107
	$m_z$	0.969	2873251.756	7.054	9.662	1.235	0.903	9.703	13.305	1302242.979	6.820	1284129.062	85.197
6. V <sub>0</sub>	$m_x$	0.683	1490.498	24.729	26.250	0.621	70.480	5.563	5.210	7169.615	29.153	7173.940	42.332
	$m_y$	0.192	526.680	33.254	32.866	0.168	48.309	5.972	5.743	1597.907	54.568	1597.374	55.964
	$m_z$	0.931	1462.314	7.081	7.483	1.133	73.466	9.645	9.625	6890.962	6.814	6894.834	11.119
7. V <sub>1</sub>	$m_x$	0.683	0.829	24.731	26.037	0.544	0.533	5.612	5.293	1.229	29.145	1.230	34.051
	$m_y$	0.191	0.392	33.256	32.905	0.191	0.162	5.983	5.931	0.369	54.564	0.371	54.111
	$m_z$	0.932	0.837	7.079	7.137	1.050	1.068	9.574	10.057	2.796	6.812	2.793	10.956
8. V <sub>2</sub>	$m_x$	0.680	0.717	24.727	23.038	0.542	0.525	5.598	5.467	1.764	29.147	1.762	33.104
	$m_y$	0.193	0.228	33.254	32.450	0.192	0.215	5.980	5.928	0.315	54.566	0.315	54.091
	$m_z$	0.928	0.871	7.082	5.144	1.048	1.061	9.589	10.389	1.408	6.812	1.408	9.199
9. A	$m_x$	0.680	0.646	24.727	23.038	0.512	0.595	5.615	5.251	2.011	29.141	2.011	26.986
	$m_y$	0.193	0.398	33.254	32.450	0.198	0.217	5.983	5.675	0.508	54.564	0.509	48.643
	$m_z$	0.928	0.977	7.082	5.144	1.022	1.089	9.569	7.024	2.724	6.812	2.723	63.276
10. A <sub>0</sub>	$m_x$	0.680	0.453	24.727	25.647	0.513	0.488	5.613	5.265	0.442	29.144	0.441	30.191
	$m_y$	0.193	0.430	33.254	32.794	0.198	0.264	5.983	5.879	0.557	54.564	0.558	54.001
	$m_z$	0.928	0.626	7.082	6.897	1.022	0.986	9.570	10.056	0.481	6.812	0.478	6.762
11. A <sub>1</sub>	$m_x$	0.682	1.078	24.730	24.408	0.512	0.510	5.598	5.200	1.387	29.147	1.384	29.269
	$m_y$	0.192	0.307	33.255	32.524	0.198	0.159	5.980	5.870	0.338	54.566	0.337	53.716
	$m_z$	0.930	1.335	7.080	5.731	1.025	1.092	9.592	9.875	1.254	6.812	1.252	7.387
12. A <sub>2</sub>	$m_x$	0.681	0.613	24.728	24.754	0.514	0.523	5.613	5.201	0.847	29.145	0.846	29.782
	$m_y$	0.192	0.411	33.254	32.570	0.197	0.232	5.984	5.868	0.542	54.564	0.543	53.781
	$m_z$	0.929	1.113	7.082	6.002	1.027	0.989	9.575	9.869	0.853	6.812	0.849	6.974
13. P <sub>S</sub> V <sub>S</sub>	$m_x$	418577.182	439729.367	398066.101	73468.889	166.470	1582595.347	83.994	21.945	2383609.474	148.373	94018.431	148.373
	$m_y$	257598.585	403629.438	300119.123	101890.137	45.421	1914580.592	18.204	13.523	2163489.615	82.595	53648.759	82.595
	$m_z$	311548.658	621453.846	296393.044	90005.618	160.697	1765500.256	87.175	35.851	2525017.860	204.753	95661.648	204.753
14. (P <sub>S</sub> V <sub>S</sub> ) <sub>0</sub>	$m_x$	0.714	20146.873	24.765	24.888	766360.502	636970.239	771083.509	697.141	197465.402	0.781	156780.579	27.647
	$m_y$	0.189	8586.594	33.262	32.432	269235.778	371120.093	253744.220	152.490	99609.424	0.209	90957.713	52.250
	$m_z$	0.964	19960.392	7.056	7.430	633107.335	584356.114	639129.754	707.654	199323.756	0.960	160271.802	6.988
15. P <sub>S</sub> A	$m_x$	2.471	6966.894	26.347	16.219	9.118	1447.215	10.803	49.936	24898.881	22.344	24930.954	77.391
	$m_y$	1.221	10035.695	34.252	12.924	2.947	780.653	5.474	29.277	18406.978	50.841	18424.392	52.365
	$m_z$	2.550	6705.287	6.174	19.940	8.196	897.925	12.613	60.908	7757.400	8.552	7794.052	108.753
16. (P <sub>S</sub> A) <sub>0</sub>	$m_x$	0.403	1253.452	24.412	27.891	3.298	93.044	8.024	5.194	1882.829	28.718	1882.853	28.296
	$m_y$	0.320	250.472	33.112	31.359	1.309	551.117	6.443	5.836	673.258	54.383	673.271	52.801
	$m_z$	0.587	343.222	7.289	6.592	3.416	244.505	6.793	10.212	1359.767	6.761	1359.740	7.004
17. V <sub>S</sub> A	$m_x$	5.042	380800.668	24.990	18.639	88.572	86170.641	40.385	100.406	275365.674	24.553	502784.361	127.657
	$m_y$	3.503	351781.019	32.712	20.229	17.423	114045.306	8.211	52.964	273554.193	53.427	380398.629	142.244
	$m_z$	6.633	500046.019	20.348	9.214	123.529	179167.514	340.239	122.982	503858.960	24.138	715962.609	147.236
18. (V <sub>S</sub> A) <sub>0</sub>	$m_x$	0.664	1959.034	24.714	25.990	1.098	45.006	5.363	5.178	6529.395	29.014	8761.155	32.800
	$m_y$	0.175	1344.455	33.274	31.858	0.080	202.876	5.911	5.843	10620.299	54.518	11109.504	53.151
	$m_z$	0.890	2217.847	7.102	6.652	1.433	82.213	9.892	9.960	9134.392	6.788	11187.116	7.627
19. (P <sub>S</sub> V <sub>S</sub> A) <sub>0</sub>	$m_x$	0.777	416664.708	23.738	14.204	486088.961	484249.794	500616.408	6.322	454477.910	27.260	410555.029	21.305
	$m_y$	1.169	260970.641	32.427	20.057	134814.403	132974.748	123105.777	6.076	285279.246	53.168	330881.852	45.134
	$m_z$	0.419	408516.337	7.825	15.700	426718.814	429948.733	442289.121	10.934	445664.058	6.917	415125.033	6.428



## CURRICULUM VITAE



**Candidate's full name:** Hüseyin TOPAN

**Place and date of birth:** Milas, 27 August 1980

**Permanent Address:** Zonguldak Karaelmas Üniversitesi Mühendislik  
Fakültesi Jeodezi ve Fotogrametri Mühendisliği  
Bölümü 67100 Zonguldak Türkiye

**Universities and  
Colleges attended:** Zonguldak Karaelmas University (Bsc.)  
Zonguldak Karaelmas University (Msc.)

### Publications:

- **Topan, H.**, Büyüksalih, G., Jacobsen, K., 2004, Comparison of Information Contents of High Resolution Space Images, *International Archives of Photogrammetry and Remote Sensing*, Vol. 35, Part B4, pp. 583-588, July 12-23, 2004 Istanbul, Turkey.
- Şahin, H., **Topan, H.**, Karakış, S., Marangoz, A. M., 2004, Comparison of Object Oriented Image Analysis and Manual Digitizing for Feature Extraction, *International Archives of Photogrammetry and Remote Sensing*, Vol. 35, Part B8, pp. 114-118, July 12-23, 2004 Istanbul, Turkey.
- Büyüksalih, G., Oruç, M., **Topan, H.**, Jacobsen, K., 2004, Geometric Accuracy Evaluation, DEM Generation and Validation for SPOT-5 Level 1B Stereo Scene, *EARSeL Workshop, Remote Sensing for Developing Countries*, September 26-29, 2004 Cairo (Egypt).
- Şahin, H., Büyüksalih, G., Akçın, H., **Topan, H.**, Karakış, S., Marangoz, A. M., 2004, Information Content Analysis of KVR-1000 Ortho-Image Based on the Available, Topographic Maps in the GIS Environment, *EARSeL Workshop on Remote Sensing for Developing Countries*, September 26-29, 2004 Cairo (Egypt).
- **Topan, H.**, Büyüksalih, G., Koçak, M. G., 2005, IRS-1C Düzey 1B Görüntüsünün Geometrik Analizinin Sensör Yöneltilme Modelleriyle ve Değişik Referans Verileriyle İrdelenmesi, *10. Türkiye Harita Bilimsel ve Teknik Kurultayı*, March 25 - April 1, 2005 Ankara, Turkey.
- Şahin, H., Karakış, S., **Topan, H.**, Marangoz, A. M., 2005, KVR-1000 Uydu Görüntüsü Üzerinden Elle Sayısallaştırma ve Nesneye Yönelik Görüntü Analizi

Yöntemlerinin Karşılaştırılması, *10. Türkiye Harita Bilimsel ve Teknik Kurultayı*, Ankara, March 25 - April 1, 2005 Ankara, Turkey.

- Jacobsen, K., Büyüksalih, G., **Topan, H.**, 2005, Geometric Models for the Orientation of High Resolution Optical Satellite Sensors, *ISPRS Hannover Workshop 2005: High-Resolution Earth Imaging for Geospatial Information*, May 17-20, 2005 Hannover, Germany.
- **Topan, H.**, Büyüksalih, G., Jacobsen, K., 2005, Information Contents of High Resolution Satellite Images, *EARSeL Workshop on 3D Remote Sensing*, June 9-11, 2005 Porto Portugal.
- Karakış, S., **Topan, H.**, Büyüksalih, G., Marangoz, A. M., Jacobsen, K., 2005, Semantic Analysis of Space Imagery for Mapping Purposes, *Proceedings of 2nd International Conference on Recent Advances in Space Technologies*, pp. 500-504, June 9-11 2005 Istanbul, Turkey.
- Özfidan, F., **Topan, H.**, Şahin, H., Karakış, S., 2005, Yüksek Çözünürlüklü Uydu Görüntülerinin Bilgi İçeriklerinin Karşılaştırılması, *IGSM&GHG 2005*, June 13-18, 2005 Istanbul, Turkey.
- Büyüksalih, G., Koçak, M. G., **Topan, H.**, Oruç, M., Marangoz, A. M., 2005, SPOT Revisited: Accuracy Assessment, DEM Generation and Validation From Stereo SPOT 5 HRG Images, *The Photogrammetric Record*, 20(110): 130-146 (June 2005).
- **Topan, H.**, Büyüksalih, G., Jacobsen, K., 2006, Information Contents of OrbView-3 for Topographic Mapping, *ISPRS Ankara Workshop 2006 Topographic Mapping from Space (with Special Emphasis on Small Satellite)*, February 14-16, 2006 Ankara, Turkey.
- Marangoz, A. M., Karakış, S., Oruç, M., Şahin, H., Sefercik, U. G., **Topan, H.**, Büyüksalih, G., 2006, 3D Cultural Heritage Documentation of Safranbolu Test Site Using High Resolution Satellite Imagery, *1st Workshop of the EARSeL Special Interest Group Urban Remote Sensing "Urban Remote Sensing Challenges & Solutions"*, March 2-3, 2006, Berlin Adlershof, Germany.
- Büyüksalih, G., **Topan, H.**, 2006, Uzaydan Harita Yapımı, *II. Ulusal Mühendislik Kongresi*, May 11-13, 2006 Zonguldak, Turkey.
- **Topan, H.**, Maktav, D., Jacobsen, K., Büyüksalih, G., 2006, Mapping Potential of High Resolution Space Images in Mountainous Urban Areas, *ISPRS International Archives of Photogrammetry and Remote Sensing*, Vol. 35, Part 8, Remote Sensing Applications for a Sustainable Future, September 1-3, 2006 Haifa, Israel.
- **Topan, H.**, Maktav, D., Büyüksalih, G., 2006, Uydu Görüntülerinin Bilgi İçeriğinin Topografik Harita Yapımı Açısından İncelenmesi, *I. Uzaktan Algılama - CBS Çalıştay ve Paneli*, November 27-29, 2006 Istanbul, Turkey.
- **Topan, H.**, Büyüksalih, G., Jacobsen, K., 2006, Information Content of High-resolution Satellite Image: Mapping with OrbView-3 Images, *GIM International*, Volume 20, Issue 12, December 2006.
- **Topan, H.**, Oruç, M., Koçak, M. G., 2007, Ortogörüntü Üretiminde Yer Kontrol Noktası Seçimi ve Sonuçlara Etkisi, *11. Türkiye Harita Bilimsel ve Teknik Kurultayı*, April 2-6, 2007 Ankara, Turkey.

- Karakış, S., Marangoz, A. M., **Topan, H.**, Şahin, H., 2007, Pan-sharp QuickBird Görüntüsü Kullanılarak Nesne-Tabanlı Görüntü Analizi ve Ekran Üzerinden Elle Sayısallaştırma Yöntemlerinin Karşılaştırılması, *11. Türkiye Harita Bilimsel ve Teknik Kurultayı*, April 2-6, 2007 Ankara, Turkey.
- **Topan, H.**, Büyüksalih, G., Derya Maktav, 2007, Mapping Potential of Orbview-3 Panchromatic Image in Mountainous Urban Areas: Results of Zonguldak Test-Field, *Urban Remote Sensing Joint Event 2007 (4th IEEE GRSS/ISPRS Joint Workshop on Remote Sensing and Data Fusion over Urban Areas & 6th International Symposium of Remote Sensing of Urban Areas)*, April 11-13, 2007 Paris, France.
- Ateşoğlu, A., Tunay, M., **Topan, H.**, Oruç, M., 2007, Uydu Görüntüleri Bilgi İçeriğinin Ormancılık Çalışmaları Açısından Değerlendirilmesi, *Orman Kaynaklarının İşlevleri Kapsamında Darboğazları, Çözüm Önerileri ve Öncelikler*, October, 17-19 2007, Istanbul, Turkey.
- **Topan, H.**, Kutoğlu, Ş. H., 2009, Georeferencing Accuracy Assessment of High Resolution Satellite Images Using Figure Condition Method, *IEEE Transactions on Geoscience and Remote Sensing*, Volume 47, Issue 4: 1256-1261, DOI: 10.1109/TGRS.2008.2008098.
- **Topan, H.**, Maktav, D., Jacobsen, K., Büyüksalih, G., 2009, Information Contents of Optical Satellite Images for Topographic Mapping, *International Journal of Remote Sensing*, Vol. 30, No: 7, April 10, 2009: 1819-1827, DOI:10.1080/01431160802642271.
- **Topan, H.**, Çelik, R. N., 2009, Young Surveyors' Days, *GIM International*, Vol. 23, Issue 5, May 2009: 32-33.
- **Topan, H.**, Oruç, M., Jacobsen, K., 2009, Potential of Manual and Automatic Feature Extraction From High Resolution Space Images in Mountainous Urban Areas, *ISPRS Hannover Workshop 2009 High-Resolution Earth Imaging for Geospatial Information*, June 2-5, 2009 Hannover, Germany. 6 pages.